

12-1-2016

Ionic Electroactive Polymer Devices: Physics-Based Modeling with Experimental Investigation and Verification

Tyler Paul Stalbaum

University of Nevada, Las Vegas, stalbau2@unlv.nevada.edu

Follow this and additional works at: <https://digitalscholarship.unlv.edu/thesesdissertations>



Part of the [Mechanical Engineering Commons](#)

Repository Citation

Stalbaum, Tyler Paul, "Ionic Electroactive Polymer Devices: Physics-Based Modeling with Experimental Investigation and Verification" (2016). *UNLV Theses, Dissertations, Professional Papers, and Capstones*. 2904.

<https://digitalscholarship.unlv.edu/thesesdissertations/2904>

This Dissertation is protected by copyright and/or related rights. It has been brought to you by Digital Scholarship@UNLV with permission from the rights-holder(s). You are free to use this Dissertation in any way that is permitted by the copyright and related rights legislation that applies to your use. For other uses you need to obtain permission from the rights-holder(s) directly, unless additional rights are indicated by a Creative Commons license in the record and/or on the work itself.

This Dissertation has been accepted for inclusion in UNLV Theses, Dissertations, Professional Papers, and Capstones by an authorized administrator of Digital Scholarship@UNLV. For more information, please contact digitalscholarship@unlv.edu.

IONIC ELECTROACTIVE POLYMER DEVICES: PHYSICS-BASED MODELING WITH EXPERIMENTAL
INVESTIGATION AND VERIFICATION

By

Tyler Paul Stalbaum

Bachelor of Science – Mechanical Engineering
University of Nevada, Las Vegas
2010

Master of Science – Industrial Engineering
Purdue University
2013

A dissertation in partial fulfillment
of the requirements for the

Doctor of Philosophy – Mechanical Engineering

Department of Mechanical Engineering
Howard R. Hughes College of Engineering
The Graduate College

University of Nevada, Las Vegas
December 2016



Dissertation Approval

The Graduate College
The University of Nevada, Las Vegas

September 16, 2016

This dissertation prepared by

Tyler Stalbaum

entitled

Ionic Electroactive Polymer Devices: Physics-Based Modeling with Experimental Investigation and Verification

is approved in partial fulfillment of the requirements for the degree of

Doctor of Philosophy – Mechanical Engineering
Department of Mechanical Engineering

Kwang Kim, Ph.D.
Examination Committee Chair

Kathryn Hausbeck Korgan, Ph.D.
Graduate College Interim Dean

Hui Zhao, Ph.D.
Examination Committee Member

Pushkin Kachroo, Ph.D.
Examination Committee Member

Woosoon Yim, Ph.D.
Examination Committee Member

Dong-Chan Lee, Ph.D.
Graduate College Faculty Representative

ABSTRACT

Stalbaum, Tyler P., Ph.D. M.E., University of Nevada, Las Vegas, August 2016.
Ionic Electroactive Polymer Devices: Physics-Based Modeling with Experimental Investigation and Verification.
Major Professor: Kwang J. Kim.

The primary focus of this study is to examine, understand, and model ionic electroactive polymer based systems in attempt to further develop this field of study. Physics-based modeling is utilized, as opposed to empirical modeling, to achieve a deeper insight to the underlying physics. The ionic electroactive polymer system of primary interest in this study is ionic polymer-metal composite (IPMC) devices. Other similar devices, such as anion-exchange membrane (AEM) type actuators and flow battery systems are also investigated using the developed model. The underlying physics are in the studies of transport phenomenon for describing the ionic flow within the polymer membrane, solid mechanics for describing deformation of the given devices, electric potential and electric currents physics for the voltage across the devices, and ion exchange along with chemical reaction in case of flow batteries. Specific details of these systems are analyzed, such as geometrical and electrode effects. The results in modeling IPMC actuators and sensors have been used to experimentally validate the modeling framework and have provided keen insight to the underlying physics behind these transduction phenomena. The developed models will benefit researchers in these fields and are expected to provide a better understanding of these systems. This study provides a framework for design and fabrication of advanced, highly integrated, ionic migration and exchange polymer-composite devices.

In particular, this work focuses on finite element simulations of ionic electroactive polymers using COMSOL Multiphysics versions 4.3 through 5.2, with primary focus on ionic polymer-metal composite devices. The basic framework model for IPMCs is of greatest importance and is the initial focus of this work. This is covered in Chapter 3 in detail with experimental comparison of results. Other

aspects of interest are geometrical and electrode effects of IPMCs, which are discussed in Chapter 3 and Chapter 4. Applications of the modeling framework, such as in modeling other electroactive polymer actuators is covered in Chapter 5 and Chapter 6, which includes simulations of electrodeless artificial cilia actuators in lithium chloride (LiCl) electrolyte, discussion and modeling of all-Vanadium oxidation reduction (redox) flow battery devices, fluid-structure interactions with IPMCs, and discussion of implementing the modeling framework for anion type IPMCs. Two publications from Journal of Applied Physics and one paper accepted for publication from the Marine Technology Society Journal are included herein, with publisher permission. These papers focus directly on topics of interest to this work. They underwent several revisions and are included in full or large excerpt form to provide the most accurate description and discussion of these topics. The author of this dissertation is first author and did much of the work of one of the three papers; specific author contributions for the other two papers are detailed before each paper is presented, in which the author of this dissertation was primarily responsible for finite element simulations, discussion, and revisions. Chapter 7 and Chapter 8 contain conclusions and recommendations for future work, respectively.

ACKNOWLEDGEMENTS

I would like to especially thank my academic advisor Professor Kwang J. Kim for his support, ingenuity in research, advice, discussion and many teachings. I would also like to extend this gratitude to my research committee members, Drs. Woosoon Yim, Hui Zhao, Pushkin Kachroo, and Dong-Chan Lee. I also would like to thank the other research members of our lab, Viljar Palmre, Qi Shen, Taeseon Hwang, Sarah Trabia, Shelby Nelson, Jun Woo Park, Jameson Lee, Choonghan Lee, Kevin Yim, Zakai Olsen, Robert Hunt, Anupam Kumar, and MD Bhuiya; without their help and individual expertise, this work would not have been possible. I would also like to thank Dr. David Pugal for pioneering development of the IPMC physics modeling framework and first demonstrating the working model in COMSOL. I'd like to especially thank Dr. Viljar Palmre for helping with IPMC fabrication, experiments, and understanding of ionic polymer-metal composites underlying physics; additionally, his calm and motivational demeanor made for an exceptionally pleasant research atmosphere. I would also like to thank Joan Conway of the UNLV Department of Mechanical Engineering for always being helpful, punctual, and for her care and dedication to students.

Additionally, I am very grateful for the teachings and mentoring of many professors throughout my studies at UNLV. Namely, I would like to thank Drs. Angel Muleshkov, Vellore C. Venkatesh, Yitung Chen, Mohammad Trabia, Sean Hsieh, and Marianne Austin for their outstanding lectures, elaborate discussions, and strong dedication to the development and education of their students. I am also grateful for my high school counselor, Alison Foster, and principal, Anita Wilbur, for all of their help and guidance in beginning my academic career. Last but not least, I would like to thank my family and friends for their unconditional support and compassion. Additional thanks to partial financial support from the Office of Naval Research (N00014-13-1-0274) and the National Aeronautics and Space Administration under Grant No. NNX13AN15A.

DEDICATION

To my mother,
Diane K. Stalbaum,
and in loving memory of my father,
Gregory L. Stalbaum
July 05, 1958 - July 19, 2014.

TABLE OF CONTENTS

Abstract	iii
Acknowledgements	v
Dedication	vi
List of Tables	ix
List of Figures	x
Chapter 1: Introduction	1
Problem Statement	3
Chapter 2: Background	5
Chapter 3: Sensing and Actuation Framework for Ionic Polymer-Metal Composites	11
Ionic Polymer-Metal Composite Governing Physics	12
Modeling Approach	16
Experimental Procedure	19
Results	20
Back Relaxation	21
Frequency Response	25
Frequency Response of an IPMC to Shear Loading	27
Finite Element Simulations of Tube-Shaped Ionic Polymer-Metal Composite Sensors	29
Model Implementation	30
Sample Preparation and Experimental Setup	32
Experimental and Simulation Results	35
Chapter 4: Electrode Effects of IPMCs	42
Physics-Based Modeling Encompassing Variable Electrode Surface Resistance	42

Modeling and Discussion	47
Chapter 5: Electrodeless EAP Actuators	56
Promising Developments in Marine Applications with Artificial Muscles: Electrodeless Artificial-Cilia Microfibers	56
Artificial Muscle Fibers	59
Fabrication of Cilium-Inspired, Electroactive Fibers	62
Experimental Methods	64
Results and Physics-Based Modeling	65
Development of a Prototype Biomimetic Cilia Array	71
Chapter 6: Example Applications of the Model Framework	76
IPMC Interaction with Fluid Flow	76
Flow Battery Systems	78
Anion Membrane IPMCs	82
Chapter 7: Conclusions	87
Chapter 8: Recommendations for Future Work	88
Appendix A: Nomenclature	89
Appendix B: Derivation of Principal Strain for Bending and Shear Cases	91
Appendix C: Copyright Permission Approvals	93
References	99
Curriculum Vitae	107

LIST OF TABLES

Table 3.1: Constant model parameters used in framework IPMC simulations	18
Table 3.2: Summary of primary modeling differences between electromechanical and mechano-electrical transduction in IPMC actuators	19
Table 3.3: Force coupling coefficients for back-relaxation modeling	23
Table 3.4: Material properties used for solid mechanics model for tube-shaped IPMCs	31
Table 3.5: Parameters used during tube-shaped IPMC simulations	36
Table 4.1: Value of IPMC actuator model constants for electrode effects modeling	46
Table 5.1: Activation process of ionomer cilia fibers	63
Table 5.2: Die sizes used for down-scaling the size of cylindrical EAP fibers	65
Table 5.3: Parameter values used in simulations of EAP fibers	70
Table 6.1: Simulation results of free-end displacement and electrode signal of a rectangular IPMC fluid-structure interaction for various flow velocities for a rectangular IPMC of dimensions 10mm x50mm x0.5mm	78
Table 6.2: Values used in simulations for cation/anion-exchange membrane comparisons	83

LIST OF FIGURES

Figure 2.1: Experimental example of back-relaxation of an IPMC actuator (50mm x 10mm x 0.5mm) completely submerged in deionized water in response to a constant 3 V input	8
Figure 2.2: Conceptual illustration of a complex three-dimensional shaped, electrically controllable artificial muscle (AM) actuator. Reprinted from <i>Polymer</i> , 43(3), Kim, K.J., and Shahinpoor, M., “A novel method of manufacturing three-dimensional polymer-metal composites (IPMCs) biomimetic sensors, actuators and artificial muscles”, 797-802, (2002), with permission from Elsevier	9
Figure 3.1: Schematic of the IPMC polymer structure and hydrated cation migration within the polymer network for electromechanical transduction	12
Figure 3.2: Electromechanical response of a rectangular IPMC to input of a 4.0 V peak-to-peak sinusoidal electrode potential (blue dotted curve) at 1 Hz frequency	20
Figure 3.3: Mechanoelectrical response of a rectangular IPMC to input of a 10.0 mm peak-to-peak sinusoidal tip-displacement (blue dotted curve) at 1 Hz frequency	21
Figure 3.4: Illustration of the IPMC electromechanical experimental setup	23
Figure 3.5: Experimental and simulated IPMC displacement at measured location of 6mm above the free-end in response to 1V, 2V, and 3V DC actuation	24
Figure 3.6: Simulated electromechanical frequency response of a 20mm x 5mm x 0.25mm rectangular IPMC actuator at 2V peak-to-peak and 4V peak-to-peak sinusoidal inputs	25
Figure 3.7: Simulated mechanoelectrical frequency response of a 20mm x 5mm x 0.25mm rectangular IPMC sensor at 5mm and 10mm peak-to-peak sinusoidal inputs	26
Figure 3.8: Simulated mechanoelectrical frequency response of a 20mm x 5mm x 0.25mm rectangular IPMC sensor at 2mm and 4mm peak-to-peak sinusoidal top-face shear inputs	27
Figure 3.9: IPMC tip geometry and mesh used in finite element simulations of tube-shaped IPMCs	30
Figure 3.10: Schematic of cross-section of the extruded Nafion tubes (not to scale): <i>Left</i> : illustration. <i>Right</i> : a photograph of experimental sample	32
Figure 3.11: Photograph of a tube-shaped IPMC sample	33
Figure 3.12: Wire soldered to copper foil (<i>left</i>), and copper foil attached to nylon collet (<i>right</i>)	34
Figure 3.13: Mounting system for cylindrical IPMC sensors (<i>left</i>), and sensor experimental setup (<i>right</i>)	34
Figure 3.14: Illustration of the IPMC mechanoelectrical experimental setup	34

Figure 3.15: Experimental results of tube-shaped IPMC sensors for sinusoidal tip displacement input of 0.5 mm amplitude (<i>left</i>), and results for tip displacement input of 1.5 mm amplitude (<i>right</i>). Frequency at 1 Hz	35
Figure 3.16: Simulation compared to experimental results of tube-shaped IPMC sensors for sinusoidal tip displacement input of 0.5 mm amplitude (<i>left</i>), and for tip displacement input of 1.5 mm amplitude (<i>right</i>). Frequency of 1 Hz	37
Figure 3.17: Cation concentration near fixed end at max bending input (<i>left</i>), and anion concentration near fixed end at max bending input (<i>right</i>). Input is tip displacement at 1.5 mm amplitude, 1 Hz	37
Figure 3.18: Ion concentrations across vertical center line of tube-shaped IPMC	38
Figure 3.19: Simulated cation concentration rise near the polymer electrode interface at max displacement for the given IPMC transduction cases	39
Figure 3.20: Input tip displacement for complex sensor signal simulation example (<i>left</i>), and x-y plane of the given tip displacement input (<i>right</i>). The arrow indicates direction of increasing time	40
Figure 3.21: Simulated signal of the top electrode with the bottom electrode grounded for the input tip motion shown in Fig. 3.20 over two cycles	41
Figure 4.1: Cross-section SEM images of the IPMC	43
Figure 4.2: Comparison between the simulation results and experimental results of the electrode resistance change	46
Figure 4.3: Comparison of experimental results of IPMC strain with model predictions, with and without consideration of surface resistance change	47
Figure 4.4: Meshes used in finite element simulations: (a) mesh sparsely mapped along length; (b) triangulated mesh	48
Figure 4.5: IPMC strip displacement for one cycle during steady-state response for a sinusoidal voltage input of 4 V peak-to-peak amplitude and 1 Hz frequency using the variable electrode properties model	52
Figure 4.6: Simulation result of the IPMC tip displacement using the variable electrode properties model	52
Figure 4.7: Simulation result of the IPMC cation concentration using the variable electrode properties model: (a) near top electrode, (b) near bottom electrode	53
Figure 4.8: Simulation results of cation concentration along the thickness of IPMC using the variable electrode properties model	54
Figure 5.1: Fabrication of cylindrical electroactive ionomer fibers by melt-drawing process	63

Figure 5.2: Experimental setup used for measuring the displacement of electroactive ionomer fiber under external electric field	64
Figure 5.3: Digital optical microscope images of the fabricated EAP microfibers in different sizes	65
Figure 5.4: Applied voltage and measured displacement response of a cylindrical EAP fiber micro-actuator at 5 V AC square-wave at 0.1 Hz (<i>left</i>) and 1 Hz (<i>right</i>) operating frequencies in 0.1 M LiCl aq. solution at 10 mm electrode spacing	67
Figure 5.5: Displacement response versus applied voltage for a cylindrical EAP fiber micro-actuator at 5 V AC square-wave at 0.1 Hz operating frequency in 0.1 M LiCl aq. solution at 10 mm electrode spacing .	67
Figure 5.6: Illustration of actuation mechanism of an electrodeless EAP fiber in electrolyte solution under an imposed electric field (<i>a</i>), with a schematic of the actuation mechanisms of a traditional IPMC for contrast (<i>b</i>)	68
Figure 5.7: Finite element simulations of an EAP fiber in electrolyte solution as actuated by a 5V, 1Hz square wave applied to electrodes spaced 10 mm apart with comparison to experimental results (<i>left</i>), and a close-up of the mesh used for simulations on the free-end of the fiber (<i>right</i>)	71
Figure 5.8: PDMS substrate with pre-drilled 50- μ m holes for placement of EAP microfibers (<i>a, b</i>), process of fixing the ionomeric cilia fibers into a PDMS substrate (<i>c, d, e</i>), and digital optical microscope images of fabricated prototype AM cilia array with 1 mm spacing in between artificial cilia fibers (<i>f, g</i>)	72
Figure 5.9: Clamp device with 6 external Pt electrodes for actuating the cilia (1x20) array by external field (<i>a</i>), and the artificial cilia array (1x20) mounted between electrodes and immersed in electrolyte solution (<i>b</i>)	73
Figure 5.10: Experimental results for a microfiber array actuated by separated electrodes at 5 V AC, 0.5 Hz square wave input applied to electrodes spaced 3.6 mm apart. Still photograph from video at times $t=1.3$ seconds (<i>a</i>), $t=1.8$ s (<i>b</i>), $t=2.3$ s (<i>c</i>), $t=2.8$ s (<i>d</i>), $t=3.3$ s (<i>e</i>), $t=3.8$ s (<i>f</i>), and measured tip-displacement measurements of an individual fiber of the array (<i>g</i>)	74
Figure 6.1: Simulated streamlines for the 0.1 m/s flow velocity condition	77
Figure 6.2: In-lab all-vanadium redox flow battery system for experimental investigation	80
Figure 6.3: All-vanadium redox flow battery experimental results for cycles 2 through 4 of charging/discharging at 40 mA/cm ² with a volume of 15 ml of electrolyte in each reservoir and a flow rate of 10 ml/min	80
Figure 6.4: Preliminary simulation results of electrolyte potential for charging (<i>left</i>) and discharging (<i>right</i>) cycles	81
Figure 6.5: Preliminary simulation results of electrode potential for charging (<i>left</i>) and discharging (<i>right</i>) cycles	81
Figure 6.6: 1D simplified geometry for rapid-simulation comparison of actuator components	83

Figure 6.7: Simulated cation concentration for mobile-cation (traditional) type IPMC actuator across 1D domain (*left*) and in a small, near-boundary region (*right*) for mobile-cation type IPMC actuators 84

Figure 6.8: Simulated cation concentration change at right-most boundary of a mobile-cation IPMC in response to a 0.5 V, 1 Hz input signal across a 0.5 mm domain 85

Figure 6.9: Simulated anion concentration for a mobile-anion type IPMC actuator across 1D domain (*left*) and in a small, near-boundary region (*right*) for mobile-cation type IPMC actuators 86

Figure 6.10: Simulated anion concentration change at right-most boundary of a mobile-anion IPMC in response to a 0.5 V, 1 Hz input signal across a 0.5 mm domain 86

Figure B.1: Bending diagram (*left*) and the simple shear strain diagram (*right*) used for strain derivations 91

CHAPTER 1. INTRODUCTION

Ionic polymer-metal composites (IPMCs), a type of electroactive polymer (EAP) which exhibit large deformation at low operational power, have been of great interest in development of actuation and sensor applications for over 2 decades [1-3]. These studies have included implementing IPMCs for use in robotics, microfluidics, and medical applications such as active catheters [4-11]. IPMCs are of interest to many studies and soft-robotic applications because of large controllable deformations at a low operating voltage, referred to as electromechanical transduction.

Alternatively, they may be used to measure an electric response for a given deformation [3, 12]. This allows IPMC devices to be developed into actuators and sensors, which can also be made into self-sensing actuators [13-16]. Furthermore, fabrication techniques have improved which allow much smaller IPMC devices and IPMCs of complex geometries to be made. Given the characteristics of IPMCs and these recent advances, advanced lightweight robotic devices of fundamentally interactive characteristics can be made with a complete understanding of the underlying physics. However, a large part of this progress is in fabrication and experimental studies, with little insight to the governing physics. Due to the complicated nature and small size scale of the ion-transport and deformation problem in electroactive polymers, experimentally visualizing the underlying phenomenon is difficult and not often performed [17]. Finite element analysis simulations can offer a significant tool for further understanding the physical characteristics of such devices.

Several studies have focused on electroactive polymer modelling and have developed models for IPMCs. However, for the large part these models are restricted to experimentally calibrated models for individual IPMC devices, being primarily empirical in form. This provides a useful tool for modeling applications in dynamics and controls of specific cases of electroactive polymer actuation, but these types of models do not provide any additional insight into the governing physical mechanisms of these

devices. Additionally, the previous physics-based models are limited in applicability for complex geometry IPMCs and are semi-empirical in the case of electromechanical transduction. This research project is focused on physics-based modeling to provide a deeper insight to the underlying physics by offering simulation tools to investigate the material properties, geometry, and governing mechanisms involved.

This study provides a coupled physics-based model for IPMC devices of complex shapes and differing applications. This will allow researchers to understand more fully the performance and optimize fabrication techniques for these devices. Moreover, it has potential commercialization due to the potential increased accuracy and better performance obtainable by means of computational optimization. An experimental study has been done to verify simulation results and determine accuracy of model predictions. Furthermore, many similarities exist in the fundamental physics governing flow batteries and IPMC devices. Therefore, this study also includes modeling of flow battery systems.

Much effort has been devoted to addressing certain issues with IPMC models that have hampered further development and understanding. However, there are several key issues that remain unclarified in currently published research on the topic. This study will focus on these issues, namely the issues of solid mechanics and ion transport physics in Chapter 3, back relaxation (in response to a constant electric field, the actuator reaches a maximum displacement before “relaxing” backwards, often surpassing the equilibrium position) in Chapter 3, sizing and geometrical effects in Chapters 3-5, and electrode effects in Chapter 4.

1.1 Problem Statement

The present study seeks to address the challenges impeding further development and design of IPMC transducers through physics-based modeling with specific emphasis on existing model shortcomings. The objective is to provide a thorough physics-based model which is adaptive to several specific aspects of IPMC transduction. The underlying physical mechanisms responsible for each of these aspects is studied and discussed herein. This approach will provide researchers and developers with a further understanding and the knowhow to design more effective devices with IPMCs. Numerical modeling in this study was done by finite element analysis (FEA) and executed with COMSOL Multiphysics versions 4.3 through 5.2. Experimental setups were designed for model verification. Simulation results are presented in comparison to experimental data. The accuracy of the models is discussed; in general, the simulation results can be said to show good agreement with experimental data. This work is expected to provide researchers in subjects of soft-robotics and ionic-transport device development with simulation methods to assist in performance analysis, design, and development of ion migration based electroactive polymer devices.

This dissertation is organized as follows. First, a review is presented of IPMC development, the significance modeling has played in its progression, and the current issues hampering further advancement in the field. Then the chapters are organized starting with the fundamental physics-based backbone of the IPMC model. The fundamental backbone of the IPMC model relates the ion transport physics, electrical potential, and solid-mechanics to achieve dynamic models for IPMC actuation and sensing; the actuation and sensing models both utilize the same underlying physics, namely the Poisson-Nernst-Planck equations for ion transport and electrical potential along with a linear elastic material solid-mechanics model for IPMC deformation. Additionally, this chapter includes focus on several important issues, including back-relaxation. A paper by the author published in Journal of Applied Physics (Stalbaum, T., Pugal, D., Nelson, S. E., Palmre, V., and Kim, K. J., "Physics-based modeling of

mechano-electric transduction of tube-shaped ionic polymer-metal composite," *117*(11), 114903, 2015) is included in this chapter to highlight tube-shaped IPMC sensors. This dissertation author is first-author of this paper and did much of this work. The next several chapters contain modeling adaptations of the fundamental IPMC model to highlight specific existing issues hampering IPMC development, including a chapter focused on electrode effects which includes another *Journal of Applied Physics* paper (Shen, Q., Palmre, V., Stalbaum, T., and Kim, K. J., "A comprehensive physics-based model encompassing variable surface resistance and underlying physics of ionic polymer-metal composite actuators," *118*(12), 124904, 2015). This dissertation author is third-author on the above paper and contributed primarily to the physics-based modeling and overall discussion. Following this chapter, a chapter focused on electrodeless, biomimetic EAP actuators is included. This chapter includes a paper accepted for publication from the *Marine Technology Society Journal* (Kim, K.J., Palmre, V., Stalbaum, T., Hwang, T., Shen, Q., and Trabia, S, "Promising developments in marine applications with artificial muscles: electrodeless artificial-cilia microfibers," accepted for publication). This dissertation author is third-author on this paper and contributed primarily to modeling and overall discussion. Each chapter that contains published material begins with a short description emphasizing the importance of the work and relevance to this study. Additionally, specific author contributions are highlighted at the beginning of chapters that contain previously published material. Finally, a chapter offering special case example applications of the overall modeling framework is presented, which includes modeling and discussion of prospective Vanadium Redox Battery (VRB) systems, IPMC interaction with fluid flow, and a section on mobile-anion based IPMCs. The remaining two chapters contain concluding remarks made together with suggestions for future work.

CHAPTER 2. BACKGROUND

Artificial muscles have been a subject of rapid development for over a century, with possibly the earliest contributions from Roentgen [18]; although the term dates back into the early 19th century [19]. The term artificial muscle has become nearly synonyms to soft-robotic actuators and electroactive polymer devices. Albeit apart from direct application as artificial muscles, these developed actuators have been suggested for a wide range of applications, including but not limited, to underwater actuators, interplanetary actuators, and medical instruments such as active catheters. Additionally, there has been a large focus in biomimetic research of aquatic life; for example, such devices have been suggested for use to mimic swimming motions of fish, jellyfish, and mimicry of dolphin skin to reduce surface drag with sub-dermal actuators. Research in electroactive polymers has had a major impact on the development of such devices [1].

Ionic polymer-metal composite actuators, an electroactive polymer device, are one of the primary candidates for the aforementioned applications. The fundamental mechanism of electromechanical transduction of IPMC materials is a localized swelling deformation caused by the redistribution of positively charged ions and water molecules within a polymer membrane due to an applied electrical field [20, 21]. This creates an electrically controllable deformable soft-substrate, and hence a soft-robotic actuator. Conversely, IPMC materials can be used as kinematic sensors to measure a given deformed state or motion by measuring the induced electric field at embedded electrodes [12].

Other electroactive polymers such as dielectric type EAPs, electrorheological fluids (ERF), ionic polymer gels (IPG), and several others work based on either ionic motion, similar to an IPMC, or by coulomb forces [22]. Dielectric EAPs are composed of a low-stiffness polymer with very high dielectric constant that can achieve good output forces and strains; however, a high voltage input which is close to the material breakdown strength and creates safety issues is required; hence, further development is

needed to effectively use this type of EAP [22]. Electrorheological fluids are a mixture of particles and fluid of different dielectric constants, which when in the presence of an electric field, the particles form chains due to an induced dipole moment. This changes the materials viscosity drastically, allowing the ERF to change consistency from a liquid to a gel. These types of EAP have been used in developing shock absorbers, damping systems, and variable flow pumps [22]. For a thorough characterization and comparison of the many existing EAP technologies, the reader is recommended to J.D.W. Madden 2004 [23]. Alternatively, IPMCs are of very unique characteristics with regard to the other available EAP devices. They offer low power input, high bending deformation, and they operate well in aquatic and hydrated environments [1]. However, a complete and thorough physics-based understanding of this type device is still being sought by the EAP community with emphasis on existing model shortcomings; therefore, IPMC devices have been selected as the focus of this study. This study addresses several of the existing IPMC modeling issues in the topics covered by the chapters herein.

Development of models for predicting the response of IPMC actuators and sensors has provided insight to the working mechanisms of these devices. Early models were made in a black-box, or grey-box modeling approach; that is, they were either wholly or partially empirical. These models are useful in predicting transducer response. These models have been successfully implemented into control electronics using both feed-forward and feedback loop controls to achieve high-precision and accuracy actuator devices [24-29]. Empirical modeling was the first step towards enabling application of IPMCs in robotic devices; however, they do not provide deeper information to the underlying physics and working mechanisms. Furthermore, these models cannot, without accompanying characterization studies, assist developers in advancing technologies in IPMC device design and fabrication.

Partially physical, semi-empirical, and some fully physics-based models have also been presented. These offer a great deal of insight into the working mechanisms of IPMCs and can help developers investigate design criteria to optimize response of a specific electroactive device. As one might expect,

many of the advances in IPMC research have come from these studies of the underlying device physics. It enables researchers to have key insight to desirable material characteristics, geometrical design, electrode fabrication, and design efficiencies. However, there are still several key issues hampering further understanding and development, such as coupling of solid mechanics to ion transport physics in actuation of IPMCs, back relaxation during actuation, sizing and geometrical effects, and electrode effects. This study attempts to investigate these issues to help advance modeling of such devices. A thorough physics-based understanding of these phenomena will advance the applicability and usefulness of IPMC materials as dynamic transducers.

In particular, the issue of back-relaxation during actuation can be considered one of the primary problems delaying application of IPMC actuators in industrial robotic and spacecraft operations. It can be observed that the initial response to a constant DC voltage of an IPMC tip-displacement quickly reaches a maximum, followed by a slow return towards the initial position, without reaching this position and maintaining an amount of residual deformation. An example experimental trace depicting this issue is shown in Fig. 2.1. If the applied electric field is removed, it bends further toward the initial position and may surpass it, ending at another deformed state. This creates issues in applications of IPMC actuators because at constant charge the response is non-steady, making maintaining a static position very difficult. This phenomenon can be attributed to the internal pressure-induced water diffusion through the swollen polymer into the electrode and past the solid-liquid interface. This is described in section 3.5.

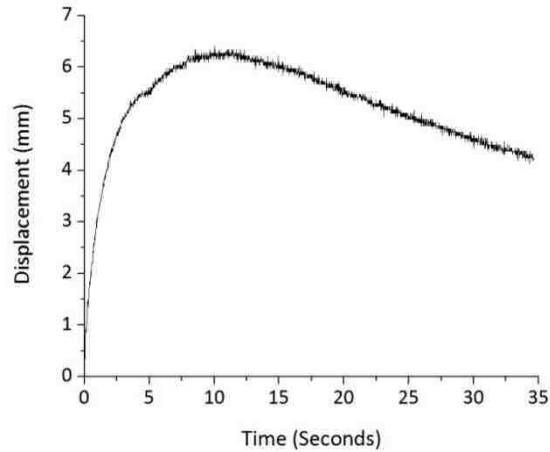


Figure 2.1: Experimental example of back-relaxation of an IPMC actuator (50mm x 10mm x 0.5mm) completely submerged in deionized water in response to a constant 3 V input

Additionally, a thorough understanding of the geometrical and sizing effects in ion transport and deformation of IPMC devices would be helpful to develop more complex or micrometer scale types of these devices [24, 30]. It is clear that thicker actuation devices result in lower bending displacement than thin samples due to the increased mechanical structural rigidity from an increased area moment of inertia [31]. However, there should be a contribution from ion concentration changes that are relative to the cross-sectional geometry as well, because the primary contribution to the IPMC actuation physics is commonly accepted to be due to a highly concentrated region of collected cations and water molecules in a very narrow region near the swollen electrode, which agrees with physics-based simulations [32]. Scaling down IPMC actuators has been suggested for applications in robotics and medicine, with one such example being a guided operational tool for surgical operations [24, 33]. Furthermore, understanding IPMC deformation in complex shaped devices, such as that suggested by Kim and Shahinpoor [34] as shown in Fig. 2.2, would facilitate research and development of such devices, which are currently unrealizable due to fabrication restrictions; however, a thorough physics-based understanding and confirmation of the theory have also not yet been developed. This is a topic of exploration and is highlighted throughout Chapters 3 through 5.

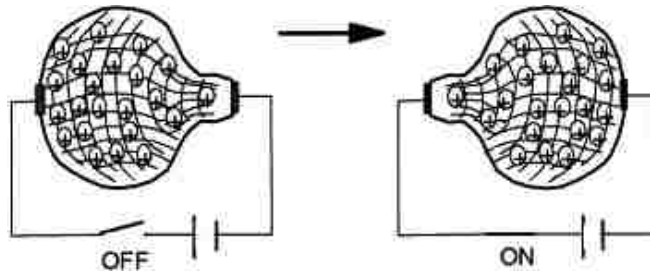


Figure 2.2: Conceptual illustration of a complex three-dimensional shaped, electrically controllable artificial muscle (AM) actuator. Reprinted from *Polymer*, 43(3), Kim, K.J., and Shahinpoor, M., “A novel method of manufacturing three-dimensional polymer-metal composites (IPMCs) biomimetic sensors, actuators and artificial muscles”, 797-802, (2002), with permission from Elsevier [34]

Furthermore, much effort has been devoted within the smart material community into investigating the electrode properties and plating techniques used to fabricate IPMCs [35]. Adaptations to the physics-based models to incorporate electrodes more accurately have been presented. Specifically, models have been developed which include the varying electrical properties of the electrodes during bending of the IPMC, such as the resistance and capacitance, due to the local strains, which affect the response of the IPMC. These effects have been reported and a model was presented [36, 37]. In this study, these models have been incorporated into the fundamental physics-based model to achieve a more thorough understanding of the electrode effects, including in Chapter 4. This model can assist developers in understanding the advantages and disadvantages of different electrode fabrication and plating techniques and how they affect the response of the actuator.

Another industry which has shown great interest in the development of smart transduction devices, with specific interest in IPMCs, is the Navy and maritime transportation industries. For many years systems have been developed for environmental monitoring of waters surrounding a ship or submerged object; however, to date such devices are costly, bulky in mechanical equipment and/or electronics, and are prone to low spatial resolution. This has rendered their application in maritime travels mostly unjustified. In this study, an IPMC sensor is investigated under the presence of flow fields in a flow

channel designed for mechanoelectric sensor experiments. A physics-based model has been developed to encompass the fluid-structure interaction effects. A discussion of the modeling differences and issues is presented in Chapter 6. These devices show high dynamics response, high spatial resolution, and limited electronics requirements. Furthermore, application of such devices in an arranged multiple micro-sensor array can be coupled with micro-jets to create an appropriate feedback system to monitor and control the flow around an object.

Another interesting application of the diffusion, migration, and charge physics modeling framework is in describing the working phenomenon of flow battery devices. These devices employ an ionomeric membrane, similar to IPMCs this is typically selected as Nafion, to separate two species of electrolyte and allow transport of H^+ ions while other ions are confined by this boundary. The modeling framework developed in Chapter 3 is governed by the same physics as the transport aspects of flow batteries, and thus expansion of the IPMC modeling framework to encompass flow battery devices, specifically the all-vanadium reduction oxidation (redox) battery (VRB), has been included in this study and is presented in Chapter 6.

Moreover, it has been of interest to the smart material research community to develop anion-type IPMC devices; that is, IPMC devices which have freely mobile negative ions with its positive ions bonded to the polymer backbone. This type of anion exchange membrane has shown promise in the fuel cell and flow battery research communities due to high performance properties at a range of temperatures. Using the modeling framework developed for cation-exchange IPMCs, a simple change of the modeling variables and parameters can encompass this effect, and is presented in Chapter 6. Such a model is expected to provide researchers and developers with a better understanding with regards to governing mechanisms and performance of IPMCs with anion-exchange membranes.

CHAPTER 3. SENSING AND ACTUATION FRAMEWORK FOR IONIC POLYMER-METAL COMPOSITES

This chapter covers the actuation and sensing framework of exemplar cases in ionic electroactive polymer transduction, specifically those of rectangular and tube-shaped IPMC actuators and sensors. Rectangular IPMCs are the most commonly utilized for actuators and sensors due to simplicity in fabrication; however, tube-shaped IPMCs are of great interest for multi-directional actuation and sensing transduction and the ability to transport species through the center hole.

In this section, a research paper published in *Journal of Applied Physics* is included. This study covers finite element modeling of tube-shaped IPMC sensors in great detail, with good agreement between experimental and simulation results, and includes a detailed explanation of the governing physics for the framework of IPMC finite element analysis. The tube-shaped IPMC is of great interest due to the capability of multi-directional actuation and sensing. The simulation results provide insight to the ion migration and deformation mechanisms of a tube-shaped IPMC sensor. The authors, in order of appearance on the article, are Tyler Stalbaum, David Pugal, Shelby E. Nelson, Viljar Palmre, and Kwang J. Kim. Reprinted from *Journal of Applied Physics*, Stalbaum, T., Pugal, D., Nelson, S. E., Palmre, V., and Kim, K. J., "Physics-based modeling of mechano-electric transduction of tube-shaped ionic polymer-metal composite," *117*(11), 114903, (2015), with the permission of AIP Publishing.

The primary contributions to the physics-based modeling are from TS, DP, and KJK. The experimental work was mostly done by SEN and VP with help from TS. The data analysis, simulations, conclusions, and discussion were primarily done by TS and VP.

3.1 Ionic Polymer-Metal Composite Governing Physics

The polymer membrane of an IPMC consists of anions fixed to the polymer backbone and freely positioned positive ions, or cations. In a hydrated state, micro-channels in the polymer expand to allow free transport of cations and attracted water molecules through the membrane. When a voltage is applied to IPMC electrodes, the cations migrate away from the anode, dragging the attracted water molecules with them. This causes osmotic pressure change with localized swelling near the cathode interface and contraction near the anode, which results in an overall deformation of the IPMC. A basic schematic of an IPMC polymer structure and electromechanical transduction phenomenon is shown in Fig. 3.1.

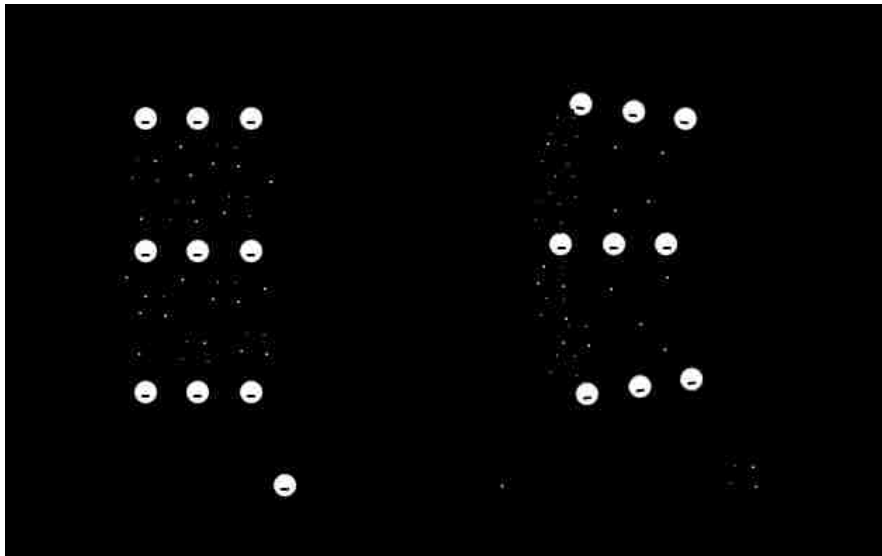


Figure 3.1: Schematic of the IPMC polymer structure and hydrated cation migration within the polymer network for electromechanical transduction

The underlying cause of IPMC electromechanical and mechanoelectrical transduction is induced ion migration and resulting charge density in the vicinity of the electrodes. Ionic current in the polymer for both cases can be described by the Nernst-Planck equation, which is a conservation equation for describing the ion fluxes based on concentration changes and electric field [20]. For a single species

absent of chemical reaction, the following species flux terms are of significance to describe the transport of cations through the IPMC polymer membrane:

$$\mathbf{j}_{diffusion} = -D\nabla C \quad (3.1)$$

$$\mathbf{j}_{migration\ in\ electric\ field} = -z\mu FC\nabla\phi \quad (3.2)$$

$$\mathbf{j}_{convection} = \mathbf{u}C \quad (3.3)$$

where $\mathbf{j}_{diffusion}$ is the cation diffusive flux, $\mathbf{j}_{migration\ in\ electric\ field}$ is the cation flux due to migration in the electric field, $\mathbf{j}_{convection}$ is the cation convective flux, C is cation concentration, D is the diffusion coefficient, F is Faraday's constant, z is the charge number, and ϕ is the electric potential in the polymer. The cation mobility, μ , can be expressed as D/RT , where R is the gas constant and T is the absolute temperature. The cation velocity, \mathbf{u} , can be expressed in terms of the solvent pressure gradient as:

$$\mathbf{u} = -\mu V_C \nabla P \quad (3.4)$$

where V_C is the molar volume which quantifies the cation hydrophilicity and ∇P is the solvent pressure gradient. The change of cation concentration with time can be expressed by performing a species flux balance over a given volume; that is, the sum of the species flux gradients and time derivative of species concentration must equal to zero. Thus, the time-dependent transport of cations in the IPMC polymer membrane can be described by the Nernst-Planck equation as:

$$\frac{\partial C}{\partial t} + \nabla \cdot (-D\nabla C - z\mu FC\nabla\phi - \mu CV_C \nabla P) = 0 \quad (3.5)$$

An important difference between IPMC electromechanical and mechanoelectrical transduction is the magnitude, direction, and significance of individual terms in Eq. (3.5). Besides the concentration time derivative, the terms of Eq. (3.5) consist of three flux terms governed by the field gradients of electric potential, concentration, and solvent pressure. In case of actuation, the electric potential gradient term is significantly more prevalent than the solvent pressure flux, that is, $zF\nabla\phi \gg V_c\nabla P$, therefore the pressure flux term is often neglected in actuation model implementation. However, in case of sensing, these terms are of similar significance and neither should be neglected [21]. It is also interesting to note the direction of the electric potential gradient is opposite for sensing as compared to actuation because the ionic current is governed by an induced pressure gradient rather than an applied voltage.

The electric potential gradient term can be described by Poisson's equation:

$$-\nabla^2\phi = \frac{\rho}{\varepsilon} \quad (3.6)$$

where ε is the absolute dielectric permittivity and ρ is charge density defined as:

$$\rho = F(C - C_a) \quad (3.7)$$

where C_a is local anion concentration.

While the cation concentration C is governed by the Nernst-Planck Eq. (3.1), the anion concentration is related to local volumetric strain. The volume changes in the polymer matrix affect the local anion concentration because anions are fixed to the polymer backbone. Hence, the anion concentration C_a is expressed:

$$C_a = C_0 \left[1 - \left(\frac{\partial u_1}{\partial x} + \frac{\partial u_2}{\partial y} + \frac{\partial u_3}{\partial z} \right) \right] \quad (3.8)$$

where u_1 , u_2 , and u_3 are local displacements in the x , y , and z directions respectively, and C_0 is the initial ion concentration.

Eq. (3.5) and Eq. (3.6) comprise the Poisson-Nernst-Planck (PNP) model for IPMCs and describes the fundamental physics within the polymer membrane.

The linear elastic material model has been used to describe deformation of IPMCs. The constitutive relation of Hooke's Law was used to relate stress and strain in the polymer as:

$$\begin{bmatrix} \sigma_{11} \\ \sigma_{22} \\ \sigma_{33} \\ \sigma_{12} \\ \sigma_{23} \\ \sigma_{13} \end{bmatrix} = \begin{bmatrix} 2\mu_L + \lambda & \lambda & \lambda & 0 & 0 & 0 \\ \lambda & 2\mu_L + \lambda & \lambda & 0 & 0 & 0 \\ \lambda & \lambda & 2\mu_L + \lambda & 0 & 0 & 0 \\ 0 & 0 & 0 & \mu_L & 0 & 0 \\ 0 & 0 & 0 & 0 & \mu_L & 0 \\ 0 & 0 & 0 & 0 & 0 & \mu_L \end{bmatrix} \begin{bmatrix} \varepsilon_{11} \\ \varepsilon_{22} \\ \varepsilon_{33} \\ 2\varepsilon_{12} \\ 2\varepsilon_{23} \\ 2\varepsilon_{13} \end{bmatrix} \quad (3.9)$$

where ε_{ij} is the normal strain in the i -direction for $i = j$ and a shear strain for $i \neq j$. Stress terms σ_{ij} are defined similarly.

The constants μ_L and λ are Lamé's constants, defined as:

$$\mu_L = \frac{E}{2(1+\nu)}, \quad \lambda = \frac{\nu E}{(1+\nu)(1-2\nu)} \quad (3.10)$$

where E is Young's Modulus and ν is Poisson's ratio.

The system is in equilibrium if Navier's displacement equations are satisfied, given by the relation:

$$-\nabla \cdot \sigma = \mathbf{F} \quad (3.11)$$

where \mathbf{F} is the body force vector per unit volume.

Newton's Second Law is used to describe time-dependent deformation:

$$\rho_p \frac{\partial^2 \mathbf{u}}{\partial t^2} - \nabla \cdot \sigma = \mathbf{F} \quad (3.12)$$

where \mathbf{u} is the local displacement vector and ρ_p is the polymer density.

3.2 Modeling Approach

A physics-based model was developed to simulate ion concentration, polymer electric potential, charge density and displacement response to a low voltage input signal to obtain further insight into the underlying physics for rectangular IPMC actuators. The simulation utilizes the transport of diluted species, general form Partial Differential Equation (PDE), electric currents, and solid mechanics physics modules in COMSOL to achieve the desired governing set of PDEs. The transport of diluted species and general form PDE physics provide the Poisson-Nernst-Planck (PNP) set of coupled PDEs, which are used to describe cation concentration and electric potential within the polymer. A linear elastic material model with infinitesimal strain theory was implemented for the solid mechanics physics.

During electromechanical actuation of an IPMC by supplied voltage input to its electrodes, the main contribution to the deformation is assumed to be the cation migration and corresponding swelling effects. The contribution from the concentration gradient and electric potential are much larger than the contribution of the pressure gradient for electromechanical transduction and this term has been omitted from the Nernst-Planck equation, as expressed in (3.5). Poisson's equation as used in the model is expressed in (3.6). Furthermore, in electromechanical transduction, the change of anion

concentration is assumed to be very small in comparison with the change in cation concentration and hence the charge density is assumed to be a function of cation concentration only, expressed in (3.7) where C_a is kept fixed. A body force in the bending direction, which is assumed to be proportional to the charge density as $F_z = \alpha\rho$, is the input into the solid mechanics model. The solids mechanics describe the stress, strain, and local displacement. The governing solid mechanics equation used is expressed in (3.8), where ρ_p was taken as $\rho_p = 874 \text{ kg/m}^3$.

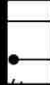

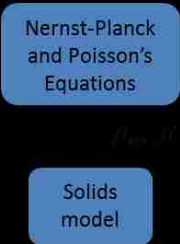
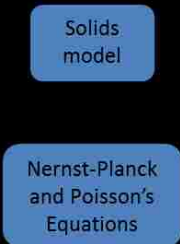
Because the material is assumed to deform primarily in the bending plane, plane strain deformation was assumed. The electromechanical model first utilizes (3.5), (3.6), and (3.7) to solve for the charge density, ρ . Then, (3.9), (3.10), and (3.11) are solved for the deformation. The mechano-electrical model is performed in the opposite order and first utilizes (3.9), (3.10), and (3.11) to solve for the stress and deformation throughout the polymer, and then (3.5), (3.6), and (3.7) are solved for the charge throughout the polymer and at the electrodes.

Effective dielectric permittivity values were varied to fit the mechano-electrical models. A proportionality coefficient of 0.0003 [N/C] was used for relating charge density in the polymer to body force for the electromechanical models. Additional modeling parameters are provided in Table 3.1. Table 3.2 summarizes the primary differences in IPMC modeling of electromechanical (actuation) or mechano-electrical (sensing) transduction types.

Table 3.1: Constant model parameters used in framework IPMC simulations.

Model parameter	Value
Diffusion coefficient, D	$5e^{-10} \text{ m}^2/\text{s}$
Faraday's constant, F	96,485 s·A/mol
Charge number, z	1
Molar volume change, V_c	$5e^{-4} \text{ m}^3/\text{mol}$
Gas constant, R	8.31 J/mol·K
Absolute temperature, T	293 K
Effective dielectric permittivity, ϵ	1.8 F/m
Initial ionic concentration, C_0	1,100 mol/m ³

Table 3.2: Summary of primary modeling differences between electromechanical and mechanoelectrical transduction in IPMC actuators.

Transduction mechanism		
Illustration of input / outputs		
Flow diagram of modeling approach	 <pre> graph TD A[Nernst-Planck and Poisson's Equations] --> B[Solids model] </pre>	 <pre> graph TD A[Solids model] --> B[Nernst-Planck and Poisson's Equations] </pre>
Important differences		

3.3 Experimental Procedure

IPMC sample preparation consists of four primary steps: (1) activation by hydrolysis reaction, (2) primary electrode plating by impregnation reduction, (3) secondary electrode plating by chemical deposition, and (4) ion exchange in the membrane. In case of rectangular IPMC samples, a thin film of cast Nafion can be purchased or fabricated. Further fabrication instructions are provided in section 3.5.3.

The experimental setups for IPMC electromechanical or mechanoelectrical transduction consist of 4 primary components: (1) a clamp for holding the IPMC and transferring electricity to the electrodes, (2)

a water tank for maintaining a hydrated environment for the IPMC, (3) an input device of a mechanical shaker for mechano-electrical experiments or a power supply for electromechanical experiments, and (4) a data acquisition system for measuring the desired output signal. For the case of electromechanical transduction experiments, the desired output signal is IPMC tip-displacement and is measured by means of a laser displacement sensor. In case of mechano-electrical transduction experiments, the desired output is the electrode signals and is measured by means of an amplified circuit and recorded in LabVIEW.

3.4 Results

Figure 3.2 and Fig. 3.3 are of experimental and simulated results for a rectangular IPMC actuator and sensor, respectively. The red curve is experimental and black dot-dashed curve is simulated tip-displacements for the case of actuation and electrode voltage response for the case of sensor. These results show good agreement for rectangular IPMC of dimensions $\sim 50\text{mm} \times 10\text{mm} \times 0.5\text{mm}$.

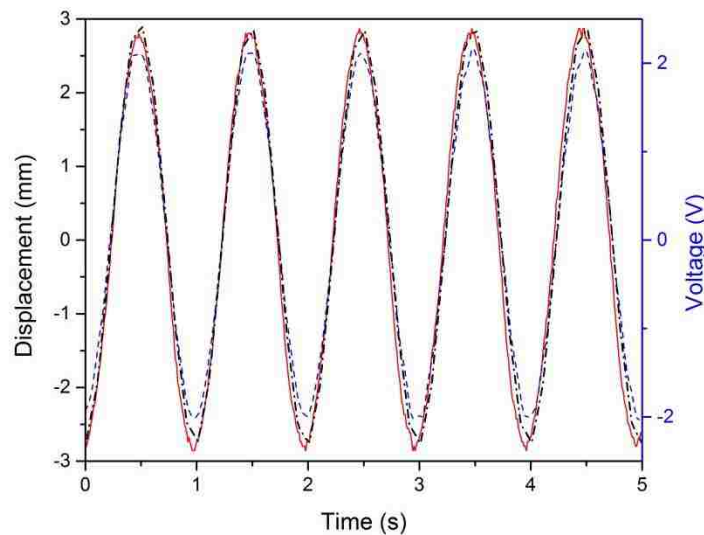


Figure 3.2: Electromechanical response of a rectangular IPMC to input of a 4.0 V peak-to-peak sinusoidal electrode potential (blue dotted curve) at 1 Hz frequency

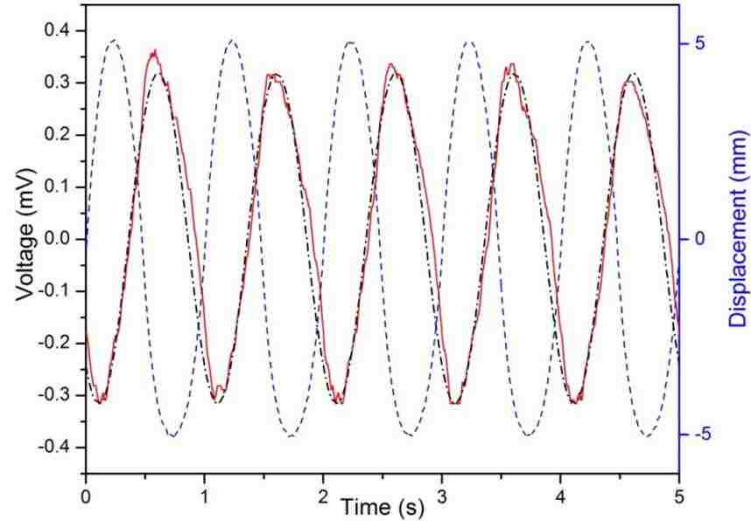


Figure 3.3: Mechano-electrical response of a rectangular IPMC to input of a 10.0 mm peak-to-peak sinusoidal tip-displacement (blue dotted curve) at 1 Hz frequency

3.5 Back-Relaxation

The issue of back-relaxation during actuation can be considered one of the primary problems delaying application of IPMC actuators in industrial robotic and spacecraft operations. It can be observed that the initial response to a constant DC voltage of an IPMC tip-displacement quickly reaches a maximum, followed by a slow return towards the initial position, without reaching this position and maintaining an amount of residual deformation. If the applied electric field is removed, it bends further toward the initial position and even may surpass it, ending at another deformed state. This creates issues in applications of IPMC actuators because at constant charge the response is non-steady, making maintaining a static position very difficult. This phenomenon has been attributed to the internal pressure-induced water diffusion through the swollen polymer into the electrode and past the solid-liquid interface.

Modifications are made to the IPMC modeling framework to include a time-varying body force which can represent the back-relaxation phenomenon. The force coupling component of the IPMC framework model has been utilized in previous works as a linear proportionality to the charge density inside the polymer, higher order proportionalities, or as follows [21]:

$$F_z = \alpha \frac{\text{sgn}(\rho)+1}{2} \rho^2 - \beta \frac{\text{sgn}(\rho)-1}{2} \rho \quad (3.13)$$

where $\text{sgn}(\rho) = +1$ for $\rho > 1$ and $\text{sgn}(\rho) = -1$ for $\rho < 1$, α and β are experimentally determined proportionality coefficients, and F_z is the body force in the direction of actuation. Using the force coupling of (3.13), originally proposed by D. Pugal [21], the higher order component is only applied near the electrode where $\rho > 1$; additionally, the linear portion is applied only where $\rho < 1$. In a similar fashion, one would like to include a relaxation force only near the swollen electrode, that is, the electrode that $\rho < 1$, because in the physical mechanisms of back-relaxation, it is expected the water diffuses through the swollen electrode, causing a relaxation in total force on that side. To encompass this effect, an additional term is included in the force coupling equation as:

$$F_z = \alpha \frac{\text{sgn}(\rho)+1}{2} \rho^2 - \beta \frac{\text{sgn}(\rho)-1}{2} \rho - k_r \frac{\text{sgn}(\rho)-1}{2} t \quad (3.14)$$

where k_r is the back-relaxation temporal coefficient, which can be thought of as a damping component within the given time range.

Simulations were developed in COMSOL Multiphysics 5.2 using the framework model of Chapter 3, with the force coupling equation given in (3.14), for an IPMC actuator in response to 1 V, 2 V, and 3 V inputs to compare with experimentally collected data. The coefficients α and k_r are calibrated per

experimental test to achieve best fit results. Parameter values used in simulations are given in Table 3.1. Fitted calibration coefficients are given in Table 3.3.

Table 3.3: Force coupling coefficients for back-relaxation modeling.

Model parameter	Response to 1 V input	Response to 2 V input	Response to 3 V input
α	$4.5e-9 \text{ N}\cdot\text{m}^3/\text{C}^2$	$1.4e-8 \text{ N}\cdot\text{m}^3/\text{C}^2$	$1.9e-8 \text{ N}\cdot\text{m}^3/\text{C}^2$
β	$3e-8 \text{ N/C}$	$1.2e-7 \text{ N/C}$	$2e-7 \text{ N/C}$
k_r	$0.07 \text{ N/s}\cdot\text{m}^3$	$0.19 \text{ N/s}\cdot\text{m}^3$	$0.24 \text{ N/s}\cdot\text{m}^3$

An IPMC actuator of dimensions width x length x height of 9.94mm x 51.07mm x 0.57mm was utilized for experimental measurements of DC response for 1 V, 2 V, and 3 V inputs. A schematic of the IPMC actuator experimental setup is shown in Fig. 3.4. The IPMC tip-displacement was measured at a location of 6mm above the free-end of the IPMC cantilever. The clamped region was measured to be roughly 10mm. Simulation results for displacement of a center location at 6mm above the free-end of the IPMC with a 10mm clamped region are shown in Fig. 3.5 with comparison to experimental measurements.

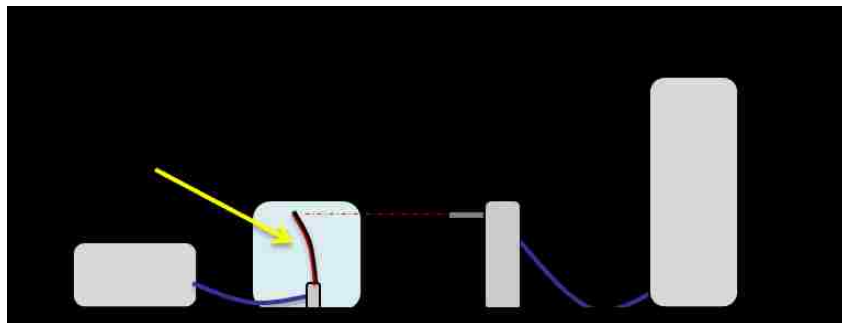


Figure 3.4: Illustration of the IPMC electromechanical experimental setup

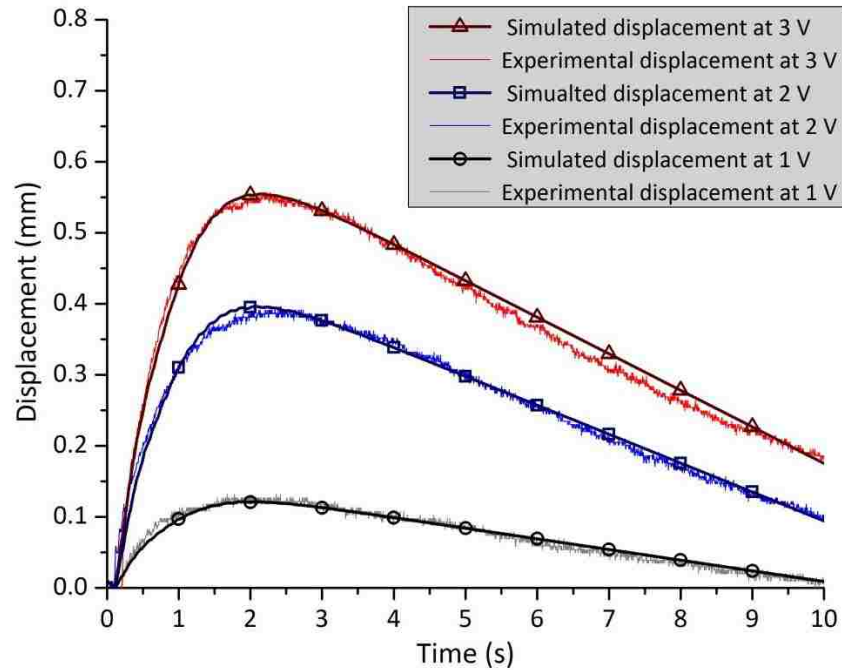


Figure 3.5: Experimental and simulated IPMC displacement at measured location of 6mm above the free-end in response to 1V, 2V, and 3V DC actuation

The simulation results and experimental results are in good agreement for the given range of input and parameter values utilized in simulations. It can be concluded that this form of force-coupling equation can be used to encompass the back-relaxation effects; however, it further complicates the force-coupling and must be implemented on a case-by-case basis. Furthermore, it should be noted that the difference between separations in the curves at 1 V to 2 V as compared to that of 2 V to 3 V could be attributed to several factors, specifically that at higher voltage, the bending displacement of the IPMC will reach a maximum bending saturation, that is, for any increase in voltage after this point, the IPMC will not exhibit larger bending response. In addition, the accuracy in the experimental voltage was near 0.1 V; therefore, the signal input values may be slightly inaccurate. This is also noticed in the parameter values, because these required a different value for each input voltage as can be seen in Table 3.2. This can be attributed to the difference in simulated as compared to experimental voltages.

3.6 Frequency Response of Ionic Polymer-Metal Composite Actuators

It is of great importance to understand the frequency response characteristics of an IPMC actuator for understanding the applicable range and expected transducer deformations. IPMCs are used within the range of 0.1 to 20 Hz [38]; therefore, this range has been selected for frequency analysis.

Simulations based on the modeling framework presented in this chapter using the parameter values as described in Table 3.1. Figure 3.6 shows the simulated frequency response curve for the typical operational range of an IPMC actuator at a sinusoidal input voltages of 2V and 4V peak-to-peak. IPMC dimensions of length x width x thickness of 20 mm x 5 mm x 0.25 mm with a 5 mm fixed region to represent the clamp.

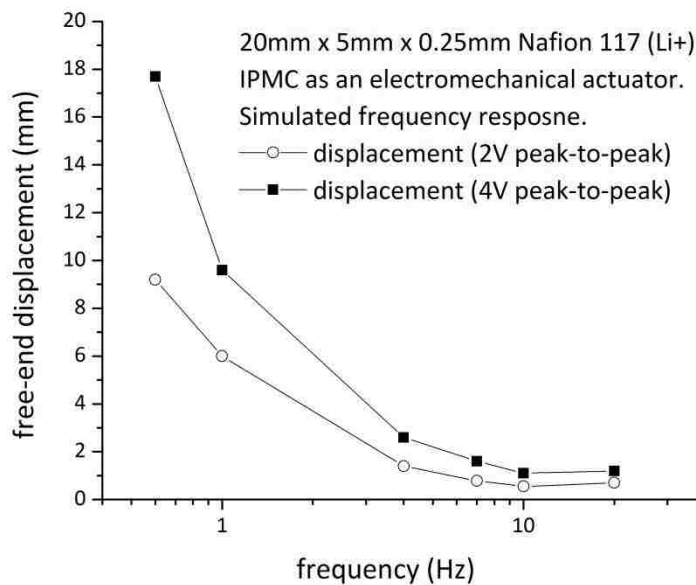


Figure 3.6: Simulated electromechanical frequency response of a 20mm x 5mm x 0.25mm rectangular IPMC actuator at 2V peak-to-peak and 4V peak-to-peak sinusoidal inputs

Similarly, simulated frequency response curves for an IPMC as a mechano-electrical sensor are provided in Fig. 3.7 for sinusoidal tip-displacement of 10 mm and 5 mm peak-to-peak amplitudes at a range of frequencies from 0.1 to 20 Hz. IPMC dimensions are the same as those used for Fig. 3.6., specifically of length x width x thickness of 20 mm x 5 mm x 0.25 mm.

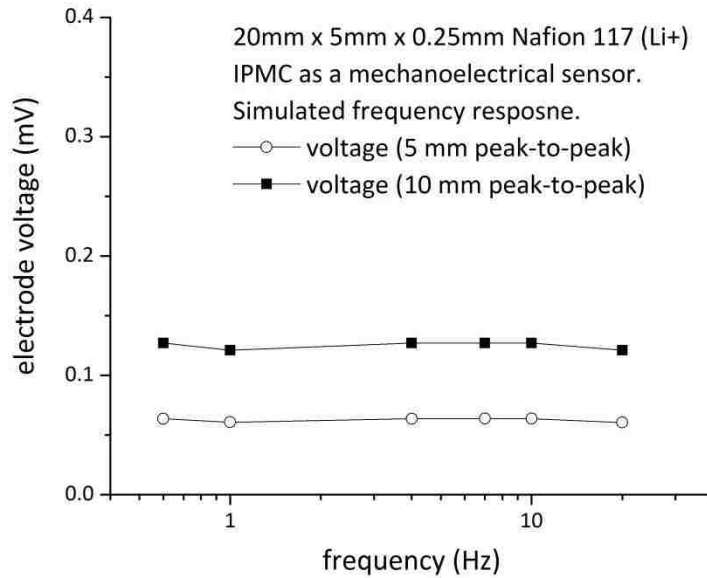


Figure 3.7: Simulated mechanoelectrical frequency response of a 20mm x 5mm x 0.25mm rectangular IPMC sensor at 5mm and 10mm peak-to-peak sinusoidal inputs

Several important observations can be made from Fig 3.6 and Fig 3.7. Figure 3.6 shows the response magnitude (free-end displacement) increasing with decreasing frequency, as would be expected of an actuator due to having a longer time period per charging and discharging cycle. Also note, the response increases slightly at 20 Hz, which can be attributed to a resonant frequency of IPMCs around 18 Hz [38]. However, in Fig. 3.7, the mechanoelectrical sensor frequency response characteristics display nearly unwavering response magnitude (electrode voltage) for change in frequency within the typical operational range. This can be attributed to the primary contribution to mechanoelectrical transduction in the Nernst-Planck equation, namely the change in anion location based on volumetric strain which is insensitive to operational frequency. Additionally, the frequency response as a sensor shows a slight decrease at 20 Hz, opposite of the increase seen in the actuator frequency response, which is likely also due to a resonant frequency around this value and corresponds to an increase in cation gradient near the electrodes, which acts against mechanoelectrical transduction in case of an IPMC as a sensor.

3.6.1 Response of an IPMC to Shear Loading

Mechanoelectrical transduction of an IPMC of dimensions 20mm x 5mm x 0.25mm in response to shear loading was also simulated for the range of frequencies of interest. The bottom face of the IPMC was held fixed, while the top face was given a prescribed sinusoidal displacement in the length direction of 2mm and 4mm peak-to-peak at a range of frequency from 0.1 – 20 Hz. Figure 3.8 shows the maximum peak-to-peak electrode voltage over the frequency range. Similar to that observed in bending mechanoelectrical transduction simulations, the magnitude of the response is nearly independent of the input frequency. As was previously proposed, this is likely due to the primary contribution to mechanoelectrical transduction in the Nernst-Planck equation is from the anion migration, and in-turn due to the volumetric strain, which is only dependent on particle position within the body and is insensitive to temporal effects. The very slight variation from the same value over the range of frequencies is likely caused by the alternative factors in the Nernst-Planck, namely the contributions from cation diffusive flux and migration acting against the magnitude of the sensor signal.

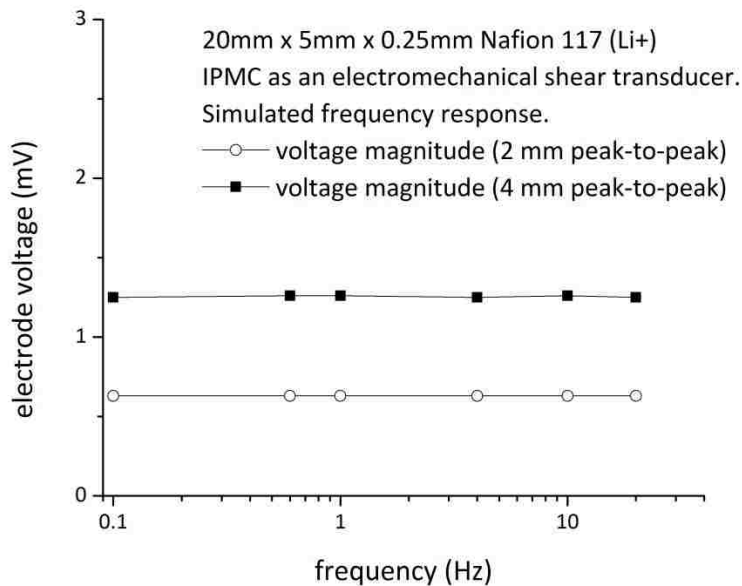


Figure 3.8: Simulated mechanoelectrical frequency response of a 20mm x 5mm x 0.25mm rectangular IPMC sensor at 2mm and 4mm peak-to-peak sinusoidal top-face shear inputs

Additionally, it is of interest to note that for the given example simulations, a 2mm peak-to-peak displacement in shear, where the top face moves in a prescribed sinusoidal motion and the bottom face remains fixed, shows a larger electrode response than for the 10mm peak-to-peak bending displacement of the free-end, given the actuators are of dimensions 20mm x 5mm x 0.25mm. To further investigate these results, Lagrangian strain has been calculated for both bending and shear cases. In solving for Lagrangian strain for both cases and comparing principal strains, one finds the principal strain of an IPMC of dimensions length L , width w , and height h under bending strain as:

$$\epsilon_{principal,bending} = \frac{h}{2r} + \frac{1}{2} \left(\frac{h}{2r} \right)^2 \quad (3.15)$$

where ϵ_{max} is the strain along the tensioned surface (bottom surface for positive y-direction free-end displacement), which is also the same for the case of bending as its principal strain, and r is the radius of curvature of the bent IPMC, which can be found by solving the following equation in an iterative method for r given free-end displacement and IPMC dimensions:

$$\delta = r \left[1 - \cos \left(\frac{L}{r} \right) \right] \quad (3.16)$$

where δ is the maximum free-end displacement of the input to the IPMC. Equations (3.15) and (3.16) are derived analytically using Lagrangian strain methods, assuming constant radius of curvature throughout the bent configuration. The volumetric strain can be given as the Jacobian of the given deformation; for the top surface during bending this is of the form:

$$J_{bending} = 1 - \frac{h}{2r} \quad (3.17)$$

For the case of shear input as described previously, assuming homogeneous deformation with the top surface moving and bottom fixed, the maximum principal strain calculated from the Lagrangian method is:

$$\epsilon_{principal, shear} = \frac{k^2}{4} \pm \frac{k}{2} \sqrt{\frac{k^2}{4} + 1} \quad (3.18)$$

where k is a nondimensional shear displacement, which is the ratio of the maximum displacement of the top face of the IPMC to the IPMC thickness ($k = \delta_{shear}/h$). It can be noted that the Jacobian is $J \approx 1$ for the case of shear loading, with very little to no volume change. Appendix B contains a detailed derivation of (3.15), (3.16), (3.17), and (3.18). In comparing (3.18) to (3.15), one can readily see the strain is much larger for the given case of shear as compared to bending for similar displacements, given the dimensions of the IPMC in question. This is observed in the value of the nondimensional shear displacement, which given an IPMC thickness of only 0.25mm, is large for even small top-face shear displacements, and it is to the second power in (3.18). Alternatively for bending strain, the value of r is typically quite large, that is, $h < 2r$, such that the strain is much less for similar displacements. This provides evidence for the large difference in simulated response for shear as compared to bending displacement response as observed in Fig. 3.7 and Fig. 3.8.

3.7 Finite Element Simulations of Tube-Shaped Ionic Polymer-Metal Composite Sensors

Tube-shaped ionic polymer-metal composite (IPMC) mechano-electrical transducers have been examined through simulation and experimental investigation for use as multi-directional sensor devices. COMSOL Multiphysics 4.3b is used to achieve 3D time-based finite element simulations including all relevant physics. A physics-based model is proposed to simulate mechano-electrical transduction of 3D

shaped IPMCs. Configuration of interest is a tube-shaped IPMC with multi-directional transducer capabilities. The fabricated IPMCs have an outer diameter of 1 mm and a length of 20-25 mm. Multi-directional sensing results are presented. Additionally, cation migration simulations provide keen insight into the differences in actuation and sensing phenomena in IPMC transducers. The cation rise in a very small (roughly 10 micrometers) sub-surface layer near the electrodes is several orders of magnitude larger in case of actuation than in case of sensing. Furthermore, the signal produced from sensing is of opposite charge direction as that provided as input for actuation to achieve the same displacement. However, cation rise is in the same direction, indicating anion concentration change as the primary effect in sensing. The proposed model is independent of general geometry and can be readily applied to IPMC sensors of other complex 3D shapes.

3.7.1 Model Implementation

3-dimensional finite element simulations were performed using COMSOL Multiphysics 4.3b software to couple mechanical deformation with ionic concentration, diffusion, and migration physics. The mesh used for all simulations was extra fine in the radial direction with a set node distribution along the edges and sparsely swept along the longitudinal direction. The mesh and IPMC tip geometry are shown in Fig. 3.9.

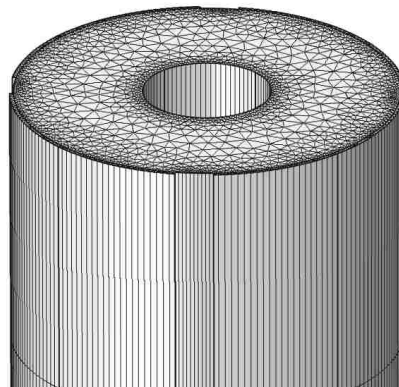


Figure 3.9: IPMC tip geometry and mesh used in finite element simulations of tube-shaped IPMCs

The simulation utilizes the Solid Mechanics, Transport of Diluted Species, Electric Currents, and General Form PDE COMSOL physics modules to achieve the desired governing equations. A linear elastic material model was implemented for the solid mechanics physics, where the material property values used are shown in Table 3.4. The transport of diluted species and general form PDE physics provide the PNP differential equations, which have been used to describe cation concentration and electric potential gradient during IPMC deformation. The model is split into two studies: (1) the deformation is calculated independently, and (2) the PNP differential equation model is applied to find ionic concentration and electric potential throughout the IPMC. In the case of sensor simulation, study (1) is computed first followed by study (2). Modeling is performed in the opposite order for actuator simulation.

Table 3.4: Material properties used for solid mechanics model for tube-shaped IPMCs.

Material property	Value
Young's modulus, E [ref. 24]	0.2 GPa
Poisson's ratio, ν [ref. 24]	0.49
Polymer density, ρ_p	874 kg/m ³

The model input is a prescribed tip displacement of a rigid connector on the IPMC tube's free-end with the opposite end held fixed, which is similar to the experimental setup. The solid mechanics physics describe stress, strain, and local displacement throughout the specimen for a prescribed tip displacement. The solid mechanics model is primarily coupled to the PNP model through the term, $\mu C V_c \nabla P$, from Eq. (3.1), where the solvent pressure is related to the polymer pressure by $\nabla P = -\nabla p$, where p is the polymer pressure found from the solid mechanics model as the average normal stress at each location. Additionally, the PNP model is coupled to the solid mechanics model through anion

migration, as indicated in Eq. (3.8). There are no empirical or experimentally determined coefficients apart from material properties for the given sensor model. The accuracy of the results will be discussed in a following section.

3.7.2 Sample Preparation and Experimental Setup

Nafion pellets are heated above glass transition temperature and are extruded in the cross-sectional shape shown in Fig. 3.10. The polymer is tensioned after extrusion to facilitate polymer chain realignment and to achieve the desired mechanical properties. After the polymer is cooled to room temperature, it is cut into 20-25 mm segments for testing.

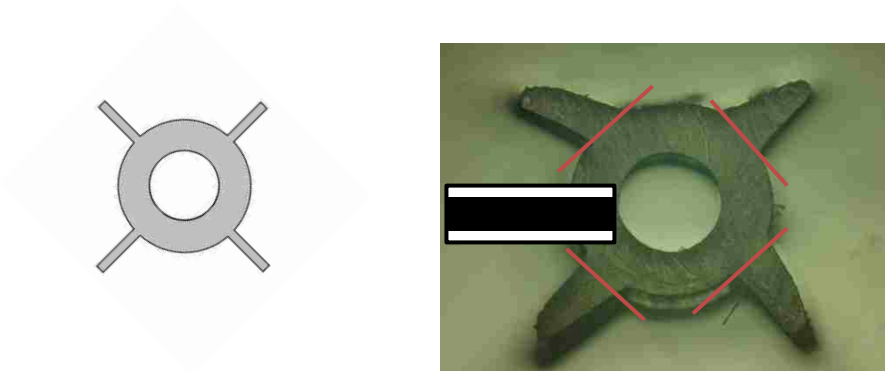


Figure 3.10: Schematic of cross-section of the extruded Nafion tubes (not to scale): illustration (*left*), and a photograph of experimental sample (*right*)

The extruded Nafion samples are activated by a hydrolysis reaction using a potassium hydroxide solution. After hydrolysis, the samples are cleaned and prepared for primary plating. The Nafion samples are plated using a Platinum impregnation-reduction reaction. Primary plating is repeated to increase the surface conductivity of the sample. When the surface conductivity reaches a desired amount, secondary plating is performed.

Secondary plating increases the surface conductivity of the samples by depositing Platinum on the surface of the sample via a chemical deposition. After secondary plating, the surface conductivity of the samples is at an acceptable level for good IPMC performance. An ion exchange can now be conducted to achieve better transport of water molecules through the membrane. Hydrogen ions within the membrane are exchanged for lithium ions which give a better transport of water molecules through the membrane. After the ion exchange process, the samples are cleaned and stored in DI water.

The flanges are removed with precision razor blades to make separated electrodes. Separating the electrodes allow for multiple degree-of-freedom sensing motion when a voltage is applied. A finished IPMC sensor is shown in Fig. 3.11.



Figure 3.11: Photograph of a tube-shaped IPMC sample

A collet is fabricated out of Nylon to clamp the IPMC tube at each electrode. The electrode contact patches of the collet are made out of copper foil. Individual wires are soldered to each contact patch and are glued to each of the collet fingers as seen in Fig. 3.12. The collet is hand tightened around each sample to securely fasten it. Previous clamping systems that have been used are restricted to a set diameter [39]. The current design allows for testing of variable diameter IPMCs [40].



Figure 3.12: Wire soldered to copper foil (*left*), and copper foil attached to nylon collet for one corner of the collet (*right*)

Once the IPMC is mounted inside the collet, the collet is secured to a collet mount and can be lowered into the water to the desired level using an adjustable plastic slide. The other end of the IPMC is clasped between two pieces of Plexiglas for the sensor setup. This end is attached to a shaker to create the motion required to produce voltage changes in the IPMC, as shown in Fig. 3.13. An illustration of the mechano-electrical IPMC experimental setup is shown in Fig. 3.14.

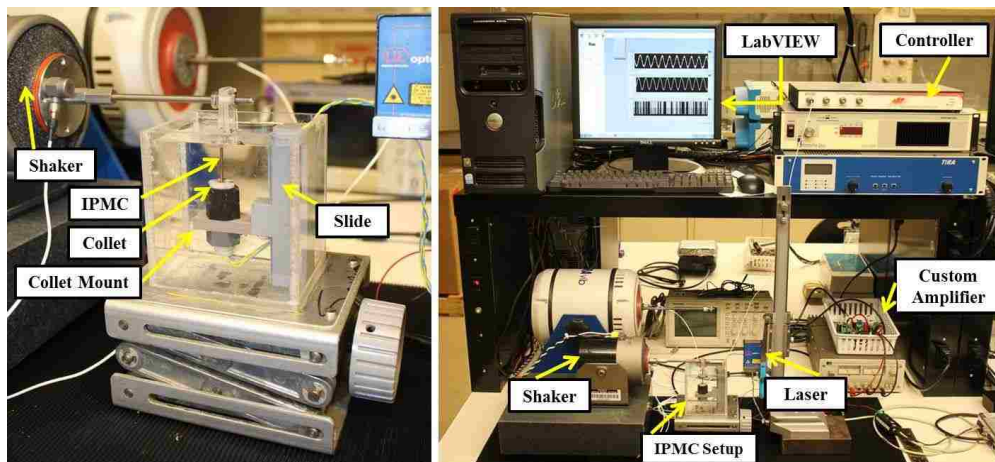


Figure 3.13: Mounting system for cylindrical IPMC sensors (*left*), and sensor experimental setup (*right*)

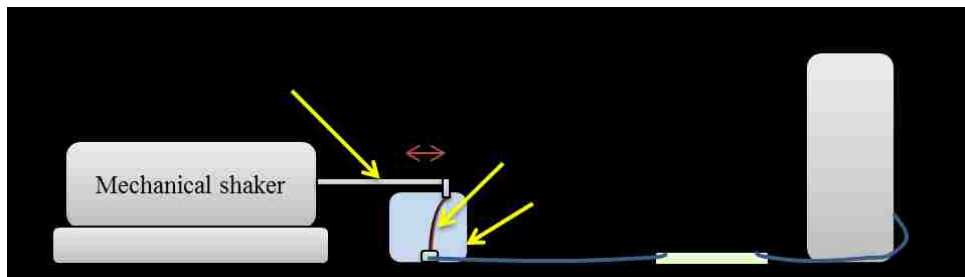


Figure 3.14: Illustration of the IPMC mechano-electrical experimental setup

The signal data was recorded using LabVIEW with National Instruments USB-6008. The displacement was measured with a laser displacement sensor (optoNCDT-1401, Micro-Epsilon) and was recorded in LabVIEW.

3.7.3 Experimental and Simulation Results

Tube-shaped IPMCs were fabricated and tested as sensor devices with sinusoidal tip displacement inputs of half peak-to-peak amplitudes 0.5 mm and 1.5 mm at a frequency of 1 Hz. The induced voltage amplitude increase with increasing tip displacement is quite significant and is similar to that seen when using rectangular shaped IPMCs. The induced voltage amplitude, although low, is on similar scale to that seen with much larger rectangular IPMC samples [41]. Direct comparison of the performance is difficult however, due to the different sample dimensions and experimental conditions. These results suggest tube shaped IPMCs are capable of multi degree of freedom displacement transduction; however, further research needs to be done to better understand the polymer-electrode interaction and improve the electrode plating process. Sample experimental traces can be seen in Fig. 3.15.

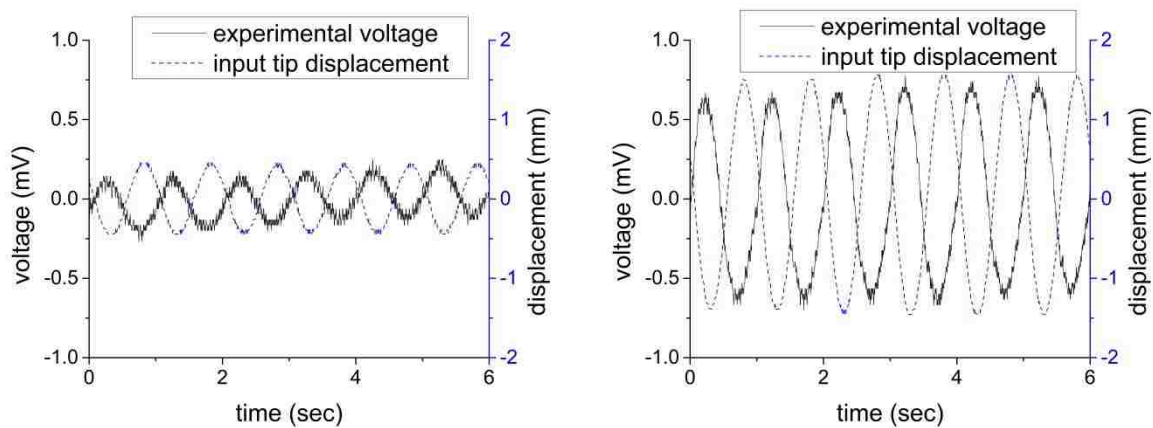


Figure 3.15: Experimental results of tube-shaped IPMC sensors for sinusoidal tip displacement input of 0.5 mm amplitude (*left*), and results for tip displacement input of 1.5 mm amplitude (*right*). Frequency at 1 Hz

Finite element simulations were performed of mechanoelectric transduction for a tube-shaped IPMC with 1 mm outer diameter, 1/3 mm inner diameter, and 20 mm length. The electrodes were set to be 0.01 mm thick. Simulations were performed using COMSOL following the steps outlined in section 3.7.1. Modeling parameters are provided in Table 3.5. Diffusion coefficient and molar volume change were adjusted to best fit the experimental results.

Table 3.5: Parameters used during tube-shaped IPMC simulations.

Material property	Value
Diffusion coefficient, D	$1e^{-11} \text{ m}^2/\text{s}$
Faraday's constant, F	96485 s·A/mol
Charge number, z	1
Molar volume change, V_c [ref. 21]	$1e^{-5} \text{ m}^3/\text{mol}$
Gas constant, R	8.31 J/mol·K
Absolute temperature, T	293 K
Effective dielectric permittivity, ϵ	0.1 F/m
Initial ionic concentration, C_0	1100 mol/m ³

Comparison of experimental and simulation results for sinusoidal tip displacement inputs of 0.5 mm and 1.5 mm amplitude at 1 Hz are shown in Fig. 3.16. These are seen to be in good agreement in terms of both phase and amplitude, indicating the given IPMC sensor model and selected parameters match the experimental results for the fabricated tube-shaped IPMCs for cases of simple input motion.

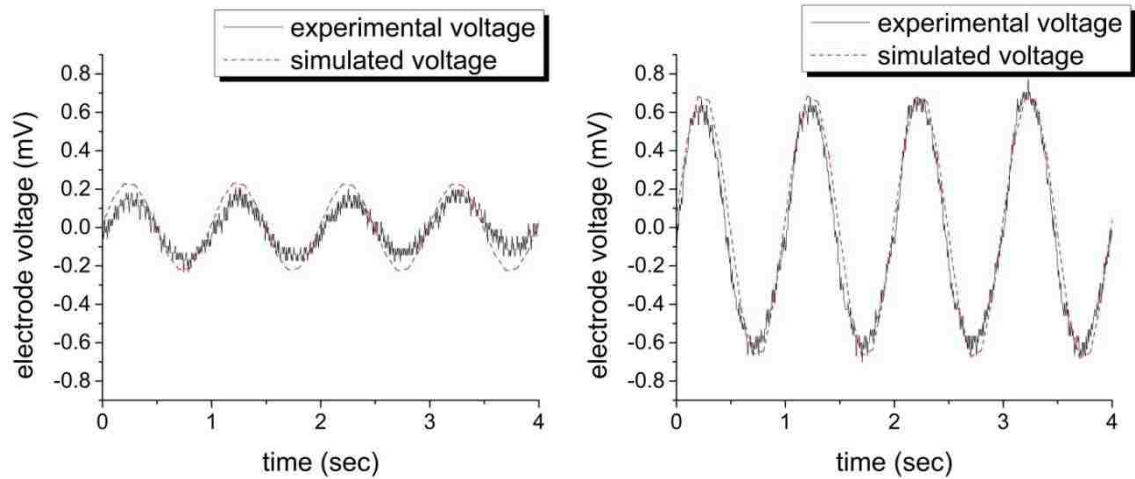


Figure 3.16: Simulation compared to experimental results of tube-shaped IPMC sensors for sinusoidal tip displacement input of 0.5 mm amplitude (*left*), and for tip displacement input of 1.5 mm amplitude (*right*). Frequency of 1 Hz

Cation and anion concentration variation, electric potential, and charge density within the polymer were simulated for sinusoidal tip displacement inputs. Results taken from a time at max displacement during sinusoidal input are presented as surface plots showing these distributions at the fixed end of the IPMC. A line path was also taken across this surface in the bending direction to better display cation and anion concentration changes. These are shown in Fig. 3.17 and 3.18.

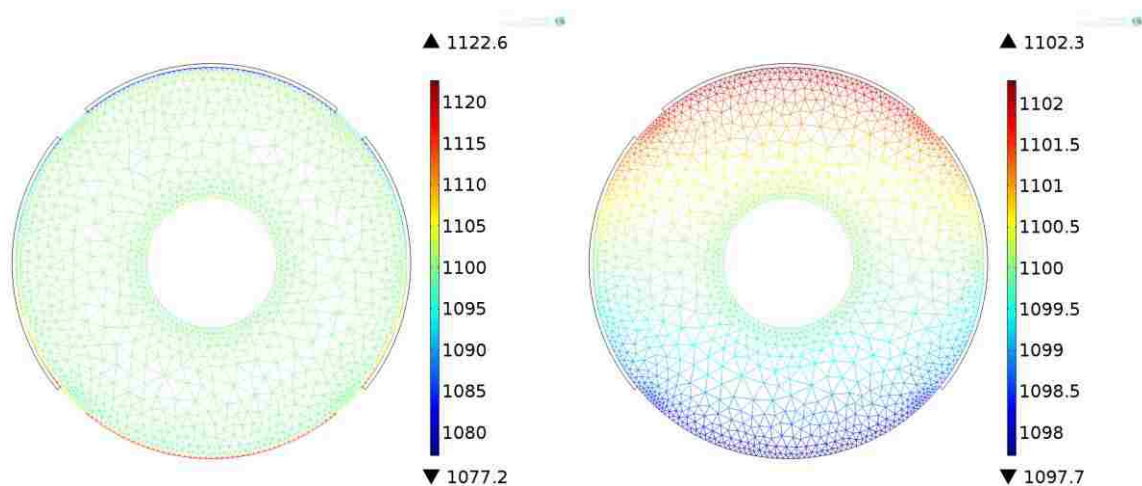


Figure 3.17: Cation concentration near fixed end at max bending input (*left*), and anion concentration near fixed end at max bending input (*right*). Input is tip displacement at 1.5 mm amplitude, 1 Hz

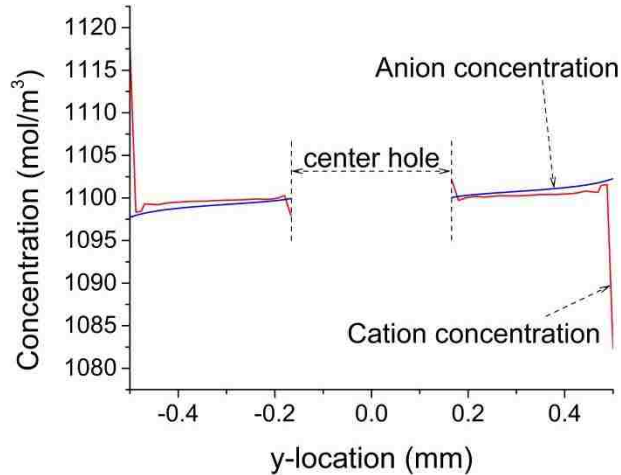


Figure 3.18: Ion concentrations across vertical center line of tube-shaped IPMC

As one would expect, the cation concentration rise in the subsurface layer near the IPMC boundary is small in comparison to actuator simulations, which show increase of concentration as large as 1000 mol/m³ in this same small subsurface area. This is likely due the high electrode charge driving the strong migration of cations in the case of actuation. Whereas for sensing, the induced electric potential is only due to rearrangement of ions from deformation, which results in small values for both concentration change and electric potentials as opposed to the case of actuation.

Cation and anion concentration variation, electric potential, and charge density within the polymer were simulated for electromechanical and mechano-electrical transduction of rectangular and tube-shaped IPMCs. The cation concentration rise in the narrow subsurface region near the polymer-electrode interface has been simulated for the different cases. Simulated values from the same location per IPMC for each case are displayed in Fig. 3.19.

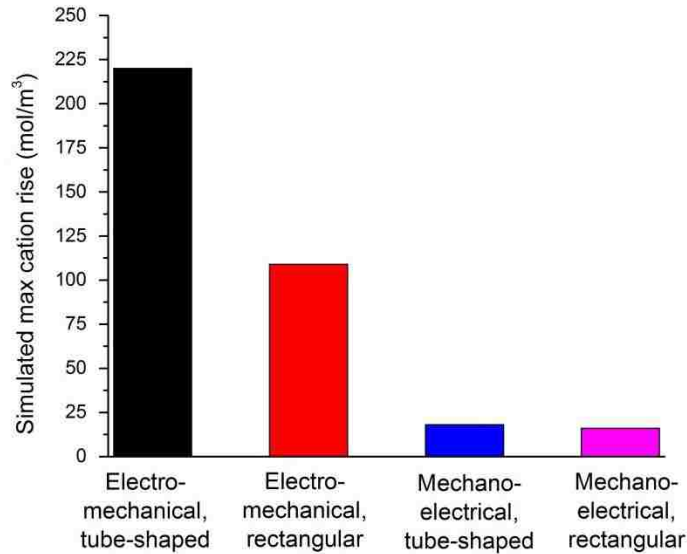


Figure 3.19. Simulated cation concentration rise near the polymer electrode interface at max displacement for the given IPMC transduction cases

The cation concentration rise in the subsurface layer near the IPMC boundary is small in mechano-electrical transduction simulations as compared to electromechanical simulations, which show increase of concentration on the order of 100 mol/m^3 in this same narrow subsurface region. This can be attributed to the high electrode charge driving the strong migration of cations in the case of electromechanical transduction. Whereas for mechano-electrical transduction, the induced electric potential is only due to rearrangement of ions during deformation, which results in small values for both concentration change and electric potentials.

Experimental results and simulations have been presented which provide a framework for further developing tube-shaped IPMC sensors and other 3D IPMC models. These results show that 3D transduction of the fabricated IPMC devices is feasible and the given model can provide accurate simulations for simple input motion. Because there are no empirical relationships utilized in coupling the solid mechanics physics to the PNP physics in the given model, this model can readily be applied to other 3D complex shaped IPMC sensor devices.

The signal in case of complex motion sensor simulation consists of both a position and ionic velocity component of the deforming IPMC. As an example, a flower pedal shape has been used as the prescribed displacement, as seen in Fig. 3.20. This type of tip displacement motion starts from the center (zero location) and passes through the center halfway through and at the end of each cycle. Simulations were carried out for two cycles. The resulting electrode signals are shown in Fig. 3.21. If the signal was comprised only of the IPMC deformation at any instant of time, one would expect at times $t=2$ and $t=4$ seconds the signals of the electrodes would all pass through 0 mV; however, this is not the case, and hence there is a significant velocity component to the IPMC sensor signal.

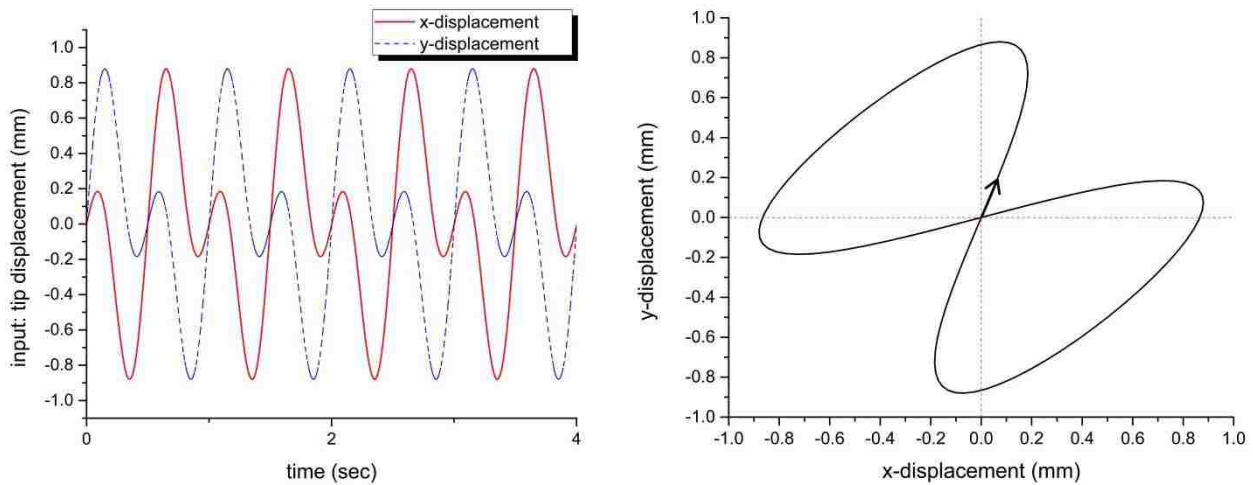


Figure 3.20: Input tip displacement for complex sensor signal simulation example (*left*), and x-y plane of the given tip displacement input (*right*). The arrow indicates direction of increasing time

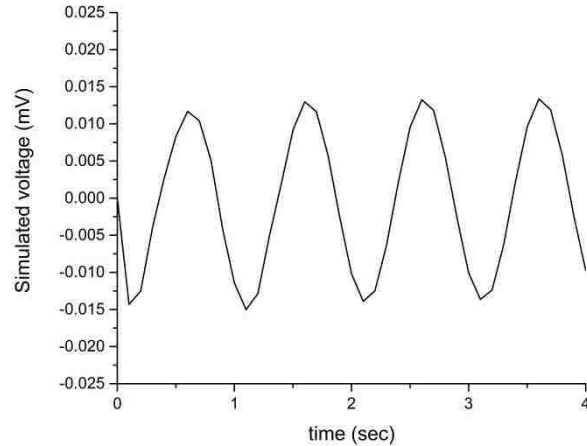


Figure 3.21: Simulated signal of the top electrode with the bottom electrode grounded for the input tip motion shown in Fig. 3.20 over two cycles

Mathematical modelling, fabrication and experimental performance studies of tube-shaped IPMC sensors have been presented. The results suggest IPMC transducers of this design are functional and simulations using the provided model are in good agreement with experimental results for simple harmonic input motion. Further work needs to be done to decouple the position and velocity components of the sensor signal. Further work also includes revising the solid mechanics model to include nonlinear material effects and electrode deformation. Improvements to IPMC fabrication, electrode plating and patterning are also being sought. Finally, design of sized-down tube shaped IPMCs are being studied to develop smaller actuator and sensor IPMC devices.

CHAPTER 4. ELECTRODE EFFECTS OF IPMCS

In this chapter, a research paper published in *Journal of Applied Physics* is included. The authors, in order of appearance on the article, are Qi Shen, Viljar Palmre, Tyler Stalbaum, and Kwang J. Kim. This article provides a complete coupled model encompassing change in electrode material properties during deformation and the associated influence on actuation performance. Reprinted from *Journal of Applied Physics*, Shen, Q., Palmre, V., Stalbaum, T., and Kim, K. J., "A comprehensive physics-based model encompassing variable surface resistance and underlying physics of ionic polymer-metal composite actuators," *118*(12), 124904, (2015), with the permission of AIP Publishing. The reader is referred to this article for a more in-depth description of the variable electrode properties mathematical model.

The primary contributions to the mathematical modeling of the electrodes are from QS. The primary contributions to physics based modeling and model coupling are from QS and TS. The experimental work was done by VP and QS. The data analysis, simulations, conclusions, and discussion were a combined effort from the whole research team.

4.1 Physics-Based Modeling Encompassing Variable Electrode Surface Resistance

The ionic polymer-metal composite (IPMC) is an emerging smart material in actuation and sensing applications, such as artificial muscles, underwater actuators, and advanced medical devices. However, the effect of the surface electrode properties change on the actuating of IPMC have not been well studied. To address this problem, attempts can be made to theoretically predict and experimentally investigate the dynamic electro-mechanical response of the IPMC thin-strip actuator. A model of the IPMC actuator is proposed based on the Poisson-Nernst-Planck equations for ion transport and charge dynamics in the polymer membrane, while a physical model for the change of surface resistance of the electrodes of the IPMC due to deformation is also incorporated. By incorporating these two models, a

complete, dynamic, physics-based model for IPMC actuators is presented. To verify the model, IPMC samples were prepared and experiments were conducted. The results show that the theoretical model can accurately predict the actuating performance of IPMC actuators over a range of dynamic conditions. Additionally, the charge dynamics inside the polymer during the oscillation of the IPMC are presented. It is also shown that the charge at the boundary mainly affects the induced stress of the IPMC. The current study is beneficial for the comprehensive understanding of the surface electrode effect on the performance of IPMC actuators.

Scanning electron microscopy (SEM) was used to study the structure of the IPMC sample. Figure 4.1 shows the cross-sectional image of the IPMC, which indicates the platinum content distribution in the electrode and vicinity. Based on the image, the IPMC was composed of the electrode and the polymer membrane. In the surface resistance model above, the electrodes are considered a bulk metal. However, in reality from the SEM images it can be seen that the structure is more complicated. The thickness of the electrode could vary significantly. The thin electrolessly plated electrodes on a polymer do not result in a uniform conductivity in each direction at each location, so the defective factor helps to take those effects into account. The parameters of the electrode were measured based on the SEM images.

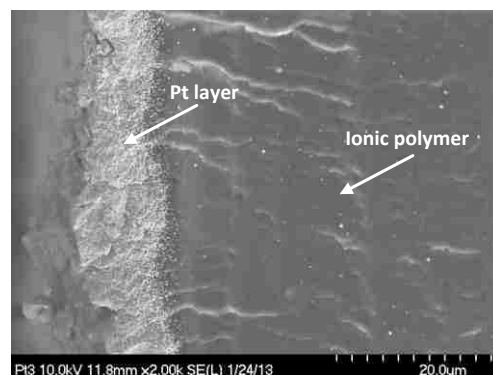


Figure 4.1: Cross-section SEM images of the IPMC. Reprinted from *Journal of Applied Physics*, Shen, Q., Palmre, V., Stalbaum, T., and Kim, K. J., "A comprehensive physics-based model encompassing variable surface resistance and underlying physics of ionic polymer-metal composite actuators," *118*(12), 124904, (2015), with the permission of AIP Publishing

The governing physics in the polymer membrane are similar to those provided in Chapter 3. The modified Nernst-Planck equation with actuation assumption simplifications as described in Chapter 3, which describes the cation migration and diffusion in the polymer element backbone, and the Poisson's equation, which describes the concentrating of local charges at the boundary between the polymer and surface electrodes resulting in an electric field increase in the opposite direction, are expressed as [14, 37]

$$\frac{\partial C}{\partial t} + \nabla \cdot (-D\nabla C - z\mu FC\nabla\phi) = 0 \quad (4.1)$$

$$\nabla \cdot \vec{E} = -\nabla^2\phi = \frac{\rho}{\hat{\epsilon}} \quad (4.2)$$

$$\rho = F(C - C_0) \quad (4.3)$$

A model was developed for resistance change based on strain of an IPMC [37]. This model has been incorporated into the modeling framework and results are presented within this chapter. For the comparison of the strain, the widths of the samples were the same. Some parameters of the actuation model were based on previous results of the surface resistance. Some are physical constants. Table 4.1 shows the value of the IPMC actuator model constants [20]. The absolute temperature is $T = 297$ K. The rest need to be identified. In current study, the voltage amplitude applied on the IPMC was constant. By applying varies frequencies to the IPMC, varies deformation as well as strains can be obtained. The deformations of the IPMC actuators were measured. Based on the experimental results of IPMC 1 through the least-square method in MATLAB, the parameters of the model were identified as $Y = 90.92 \times 10^6$ Pa and $\alpha = 104$ J/C. The Young's module of IPMC varies from 41×10^6 Pa to 571×10^6 Pa based

on previous work [20, 42]. The coupling constant α varies from 30 J/C to 148 J/C based on previous work [14]. Thus the value in current paper is reasonable. The parameters were plugged into the actuation model (except geometric dimensions) for predicting the actuating performance of IPMC 2 and IPMC 3. Model with and without surface resistance change were compared. For the model without consideration of the surface resistance change, the surface resistance R is a constant value and was identified as $R = 1.8 \Omega$ through the non-linear fitting process. The surface resistance per {unit length · unit width} of the IPMC is 7.44Ω . Previous work reported the surface resistance per {unit length · unit width} as 22.3Ω [42]. The reasons for the difference are the different electrode plating times and different reduction temperatures during the fabrication process of IPMC. The rest of the parameters are the same as previous simulations.

In the current study, the deformation of the IPMC is converted to the strain for intuitive comparison. Figure 4.2 shows the resistance change of the IPMC electrode versus different strains. The simulation results were compared with the experimental results. It can be seen that the model can well describe the resistance change of the IPMC electrode. It is also noticed that with the strain increasing, the resistance change of the electrode increased.

The actuation model was verified in experiments by applying sinusoidal actuation signals to the IPMC samples and measuring the deformations. Figure 4.3 shows the comparison of experimental results with theoretical model simulation results with and without consideration of surface resistance change. It is clear that the model considering the effect of surface resistance change shows better agreement than the one ignoring the resistance. This indicates that the model incorporating the surface resistance change is more effective in capturing the actuation dynamics of IPMC. Based on Fig. 4.3, it can be found that for all samples, good agreement between the model prediction and the experimental data is achieved. These figures show that current actuation model can well predict the actuating of

IPMCs. It is also noticed that with the voltage amplitude increasing, the strain of the IPMC increased. As the actuating frequency rose, the strain of the IPMC reduced.

Table 4.1: Value of IPMC actuator model constants for electrode effects modeling.

Item	Value
D	$7 \times 10^{-10} \text{ m}^2/\text{s}$
C_0	$1091 \text{ mol}/\text{m}^3$
ε	$0.2 \times 10^{-3} \text{ F}/\text{m}$
μ	$2.9 \times 10^{-15} \text{ mol}\cdot\text{s}/\text{kg}$
z	1
F	96487 C/mol
R	8.3143 J/mol·K

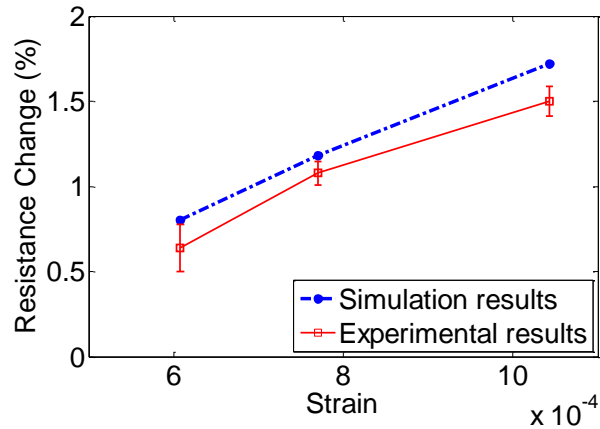


Figure 4.2: Comparison between the simulation results and experimental results of the electrode resistance change. Reprinted from *Journal of Applied Physics*, Shen, Q., Palmre, V., Stalbaum, T., and Kim, K. J., "A comprehensive physics-based model encompassing variable surface resistance and underlying physics of ionic polymer-metal composite actuators," *118*(12), 124904, (2015), with the permission of AIP Publishing

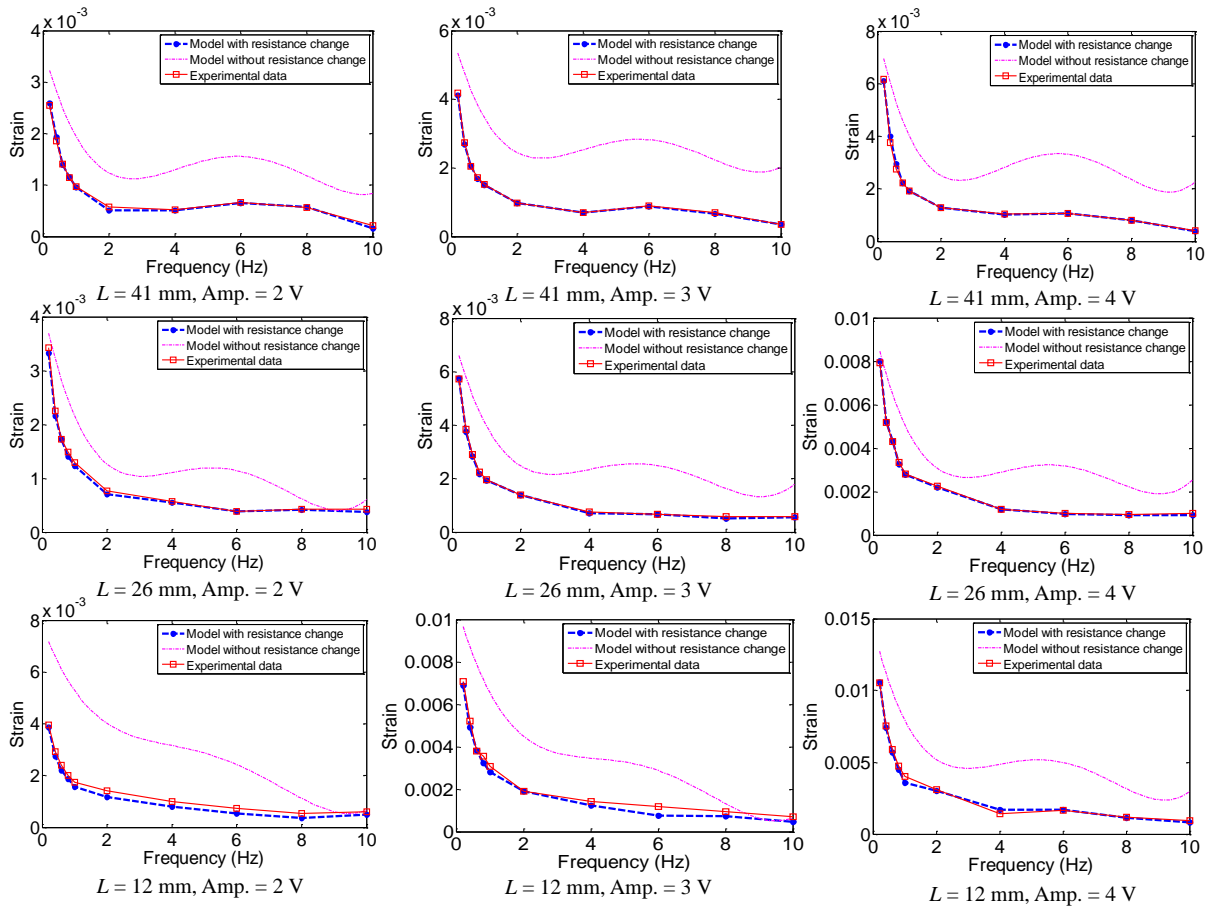
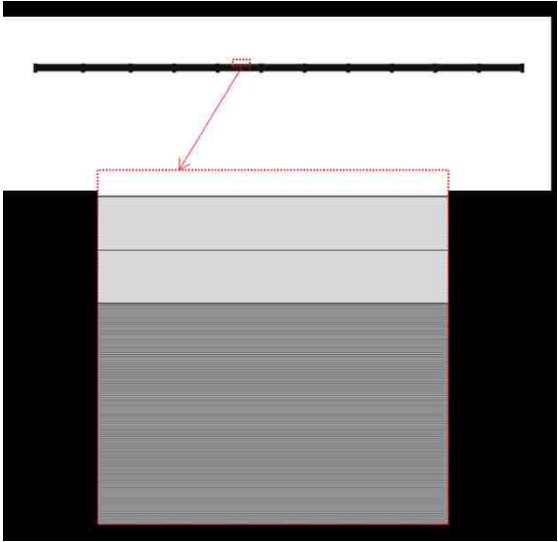


Figure 4.3: Comparison of experimental results of IPMC strain with model predictions, with and without consideration of surface resistance change. Reprinted from *Journal of Applied Physics*, Shen, Q., Palmre, V., Stalbaum, T., and Kim, K. J., “A comprehensive physics-based model encompassing variable surface resistance and underlying physics of ionic polymer-metal composite actuators,” *118*(12), 124904, (2015), with the permission of AIP Publishing (Figure courtesy of Q. Shen)

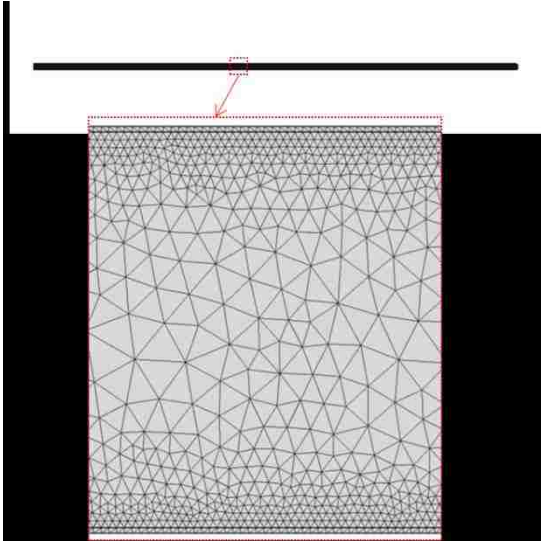
4.2 Modeling and Discussion

A physics-based model was used to simulate ion concentration, polymer electric potential, charge density and displacement response to a low voltage input signal to obtain further insight into the underlying physics. A 2-dimensional finite element simulation was performed using COMSOL Multiphysics 4.3b software. Two mesh types were used in simulation: (1) a sparsely mapped mesh along the length with a very large element aspect ratio; (2) a triangular mesh with fine distribution near electrodes and maximum aspect ratio of 1.3:1, as shown in Fig. 4.4. The sparsely mapped mesh was

utilized because the changes in the length direction were assumed to be negligible. The sparsely mapped mesh has 55,044 elements, whereas the triangulated mesh has 145,952 elements. Both meshes were refined to within 1% solution change. Additionally, the sparse mesh produced the same solutions as the triangulated mesh and was thus chosen for use in simulations.



(a)



(b)

Figure 4.4: Meshes used in finite element simulations: (a) mesh sparsely mapped along length; (b) triangulated mesh

The simulation utilizes the transport of diluted species, general form partial differential equation (PDE), electric currents, and solid mechanics physics modules in COMSOL to achieve the desired governing set of PDEs. The transport of diluted species and general form PDE physics provide the Poisson-Nernst-Planck (PNP) set of coupled PDEs, which are used to describe cation concentration and electric potential within the polymer. A linear elastic material model with infinitesimal strain theory was implemented for the solid mechanics physics. The simulation is divided into two studies: first the electric currents and PNP physics are applied simultaneously to find ion concentration and charge density in the IPMC for a given sinusoidal voltage input, and then the solid mechanics study is performed. The voltage is applied over a fixed region of 10 mm in length to the electrodes, similar to the experimental setup. The solids model is done with one end of the IPMC fixed. A body load which is assumed proportional to the charge density is applied across the free length of the IPMC strip.

During electromechanical actuation of an IPMC by supplied voltage input to its electrodes, the main contribution to the deformation is assumed to be the cation migration and corresponding swelling effects. In current model, the IPMC is in fully hydrated condition. The contribution from the concentration gradient and electric potential are much larger than the contribution of the pressure gradient, thus this term has been omitted and the Nernst-Planck equation is expressed in Eq. (4.1). Poisson's equation as used in the model is expressed in Eq. (4.2). The anions of the IPMC are fixed to the polymer backbone making the anion concentration variable with deformation only, while the cations are free to migrate based on the electric potential. Thus in actuation of the IPMC by input voltage, the change of anion concentration is very small in comparison with the change in cation concentration and the charge density is assumed to be a function of cation concentration only as expressed in Eq. (4.3). A body force in the bending direction, which is assumed to be proportional to the charge density as $F_y = \alpha\rho$, is the input into the solid mechanics model. The solids mechanics describe the stress, strain, and local displacement. The governing solid mechanics equation used is:

$$\rho_m \frac{\partial^2 \mathbf{u}}{\partial t^2} - \nabla \cdot \boldsymbol{\sigma}_m = F \quad (4.4)$$

where ρ_m is material density and $\rho_m = 874 \text{ kg/m}^3$, $\mathbf{u} = \{u, v\}$ is the local displacement vector in x and y directions respectively, and F is the body force vector. Notation $\boldsymbol{\sigma}_m$ is the material stress tensor written in terms of local displacement using Hooke's Law as

$$\begin{bmatrix} \sigma_{xx} \\ \sigma_{yy} \\ \sigma_{xy} \end{bmatrix} = \frac{E}{(1+\nu)(1-2\nu)} \begin{bmatrix} (1-\nu) & \nu & 0 \\ \nu & (1-\nu) & 0 \\ 0 & 0 & (1-2\nu) \end{bmatrix} \begin{bmatrix} \frac{\partial u}{\partial x} \\ \frac{\partial v}{\partial y} \\ \frac{1}{2} \left(\frac{\partial u}{\partial y} + \frac{\partial v}{\partial x} \right) \end{bmatrix} \quad (4.5)$$

where ν is the Poisson's ratio and $\nu = 0.49$. As the material is assumed to deform primarily in the bending plane, a plane strain deformation assumption was utilized, hence strains in the x - z , y - z , and z - z planes are assumed to be zero. The model first utilizes Eqs. (4.1), (4.2), and (4.3) to solve for the charge density, ρ . Then, Eqs. (4.4) and (4.5) are solved for the deformation. The constant parameters used for COMSOL simulations are shown in Table 4.3.

Since an experimental method of measuring the cation migration and charge density within the polymer is not readily available, the COSMOL simulation results were used primarily to gain insight into these phenomena. The simulation of the IPMC actuating was performed under an input voltage with amplitude of 2 V and frequency of 1 Hz. Figure 4.5 illustrates the IPMC oscillation time-series during steady-state response. Within one oscillation cycle, the stress on the IPMC strip varied along the length.

The stress on the IPMC increased as the IPMC curved. At the maximum tip displacement, the stress reached its maximum. Figure 4.6 shows the simulation result of the IPMC tip displacement. As can be seen in the graph, after several cycles of oscillation, the quasi-steady state of the IPMC tip movement appeared to be reached. The amplitude of the oscillation is 2.1×10^{-3} m. The tip displacement result also shows a good agreement with the experimental result.

Figure 4.7 show the cation concentration in the polymer near the top and bottom electrode separately. The location (x, y, z) of the measured points are $(h - 1 \times 10^6 \text{ m}, W/2, L/2)$ and $(-h + 1 \times 10^6 \text{ m}, W/2, L/2)$. A sinusoid variation of the cation concentration was observed during the deformation of the IPMC actuator within a range between $1.44 \times 10^3 \text{ mol/m}^3$ and $0.82 \times 10^3 \text{ mol/m}^3$ for both points. As shown in Fig. 4.7, the cation concentration reached its quasi-steady state after several cycles of oscillation. It was also noticed that the cation concentration near the top and bottom electrode show an opposite variation, as was expected. The initial transient phase of actuation response can be verified experimentally. This can be thought of as the result of the initial cation distribution at the beginning of the first oscillation cycle (at $t = 0$ seconds) being different than at the beginning of following cycles, until the cation distribution at the start of each cycle is nearly constant.

Figure 4.8 shows the cation concentration time series along the thickness direction in accordance with Fig. 4.5. The location of the measured line was $y = W/2$ and $z = L/2$. It can be found that in one cycle, the cation concentration near the upper and bottom electrode changed significantly, and remained the same in the central area. The simulation results indicated that the charge density at the boundary has a main effect on the stress of the IPMC. However, the relationship between the charge density and induced stress cannot be verified based on current simulation and experimental results.

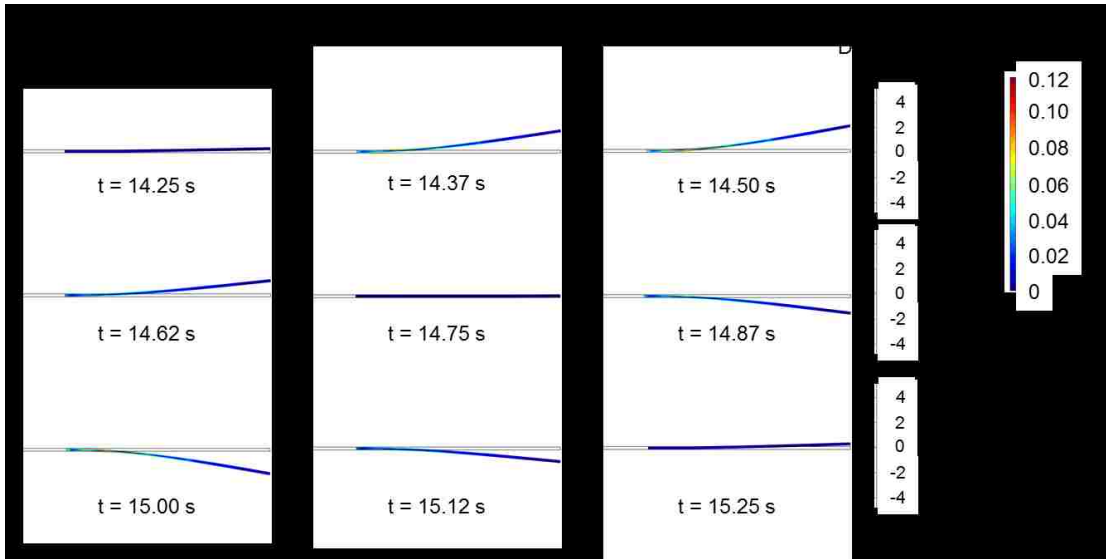


Figure 4.5: IPMC strip displacement for one cycle during steady-state response for a sinusoidal voltage input of 4 V peak-to-peak amplitude and 1 Hz frequency using the variable electrode properties model

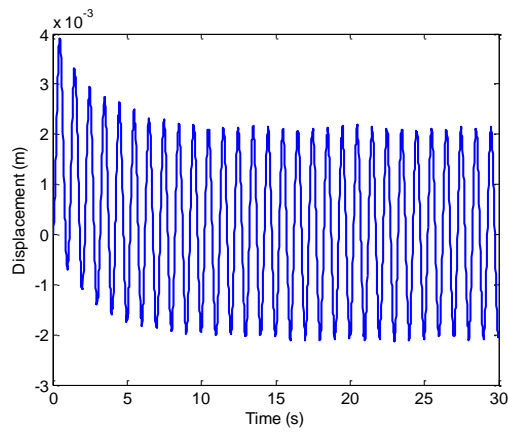
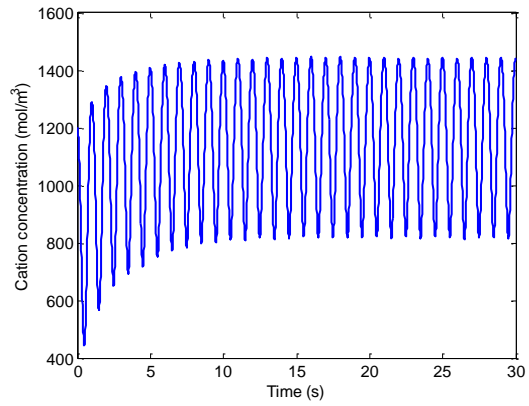
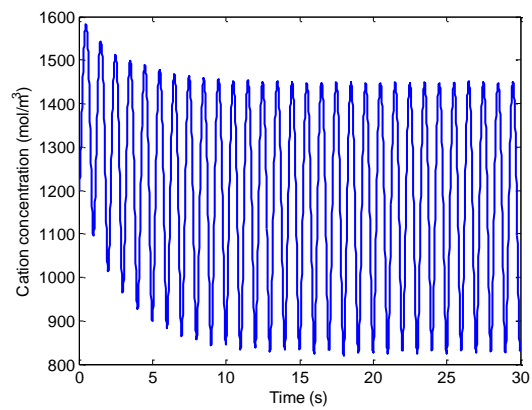


Figure 4.6: Simulation result of the IPMC tip displacement using the variable electrode properties model



(a)



(b)

Figure 4.7: Simulation result of the IPMC cation concentration using the variable electrode properties model: near top electrode (a), and near bottom electrode (b)

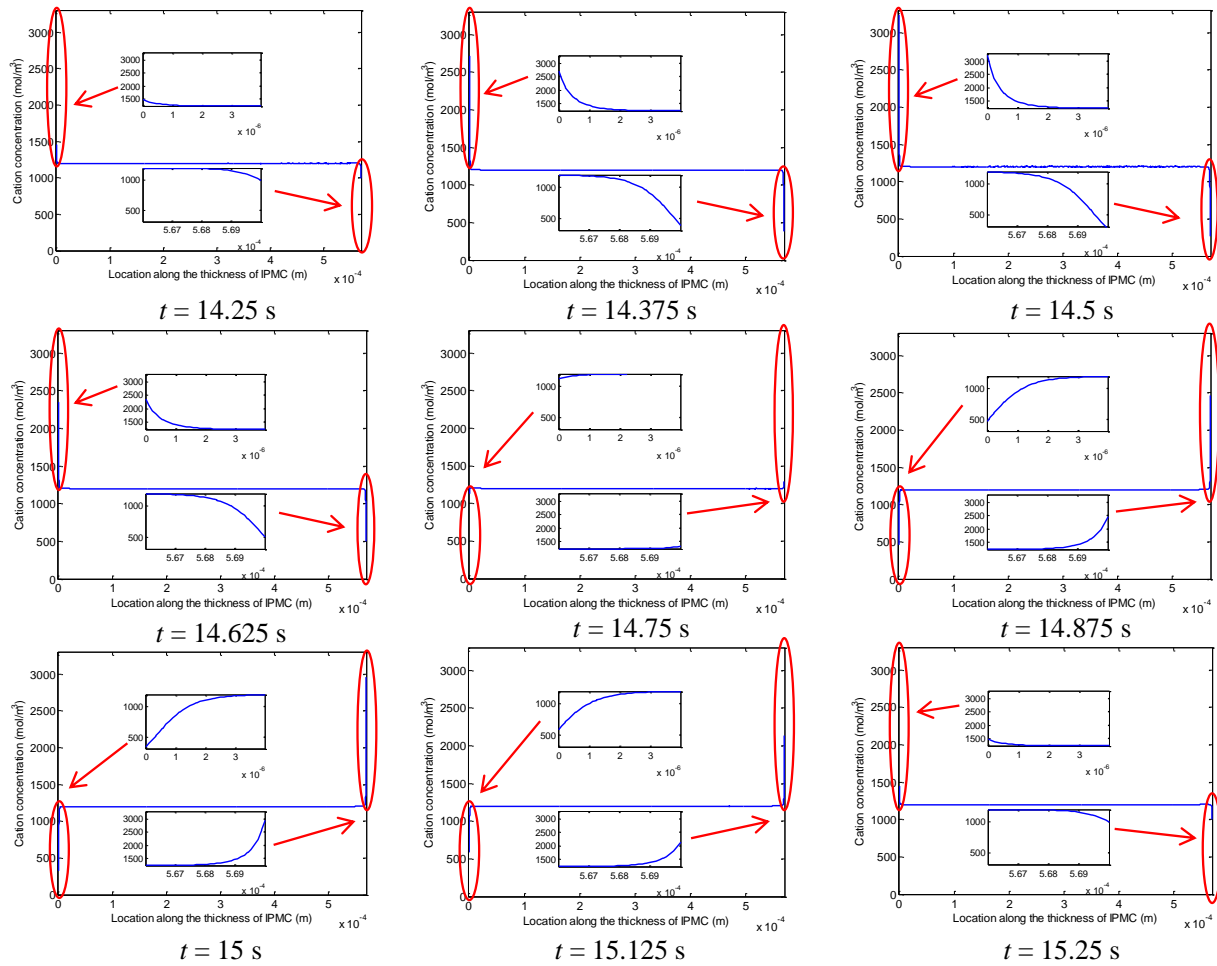


Figure 4.8: Simulation results of cation concentration along the thickness of IPMC using the variable electrode properties model

In this chapter, a physical based model of IPMC was developed. The model is based on the charge dynamics model of the polymer membrane and a microstructure model of the electrode. Experiments were conducted to verify the model. Theoretical results and experimental results were compared and showed a good agreement. The results show that the model that considers the surface resistance change is more accurate in predicting the actuating response of IPMC than the model without considering the surface resistance change. Finite element approach was implemented to study the charge dynamics inside the polymer. It was found that the charge at the boundary of the IPMC has a major effect on the performance of IPMC actuators.

In the future, focus will be on the application of the theoretical model approach to the control of biomimetic robots and manipulations such as medical devices. Meanwhile, the IPMCs in the current study are based on the electroless processing method. New electrode plating method will be used to fabricate the new IPMCs, such as electroplating method, hot pressing method. The theoretical model will be verified with the new IPMCs. New IPMCs will also be fabricated with different Pt loading in the electrode layers and other metals as electrode, and new models will be developed for the new IPMCs by the same method.

CHAPTER 5. ELECTRODELESS EAP ACTUATORS

In this chapter, a research paper accepted for publication in Marine Technology Society (MTS) Journal is included. This section provides an overview of the mechanisms of actuation of Nafion fibers in electrolyte. The overall physics are still governed by the Nernst-Planck and Poisson's equations, as in Chapter 3. However, in case of electrodeless electroactive polymer (EAP) actuators, the physics involve charge dynamics in the electrolyte as opposed to electric currents in the electrodes. Experimental and simulation results are compared in good agreement for the case of an individual electrodeless electroactive polymer. The authors, in order of appearance on the article, are Kwang J. Kim, Viljar Palmre, Tyler Stalbaum, Taeseon Hwang, Qi Shen, and Sarah Trabia.

Overall project was led by KJK. Primary contributions to fabrication and development are VP and TH. The primary contributions to the physics based modeling was TS. The experimental work was mostly done by VP and TH. The data analysis, simulations, conclusions, and discussion were a combined effort from the whole research team.

5.1 Promising Developments in Marine Applications with Artificial Muscles: Electrodeless Artificial-Cilia Microfibers

Ionic polymer-metal composite (IPMC) artificial muscles have received great research attention in the development of robotic manipulators, advanced medical devices, and underwater propulsors, such as artificial fish fins. This is due to their unique properties of large deformation, fast dynamic response, low power requirements, and the ability to operate in aquatic environments. Recently, locomotion of biological cells and microorganisms through unique motion of cilium (flagellum) has received great interest in the field of biomimetic robotics. It is envisioned that artificial cilia can be an effective strategy for maneuvering and sensing in small-scale bio-inspired robotic systems. However, current

actuators used for driving the robots are typically rigid, bulky in mechanism and electronics requirements producing some acoustic signatures, and difficult to miniaturize. Herein, the authors report biomimetic, wirelessly driven, electroactive polymer (EAP) microfibers that actuate in an aqueous medium when subjected to an external electric field of < 5 V/mm, which can be realized to create cilia-based robotic systems for aquatic applications. Initial development and manufacturing of these systems is presented in this paper. The EAP fibers are fabricated from ionic polymer precursor resin through melt-drawing process and have a circular cross-section with a diameter of 30–70 μm . When properly activated and subjected to an electric field with switching polarity, the EAP fibers exhibit cyclic actuation with adequate response time (0.05–5 Hz). The experimental results are presented and discussed to demonstrate the performance and feasibility of biomimetic cilia-based micro-actuators. Prospective bio-inspired applications of the artificial muscle cilia-based system in marine operations are also discussed.

Many aquatic lifeforms are equipped with natural tools for high-maneuverability, environmental sensing, and capturing or escaping from target or prey, respectively. These characteristics improve survival and well-being in often harsh or predatory-rich environments. The employed mechanisms are commonly unique to a select few natural creatures, which attributes to the survival of very different species in the same environments. Researchers have long aspired to mimic these natural traits by designing robotic mechanisms and advanced materials to create new technologies in marine operations [25, 43-48]. Examples of these developments include robotic devices such as artificial muscles, fish-fin-like underwater propulsors, full bioinspired underwater vehicle designs, and even intricately structured, soft, artificial-skin substrates [7, 43, 49-65].

One such natural system that has been investigated for prospective biomimetic marine applications is cilia and flagella of mammalian cells for micro-flow control and micro-locomotion mechanisms [50, 66, 67]. Cilia and flagella are micro-tubular protrusions from the surface of many eukaryotic cells and are of

two main types: motile, those capable of moving independently, and non-motile cilia [68, 69]. They are found in cells in nature and play a critical role in health and well-being, often functioning as mechanisms to move cells or objects through a flow channel, such as in the case of human windpipe, brain ventricles, and Fallopian tubes, as examples [70], in case of motile cilia. Non-motile cilia, found in many cells in nature, typically operate as a sensory system. However, motile cilia and non-motile cilia are structurally similar and both can function as signaling devices [68, 69]. As sensory organelles, these transfer information of extracellular signals to control several cellular processes [68]. Thus, sensory information from cilia is thought to be coupled to motile cilia for feedback environmental sensing and control [68, 69]. These characteristics have made cilia organelles a promising candidate for bioinspired device development in microfluidics and marine operations. The prospective applications of a simple, surface-mountable micro-artificial-cilia environmental sensory and control system range from near-surface flow control of underwater vehicles to advanced medical operations in drug delivery systems.

This paper exploits the unique properties of an in-lab designed artificial muscle (AM) micro-transducer to develop a working cilia-based micro-actuator array for marine applications. An AM is a multifunctional, smart polymer whose electromechanical properties can be controlled, resulting in reproducible actuation and sensing capabilities [71-73]. Like biological muscles, the AM technology exhibits large motion, good force, fast response, good efficiency, long cycle life, and silent operation. Recent research on the locomotion of biological cells and microorganisms has identified the importance of cilium (flagellum) and its unique motion for propulsion and maneuvering [68, 69]. However, recent man-made attempts at mimicking the motion of cilium using traditional actuators have yielded limited success and often the designs are bulky [92, 66, 67]. On the contrary, the AM technology is an excellent candidate for realizing the complex oscillatory motion of cilium for the development of efficient and highly maneuverable underwater actuator and sensor systems for marine applications.

The current state-of-the-art AM technology is limited to creating thin strips or cantilever-style actuators due primarily to difficulties associated with material processing. Recent advances in AM materials processing work and research have resulted in AMs which can produce forces on the order of tens of gram-force for a standard sample of 1-cm wide by 5-cm long by 1-mm thick. However, the manufacturing of slender rod-like AMs with sectored electrodes has been challenging [74]. Additionally, these devices require two or more separated electrodes per sample to actuate. Herein, the authors report a new electrodeless electroactive polymer (EAP) micro-actuator that actuates wirelessly by low external electric field and is capable of AM maneuverability. It is an ionic type EAP actuator with no built-in surface electrode layers. The new electrodeless EAP actuator consists of only one single perfluorinated EAP material. Due to its simple structure, the electrodeless EAP actuators are simple to fabricate into variety of shapes and can be easily miniaturized to micro-scale, which is needed for the development of small bio-inspired robotic systems such as artificial cilia or flagella. Preliminary studies have successfully demonstrated fabrication of AM with different geometries, including rod-shaped AMs which can undergo bending actuation and sensing in multiple directions, and micro-actuator fibers that have been expanded into prototype AM cilia arrays (1x20).

5.1.1 Artificial Muscle Fibers

Ionic polymer-metal composite (IPMC) transducers, made from an ionomer-based EAP, which have been used successfully as 3D micro-sensors in previous works [32, 75], are a strong motivation for this study for development into the cilia-like artificial muscle micro-actuator array due to their unique and well-suited properties. These devices exhibit fast dynamic response, high spatial resolution, low electronics and mechanisms requirements, and are best suited for operation in aqueous environments [22, 37]. Additionally, they are silent in operation, are low in power consumption, and can be designed to operate in different fluid environments [76]. Furthermore, they can operate as actuators or sensors

[12, 77], and have been designed into self-sensing actuators [78-80]. These characteristics make this type of AM a good material candidate for this research with a strong existing technical groundwork. However, IPMC electrode plating is a cumbersome process, and these devices require separated electrodes per sample to actuate.

Conventionally, IPMC material consists of an ionic polymer membrane, typically Nafion material, chemically plated on both surfaces with conductive metal layers, typically of Pt or Au, that serve as conductive electrodes. To enable an electroactive capability, the ionomer membrane is solvated with an electrolyte, typically Li^+ or Na^+ ions in water solution. When a DC voltage ($< 5 \text{ V}$) is applied to the electrodes, the hydrated cations migrate toward the negatively charged electrode, leading to internal pressure change, which in turn, causes a bending of the IPMC toward the positive electrode. The electromechanical performance of an IPMC is highly dependent on the electrical conductivity, flexibility and surface morphology of the electrodes [36, 37, 81]. The electrode structure determines the adsorption of electrolyte ions at the electrode interface (accumulated charge) that is directly proportional to the electromechanical deformation of the material. As such, the electrodes have many critical design requirements that pose several engineering challenges in terms of performance, manufacturing and scalability. Also, due to the presence of electric potential and liquid electrolytes, the choice of suitable electrode materials is restricted to electrochemically stable (inert) materials. Therefore, noble metals (such as Pt or Au), carbon nanotubes, carbide-derived carbons, and other carbon derivatives are used for electrodes.

Herein, the authors report a new artificial muscle for biomimetic applications, an electrodeless EAP micro-actuator that actuates wirelessly by low external electric field ($< 5 \text{ V/mm}$). It is an ionic type EAP actuator similar to the IPMC but with no built-in surface electrode layers. Hence, it is simply called an EAP actuator. As opposed to traditional tri-layer IPMC actuators with surface electrodes that comprise different materials and require complex manufacturing processes, the new electrodeless EAP actuator

consists of only one single perfluorinated electroactive polymer material. Due to its simple structure, the electrodeless EAP actuators are simple to fabricate into variety of shapes and can be easily miniaturized to micro-scale, which is needed for the development of small bio-inspired robotic systems such as artificial cilia (or flagellum). It is envisaged that artificial cilia can be an effective strategy for locomotion and maneuvering of next-generation miniature underwater robotic and microfluidic systems [82, 83]. However, the existing smart actuator technologies face challenges in downscaling to micro-scale due to their complex structure and manufacturing process and electrical conductivity issues related to miniaturizing the surface electrodes. For instance, down-scaling a tri-layered polymeric composite actuator requires much thinner and more flexible electrodes than in case of metallic Pt or Au electrodes and can become problematic due to loss in mechanical robustness, which is required to maintain electrical conductivity and durability.

To demonstrate the feasibility of the new electrodeless EAP fiber micro-actuators for small-scale bio-inspired robotic applications, an artificial muscle (AM) cilia fiber array system is developed. The electrodeless fiber EAP micro-actuators are fabricated from a perfluorinated precursor resin of Nafion through melt-drawing process. By careful control of the drawing conditions, cylindrical fibers with a diameter size down to 30 microns are successfully produced. These microfibers, when converted to electroactive form by a simple chemical treatment and subjected to an aqueous medium, display controllable electromechanical actuation in response to low external electric field (<5 V/mm). The prototype cilia array is capable of different aquatic motions such as flapping, bending and oscillation when driven wirelessly by different external electric fields.

5.1.2 Fabrication of Cilium-Inspired, Electroactive Fibers

The electroactive ionomer fibers were fabricated from Nafion precursor resin through a melt-drawing process (Fig. 5.1). First, the inactive perfluorinated precursor resin in the sulfonyl fluoride ($-\text{SO}_2\text{F}$) form was placed in a custom-made extruder die and preheated. As a perfluorinated precursor resin, Nafion polymer does not have the ion-exchange capability and is thermoplastic and can be easily melt-processed into variety of shapes. The custom extruder die assembly (shown in Fig. 5.1, top-center) was preheated to $240\text{ }^\circ\text{C}$ and slightly pressurized initially to generate polymer flow through the die. Then, the exiting polymer thread was drawn with uniform speed and collected around a rotating glass drum. Compared to conventional fiber extrusion, the drawing process significantly reduces the diameter size of the fiber as it exits from a die and induces the molecular orientation of polymer chains, increasing the degree of crystallinity and tensile strength of the fiber. Fibers with different dimensions were created by varying the drawing speed and collector drum distance from the die.

The obtained cylindrical Nafion fibers had to be activated by a chemical treatment to enable the cation-exchange capability. Table 5.1 describes the activation process by which the Nafion precursor was converted to 'active' sulfonic acid ($-\text{SO}_3\text{H}$) form. The first step was the hydrolysis process in hot aqueous potassium hydroxide (KOH) and dimethyl sulfoxide (DMSO) for 1 h to convert the ($-\text{SO}_2\text{F}$) functional groups into sulfonate groups ($-\text{SO}_3\text{K}$). Next, the polymer was converted to sulfonic acid ($-\text{SO}_3\text{H}$) form by treatment in a bath of H_2SO_4 solution. Finally, the polymer fibers were cleaned in deionized (DI) water to remove the acid residues.

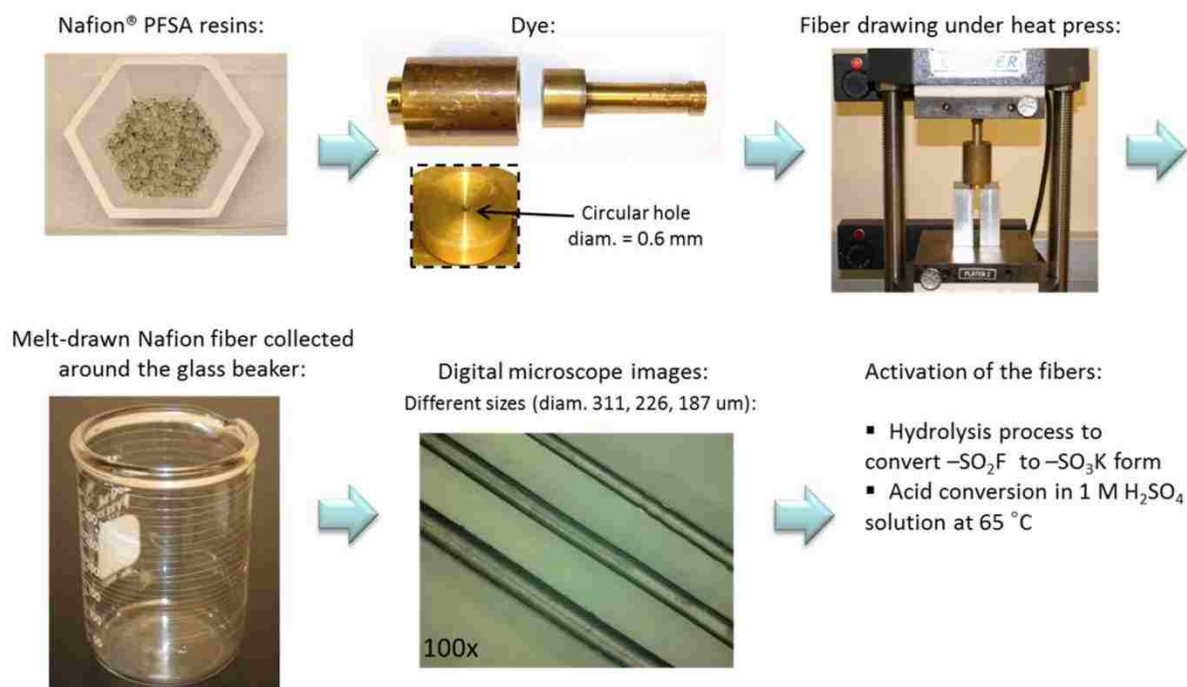


Figure 5.1: Fabrication of cylindrical electroactive ionomer fibers by melt-drawing process

Table 5.1: Activation process of ionomer cilia fibers

Procedure step	Description	Amount	Temperature	Time
1	Soak in KOH (15%), DMSO (30%)	350 mL	95 °C	1 h
2	Soak in H_2SO_4	350 mL	75 °C	3 h
3	Soak in DI water	350 mL	75 °C	45 min
4	Soak in new DI water	350 mL	75 °C	45 min

5.1.3 Experimental Methods

A cylindrical Nafion fiber fabricated by melt-drawing process was suspended in 0.1 M LiCl aq. solution between two parallel graphite electrode plates (Fig. 5.2). The distance between the electrodes was 10 mm and the effective length of the fiber was 42 mm. The bottom end of the fiber reached slightly lower than the electrodes to allow access to the laser beam for displacement measurement. A small piece of tape was attached to the fiber tip, serving as a target for a laser beam. A laser displacement sensor with National Instruments/LabView DAQ system was used for measuring the fiber tip displacement under AC square-wave input of 5 V at frequencies from 0.1 to 1 Hz.

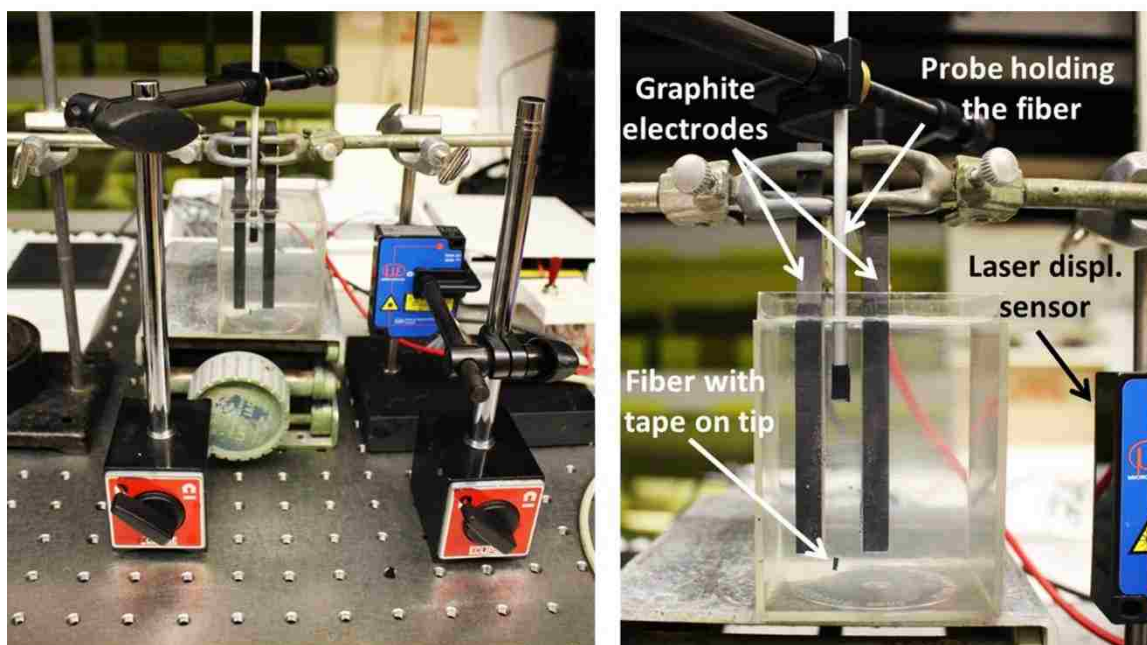


Figure 5.2: Experimental setup used for measuring the displacement of electroactive ionomer fiber under external electric field

5.1.4 Results and Physics-Based Modeling

Figure 5.3 shows the fabricated EAP microfibers in different diameter sizes – 32 μm and 55 μm produced by melt-drawing process using a 175- μm and 210- μm diameter die, respectively. The fabricated ionomer fibers have a smooth surface morphology and circular cross-section. The thickness of the melt-drawn fibers is highly dependent on the die size and drawing speed. To down-scale the diameter size of the EAP fibers, the die size was significantly reduced. Table 5.2 shows the size range of the fibers produced with different dies. With the smallest 175- μm die, EAP fibers in diameter of 25–45 μm were successfully created.

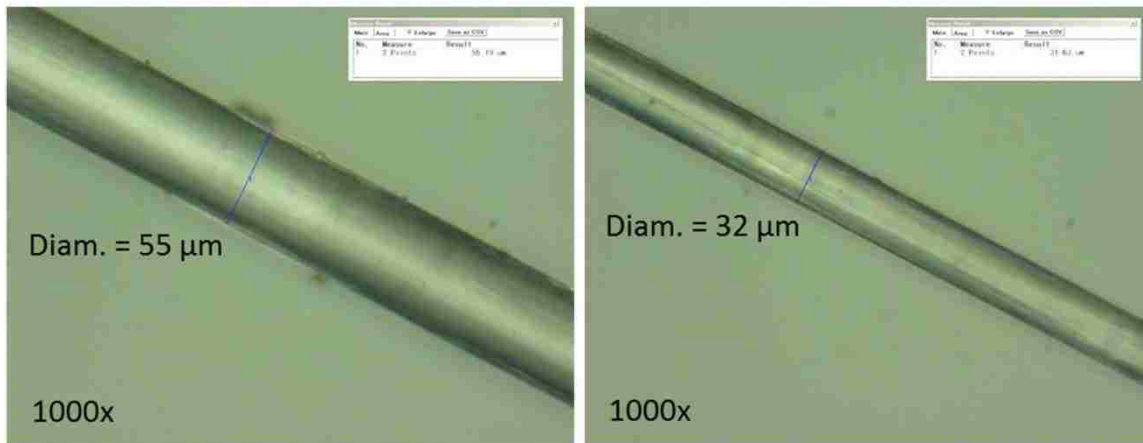


Figure 5.3: Digital optical microscope images of the fabricated EAP microfibers in different sizes

Table 5.2: Die sizes used for down-scaling the size of cylindrical EAP fibers.

Die diameter size (μm)	Fiber diameter range (μm)
610	200–300
310	70–100
210	30–55
175	25–45

To demonstrate electromechanical actuation of the new actuators, an individual EAP fiber in cantilever configuration with a free-length of 42 mm was suspended between two graphite electrode plates with a distance of 10 mm and immersed in 0.1 M LiCl aqueous electrolyte solution (Fig. 5.2). The electric field was applied to the (external) graphite plates to wirelessly actuate the fiber. Figure 5.4 shows the measured voltage and displacement responses in time for the EAP fiber micro-actuator under an external field of 5 V AC square-wave at 0.1 Hz and 1 Hz. It can be seen that the fiber exhibits repeatable cyclic actuation performance with adequate response. Unlike IPMC actuator that bends toward the positive electrode (anode), the EAP fiber deflects toward the negative electrode (cathode). This can be explained by the fact that Nafion is a cation-exchange polymer that can only pass or conduct cations but is non-transparent to anions. Since the Nafion membrane (fiber) does not have a charged electrode boundary at the surface as in case of IPMC with surface electrodes, the cations (Li^+) of the electrolyte migrate through the ionic polymer under the imposed electric field. This results in a cationic current in the polymer that draws the fiber along toward the negative (external) graphite electrode. At the same time, the anionic current of Cl^- ions toward the opposite electrode (anode) has no effect on the fiber as the anions are unable to freely move. Furthermore, the voltage-dependent displacement curves are different than conventional IPMC actuators, as can be observed in the voltage-displacement curve in Fig. 5.5, displaying large hysteresis.

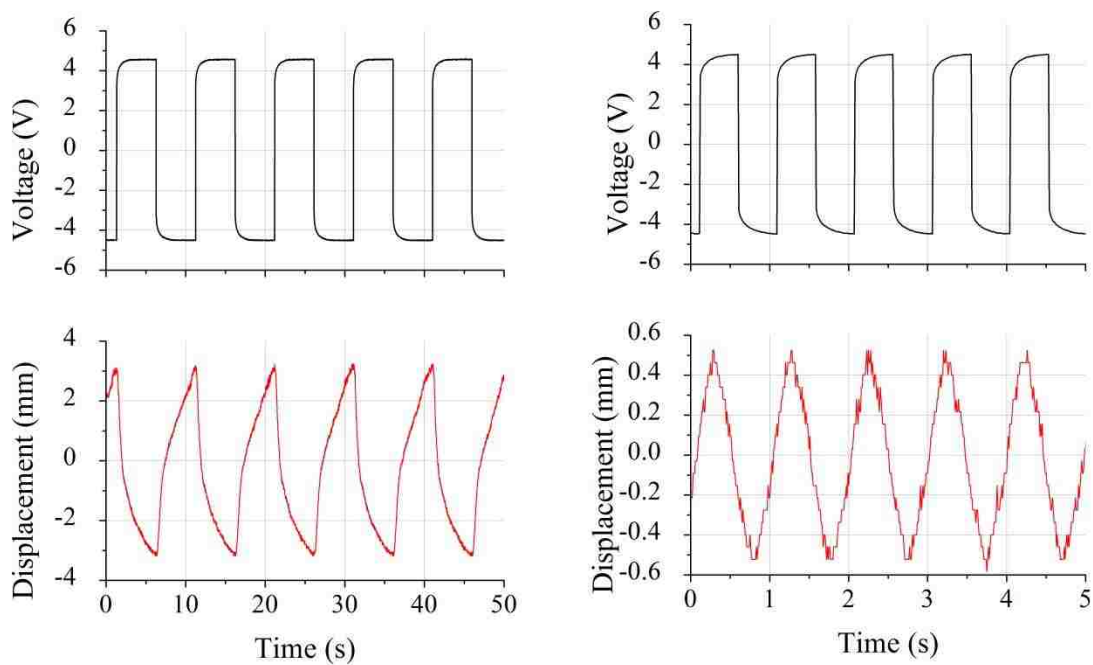


Figure 5.4: Applied voltage and measured displacement response of a cylindrical EAP fiber micro-actuator at 5 V AC square-wave at 0.1 Hz (*left*) and 1 Hz (*right*) operating frequencies in 0.1 M LiCl aq. solution at 10 mm electrode spacing

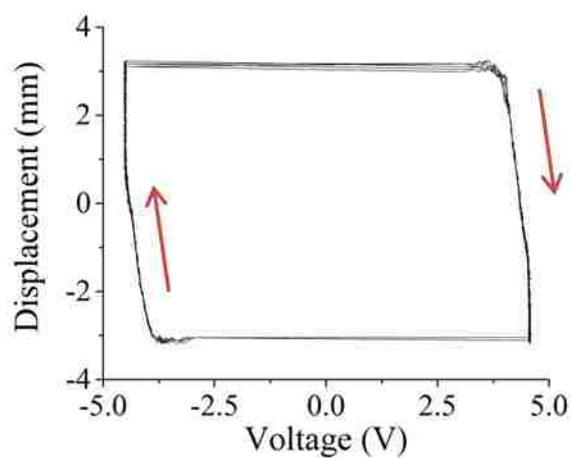


Figure 5.5: Displacement response versus applied voltage for a cylindrical EAP fiber micro-actuator at 5 V AC square-wave at 0.1 Hz operating frequency in 0.1 M LiCl aq. solution at 10 mm electrode spacing

The same experiment was also conducted in ultrapure de-ionized water (resistivity $18.2 \text{ M}\Omega \cdot \text{cm}$). In this case the actuation would only rely on Li^+ ions inside the ionomer fiber that balance the fixed anionic functional groups ($-\text{SO}_3^-$), which are present due to previous exposure to LiCl electrolyte. However, even at much higher electric fields ($> 10 \text{ V/mm}$) the fiber exhibited minimal actuation and the response was hesitant. Conducting the experiment in an electrolyte solution (NaCl or LiCl , $\geq 0.1 \text{ M}$) reduced significantly the required potential and produced much larger/stronger displacement response. Thus, the actuation of EAP fiber is driven by the transport of cations (or cationic current) through the ionomer fiber, as illustrated in Fig. 5.6(a). Figure 5.6(b) shows the actuation schematic of a conventional IPMC for comparison. In application perspective, actuating the fibers in electrolyte salt solutions would be very convenient as the EAP fibers are intended for use in underwater applications where typical salinity of seawater is $\sim 0.5\text{-}0.6 \text{ M}$ (NaCl). Therefore, the prepared EAP fibers would be further investigated in marine environment (NaCl solution) in the future.

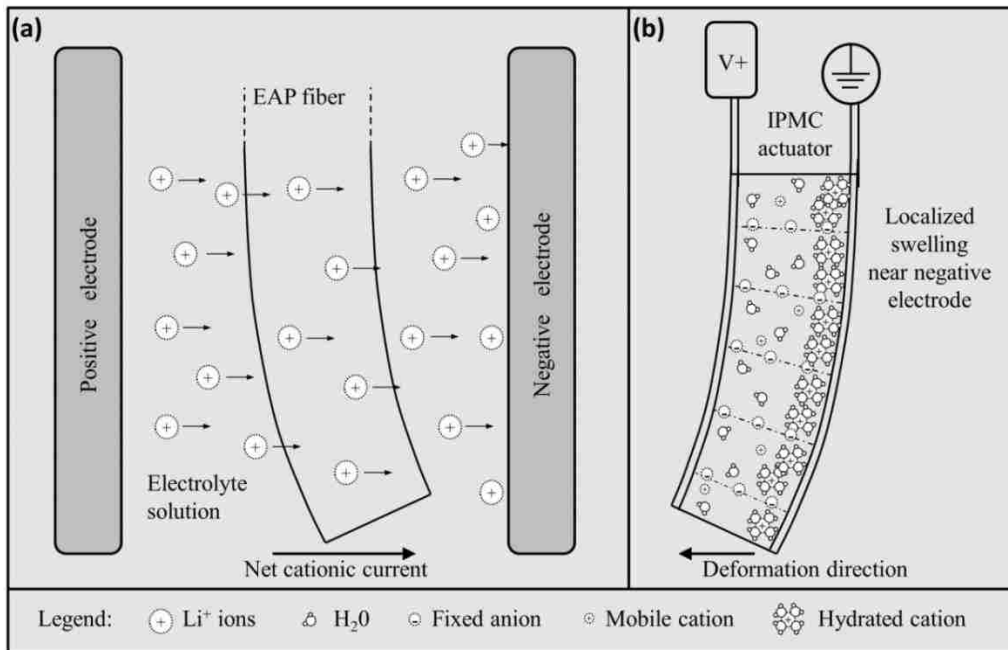


Figure 5.6: Illustration of actuation mechanism of an electrodeless EAP fiber in electrolyte solution under an imposed electric field (a), with a schematic of the actuation mechanisms of a traditional IPMC for contrast (b)

Preliminary 2D finite element physics-based modeling in COMSOL® Multiphysics 5.2 of a Nafion EAP fiber immersed in a 0.1 M LiCl solution was performed based on the physics discussed above. The results show good agreement for fiber tip-displacement using governing physics as shown in Fig. 6(b) as a simplified illustration, using the Poisson-Nernst-Planck equations for diffusion and charge density within the polymer membrane and primary current distribution physics for the electrolyte solution. The primary difference to modeling of conventional IPMC actuators is in the additional electrolyte physics, utilizing the primary current distribution physics module. Additionally, there are no electrodes or electric current physics at the Nafion fiber surface. The electrodes are instead 100 mm² surface area electrodes separated by 10 mm to correspond with experimental data of Fig. 5.4. Utilizing the Nernst-Planck and Poisson’s equations as described in Eqn. (4.6) and (4.7).

Primary current distribution physics are used in the electrolyte domain. With the equation for electrolyte potential given as:

$$-\Delta\phi_l = \frac{Q}{\sigma} \tag{5.1}$$

where ϕ_l is the electrolyte potential, Q is the electrolyte charge, and σ is the electrolyte conductivity. A Dirichlet boundary condition is applied at the electrolyte – polymer interface. Table 5.3 provides the parameter values used in simulations.

Similar to conventional IPMC actuator modeling, a linear elastic material model with Newton’s second law is utilized to solve deformation in the polymer fiber. With Newton’s Second Law given as in Eqn. (4.22), where the component of the body force vector across the bending direction of the Nafion fiber is assumed to be proportional to the charge density within the polymer, that is:

$$F_x = \alpha \rho \tag{5.2}$$

where α is the force-coupling coefficient, which is experimentally calibrated.

Table 5.3: Parameter values used in simulations of EAP fibers.

Parameter	Value
D	$7\text{e-}11 \text{ m}^2/\text{s}$
F	$96485.3415 \text{ s}\cdot\text{A}/\text{mol}$
R	$8.31 \text{ J}/(\text{mol}\cdot\text{K})$
T	293 K
C_a	$1,200 \text{ mol}/\text{m}^3$
ε	$2 \text{ mF}/\text{m}$
σ	$3 \text{ mS}/\text{cm}$
ρ_p	$2000 \text{ kg}/\text{m}^3$
α	$1.5\text{e-}7 \text{ V}/\text{m}$

Simulation results for a 200 μm diameter, 40 mm long, EAP fiber submerged in LiCl electrolyte exposed to a 5 V, 1Hz AC square wave, with 100x100 mm surface area electrodes spaced 10 mm apart, are shown in Fig. 5.7. A comparison to experimental results is included for the same operating conditions. These results show good agreement with experimental data, indicating the model adequately captures the underlying actuation physics. Mesh refinement was performed up to 250,832 domain elements showing less than 2% solution change. A close-up of the final utilized mesh at the free-end of the EAP fiber is shown in Fig. 5.7.

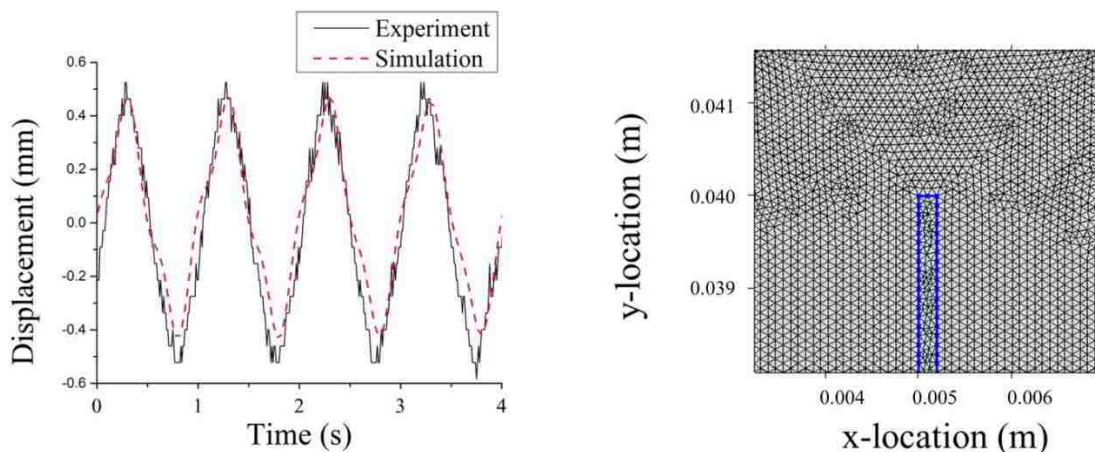


Figure 5.7: Finite element simulations of an EAP fiber in electrolyte solution as actuated by a 5V, 1Hz square wave applied to electrodes spaced 10 mm apart with comparison to experimental results (*left*), and a close-up of the mesh used for simulations on the free-end of the fiber (*right*)

5.1.5 Development of a Prototype Biomimetic Cilia Array

The fabricated cylindrical ionomer fibers were used as artificial cilia for designing a prototype cilia array. The biomimetic AM cilia array system was fabricated on a soft and flexible polydimethylsiloxane (PDMS) silicone elastomer substrate. The PDMS substrate was prepared using Sylgard® 184 silicone elastomer (Dow Corning). The PDMS pre-polymer mixed at a 10:1 weight ratio of elastomer to hardener was cast into a mold and cured at room temperature for 48 h to obtain a flexible rubber-like substrate layer.

For accurate placement of cilia fibers, an array of holes with diameter of 50 μm was pre-drilled into the PDMS layer using a CNC milling machine. Figure 5.8(a, b) shows microscopy images of the drilled holes. The melt-drawn ionomer microfibers were then planted into the PDMS substrate under a digital microscope using 29-gauge hypodermic needle. The process of fixing cilia fibers in the substrate is illustrated in Figure 5.8(c, d, e). First, a needle with an ionomer fiber was inserted along the pre-drilled hole and pushed slightly through the substrate. Then, the tip of the fiber was temporarily clamped

while pulling out the needle, leaving the ionomer fiber securely fixed in a PDMS substrate. Figure 5.8(*f, g*) shows the prototype AM cilia array system consisting of 20 fibers in row with 1 mm spacing in between. The diameter size of the fibers used in this prototype ranges from 70 to 90 μm and free length is 8 mm. The substrate dimensions are 3.6 mm (W) x 2.4 mm (H) x 23 mm (L).

In order to actuate the AM cilia array by an external electric field, a clamp device with 6 external electrodes was designed (Fig. 5.9). The electrode assembly was fabricated from acrylic glass and electrodes were made from Pt foil (thickness 0.001 in). The clamp device consists of 3 sections (pairs) of electrodes that can be used to create a wave-like oscillation of cilia when sections are driven with phase difference. Figure 5.9(*b*) shows the prototype cilia fiber (1x20) array mounted between the electrodes and immersed in electrolyte solution. The electrodes shown are spaced 3.6 mm apart.

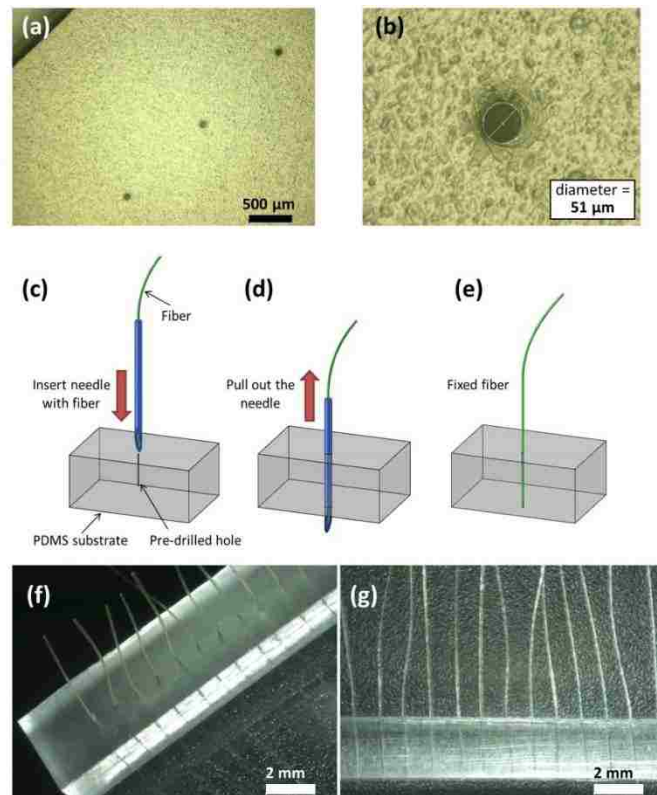


Figure 5.8: PDMS substrate with pre-drilled 50- μm holes for placement of EAP microfibers (*a, b*), process of fixing the ionomeric cilia fibers into a PDMS substrate (*c, d, e*), and digital optical microscope images of fabricated prototype AM cilia array with 1 mm spacing in between artificial cilia fibers (*f, g*)

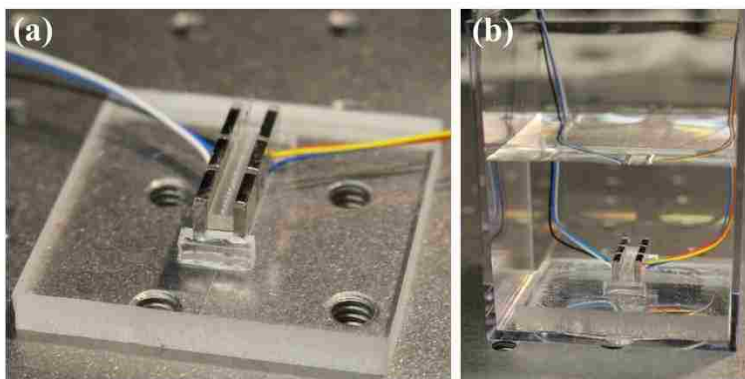


Figure 5.9: Clamp device with 6 external Pt electrodes for actuating the cilia (1x20) array by external field (a), and the artificial cilia array (1x20) mounted between electrodes and immersed in electrolyte solution (b)

The prototype artificial cilia array was actuated by applying a 5 V AC, 0.5 Hz square wave input to alternating electrodes in a LiCl electrolyte solution. Video was collected at 30 frames per second. Tip-displacement measurements were collected from the video at a rate of 10 Hz. The fibers show actuation displacements of several millimeters for the given case. Measured data and photographs from time of maximum displacements are shown in Fig. 5.10.

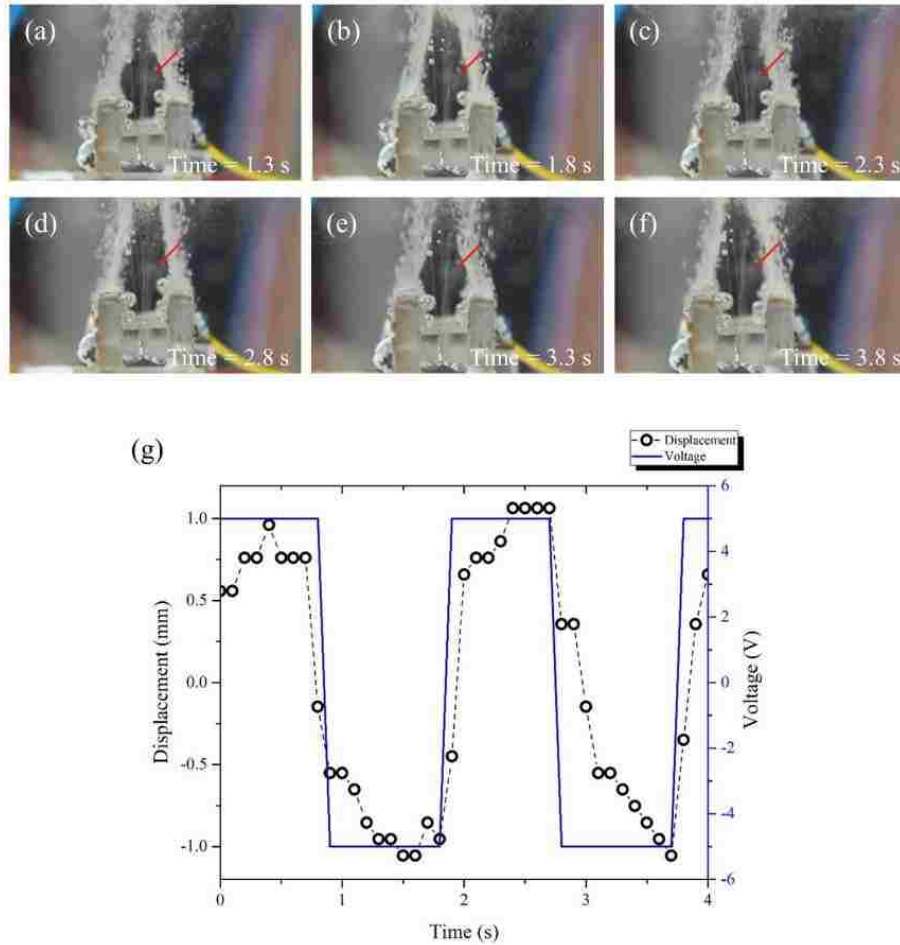


Figure 5.10: Experimental results for a microfiber array actuated by separated electrodes at 5 V AC, 0.5 Hz square wave input applied to electrodes spaced 3.6 mm apart. Still photograph from video at times $t=1.3$ seconds (a), $t=1.8$ s (b), $t=2.3$ s (c), $t=2.8$ s (d), $t=3.3$ s (e), $t=3.8$ s (f), and measured tip-displacement measurements of an individual fiber of the array (g)

The developed cilia-based micro-actuators are realizable and have been successfully implemented in a prototype microfiber array for prospective applications in underwater robotics and microfluidics. The micro-actuators can be wirelessly driven by low external electric field. They operate with low electronics requirements and can be designed as alternating actuators and sensors in different geometrical arrangements. Fabrication techniques as described are scalable up or down to meet desired design criteria. Application with microfibers acting as both sensors and actuators is being investigated for a full flow sensing and control system. This type of microarray device has many

promising applications in microfluidics, robotics, and general marine operations. Problems such as accurate environmental sensing, *in situ* boundary layer and near-surface flow measurement, and chaotic or turbulent flow sensing and control can be addressed using this technology. This can be applied to underwater vehicles to improve handling and maneuverability, medical operations in cell and drug transport, and other capillary flow or microfluidic problems. Upon further development, this technology can play a significant role in achieving more advanced underwater robotic systems. The newly developed prototype artificial muscle array of microfibers presented above is crucial groundwork to further developments of active materials as employed in microfluidics and marine biomimetic studies.

Future work includes building an understanding for cilium motion and utilizing finite element modeling for design optimization. Further developments will be done in attempt to replicate similar motion to that of natural cilium. This can be expanded into arrays of cilia with phase shifts to move similarly to how systems of cilia move together. Natural cilia are able to produce consistent flow, locomotion, and organism displacement control. The ability to replicate natural cilia will benefit robotics, such as in bio-mimicry for artificial organs. Artificial cilia technologies of this type would be ideal for certain microfluidics, flow sensing and control systems, small organism locomotion, or similar application in biomedical devices.

CHAPTER 6. EXAMPLE APPLICATIONS OF THE MODEL FRAMEWORK

In this chapter, several unique applications of the modeling framework are investigated, specifically IPMC interaction with fluid flow, modeling of an all-vanadium redox flow battery system, and modeling of anion-exchange membrane (AEM) type ionic electroactive polymer actuators. In case of modeling interaction with fluids, IPMC sensors are of primary interest for understanding sensor response to certain flow conditions, for future applications as underwater environmental sensing instruments. The governing physics are of solid mechanics for deformation with Navier-Stokes for the surrounding flow. COMSOL Multiphysics 5.2 was utilized, allowing for application of a moving-mesh for the deformed geometry. Simulation results are presented and discussed. For modeling the all-vanadium flow battery, the governing physics are of Nernst equation with Butler-Volmer law for kinetics, and chemical reaction physics for the electrodes. In case of anion-type ionic electroactive polymer devices, a simple 1-D model has been made to compare solutions of the Nernst-Planck and Poisson's equations for a traditional IPMC to the anion-type actuator. These results aim to provide example further applications with the modeling framework for ionic electroactive polymer devices.

6.1 IPMC Interaction with Fluid Flow

IPMC interaction with fluid flow is of interest to develop advanced underwater sensor and actuation devices for naval or other maritime operations. A fluid-control system could potentially be developed using ionic electroactive polymer devices for both flow measurement and control near the surface of an object. In this section, finite element simulations of a rectangular IPMC in response to different flow rates is presented and discussed.

COMSOL Multiphysics 5.2 is utilized for simulations. A fluid-structure interaction model is utilized to find the deformation of an IPMC for a given flow field. The ion concentration physics within the polymer

membrane are solved in the same way as in Chapter 3, simultaneously with the fluid-structure interaction, and a simulated voltage signal is produced at the IPMC clamp. The IPMC dimensions in the given model are width X length X height of 10mm x 50mm x 0.5mm, with a 10mm clamped region. Parameter values used in simulations can be found in Table 3.4. The channel dimensions utilized were 1000mm x 1000mm with the IPMC located 200mm from the outlet on the left-hand wall. The inlet flow was given as a normal inflow with flow velocities ranging from 0.1 m/s to 0.5 m/s. Figure 6.1 displays the simulation geometry and flow streamlines for a normal inflow of 0.1 m/s. The IPMC is in the bottom-left of the channel, at location (0, 0).

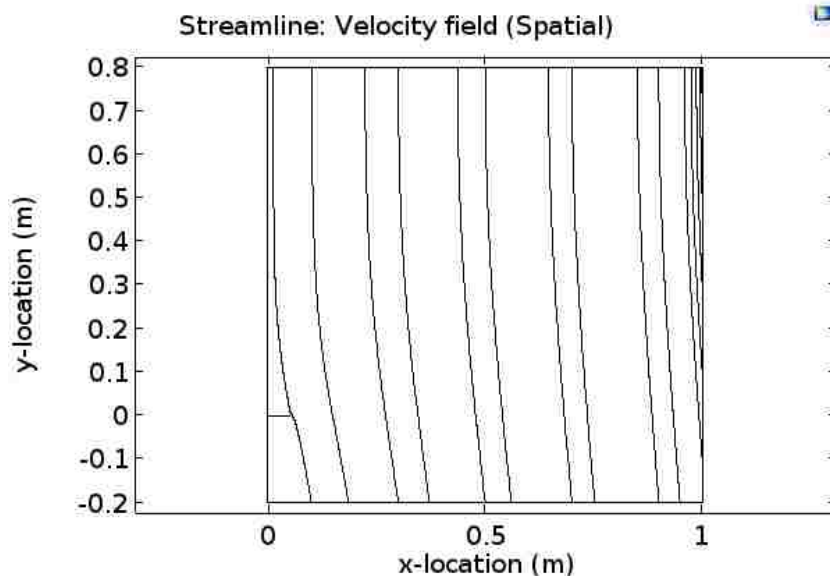


Figure 6.1: Simulated streamlines for the 0.1 m/s flow velocity condition

The free-end IPMC displacement and simulated voltage measurable at the IPMC electrodes are tabulated for a range of inflow velocities in Table 6.1. As one would expect, the simulated electrode values increase with increasing flow velocity. For the given IPMC dimensions and flow velocity range of 0.1 m/s to 0.5 m/s, the IPMC free-end displacement ranges from 0.4mm to 8.8mm. However, the

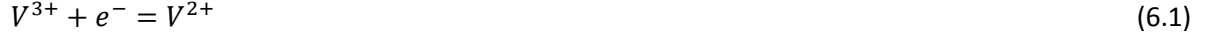
output signal is quite low, ranging only from 0.01mV to 0.22mV. This is expected for IPMC sensors, especially given the low free-end displacements involved in the low flow rate simulations (see Fig. 3.3 and Fig 3.7).

Table 6.1: Simulation results of free-end displacement and electrode signal of a rectangular IPMC fluid-structure interaction for various flow velocities for a rectangular IPMC of dimensions 10mm x50mm x0.5mm.

Inlet flow velocity (m/s)	Simulated IPMC free-end displacement (mm)	Simulated electrode signal (mV)
0.1	0.4	0.01
0.2	1.4	0.035
0.3	3.2	0.08
0.45	7.2	0.18
0.5	8.8	0.22

6.2 Flow Battery Systems

Another interesting problem that operates by similar underlying physics to an ion electroactive polymer device is simulation of flow battery systems. In the current example, simulation results of charge dynamics in an all-vanadium redox flow battery device are presented and discussed. The underlying physics are similar to those of Chapter 3, namely using the Nernst-Planck equations for species transport as described in Eqn. (3.5). Additional physics to describe the chemical reactions at the electrode-electrolyte interface are present, along with the Butler-Volmer law for charge kinetics, and Faraday's law for the electrolyte current density [84]. The negative electrode reaction can be written as



The positive electrode reaction can be written as



where ions in the negative electrolyte are H^{+} , HSO_4^{-} , SO_4^{2-} , V^{3+} , and V^{2+} . Ions present in the positive electrolyte are H^{+} , HSO_4^{-} , SO_4^{2-} , VO^{2+} , and VO_2^{+} . Conservation of charge for charge density in the electrolyte and the electrode can be written as

$$\nabla \cdot \bar{i}_l + \nabla \cdot \bar{i}_s = 0 \quad (6.3)$$

where \bar{i}_l is the charge in the liquid electrolyte and \bar{i}_s is the charge in the solid electrode. The electric potential in the electrode is given by Ohm's law. With associated chemical reaction kinetics using the Butler-Volmer law as

$$\nabla \cdot \bar{i} = i_{0,i} \left\{ \exp \left[\frac{\alpha_{a,i} F \eta_i}{RT} \right] - \exp \left[- \frac{\alpha_{c,i} F \eta_i}{RT} \right] \right\} \quad (6.4)$$

where $\alpha_{a,i}$ is the transfer coefficient of the anion, $\alpha_{c,i}$ is the transfer coefficient of the cation, η_i is the activation over potential, F is Faraday's constant, R is the universal gas constant, and T is the temperature.

An all-vanadium oxidation-reduction (redox) flow battery has been developed in-lab at UNLV for experimental investigation to advance understanding and development of flow battery devices. Figure 6.2 shows the flow battery system with pump and electrolyte reservoirs.

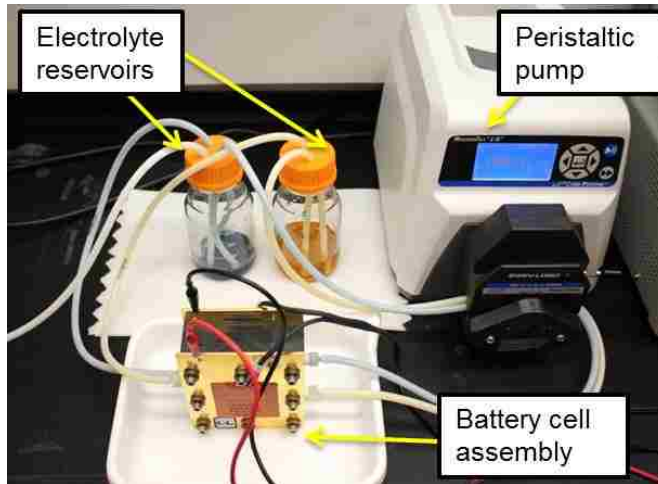


Figure 6.2: In-lab all-vanadium redox flow battery system for experimental investigation (Figure and battery cell assembly courtesy of V. Palmre)

Preliminary experimental tests were performed at charging and discharging of 40 mA/cm^2 at an electrolyte flow rate of 10 ml/min . Figure 6.3 shows the charge-discharge curves for 3 cycles.

Preliminary simulation results for the same conditions as those for the experimental test are shown in Fig. 6.4 and Fig. 6.5.

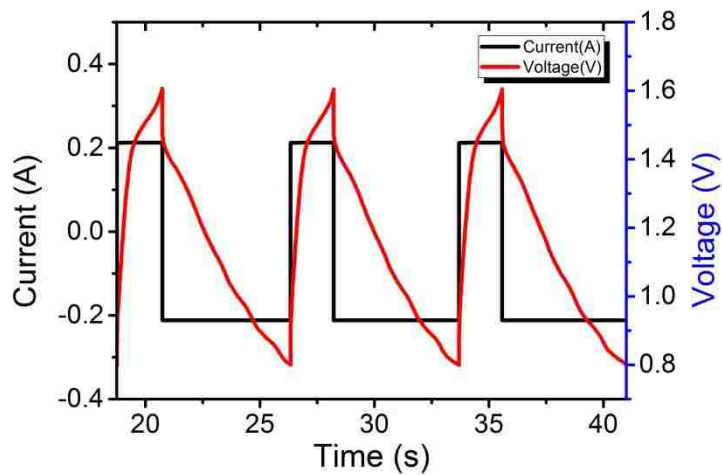


Figure 6.3: All-vanadium redox flow battery experimental results for cycles 2 through 4 of charging/discharging at 40 mA/cm^2 with a volume of 15 ml of electrolyte in each reservoir and a flow rate of 10 ml/min (Figure courtesy of J.W. Park)

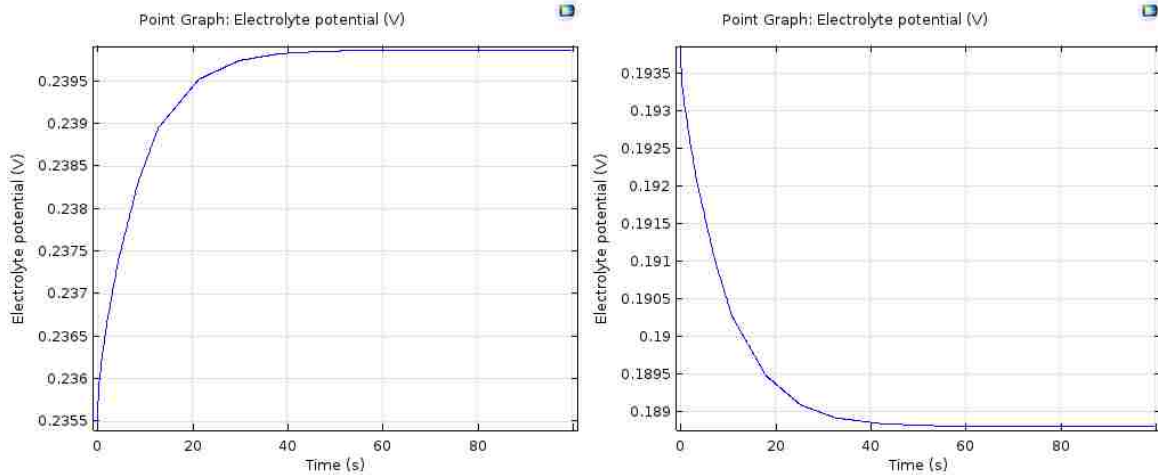


Figure 6.4: Preliminary simulation results of electrolyte potential for charging (*left*) and discharging (*right*) cycles

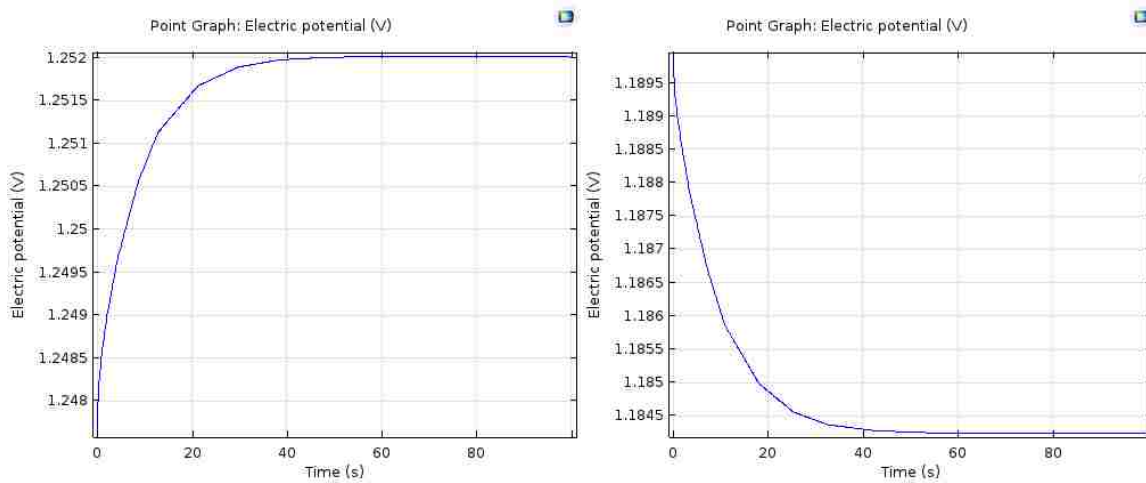


Figure 6.5: Preliminary simulation results of electrode potential for charging (*left*) and discharging (*right*) cycles

Simulation results and experimental results are similar in form; however, the model needs further calibration to achieve accurate magnitude and charge/discharge times. Additionally, the experimental results show unusual discharge curves, indicating there are design issues with the experimental flow battery system.

6.3 Anion Exchange Membrane IPMCs

An anion exchange membrane (AEM) is typically made of an ionomer which transports negatively charged ions and restricts transport of positive ions, similar to, but opposite in transport mechanisms, as the cation exchange membranes used in IPMCs. This type membrane has been utilized in applications such as alkaline anion exchange membrane fuel cells, offering certain advantages over cation exchange based fuel cells, including utilization of lower conductivity electrodes due to high over-potentials. In case of IPMCs, as previously discussed, fabrication of the electrodes by state-of-the-art methods is currently expensive, requiring multiple chemical depositions of gold, platinum, or palladium to achieve suitable electrode conductivity. Implementing anion exchange membranes as the IPMC ionomer may show promise for reducing fabrication time and cost. In this section, a simple actuation model based on the IPMC modeling framework is developed to compare performance of such devices to traditional IPMC simulations. The model for anion exchange membrane ionic polymer-metal composite actuators utilizes the same COMSOL physics modules as throughout this work, namely transport of diluted species and general form PDE modules to achieve the set of Poisson-Nernst-Planck equations. The primary differences are in the membrane properties and simulation results. As one would expect, simulation results suggest anion-type IPMC displacement in the opposite direction as that of traditional IPMCs.

A simple, 1D variation of the IPMC modeling framework has been used for comparison of mobile-cation and mobile-anion membrane type actuators. The 1D model variation has been chosen to achieve highly refined mesh size without being restricted by computational power. The distance between boundaries was given as 0.5mm. The basic geometry is shown in Fig. 6.6, where a sine wave input of 0.5 V magnitude, 1 Hz frequency was used as input, applied to the left boundary identified by "Positive V+" starting at time $t=0$ seconds.

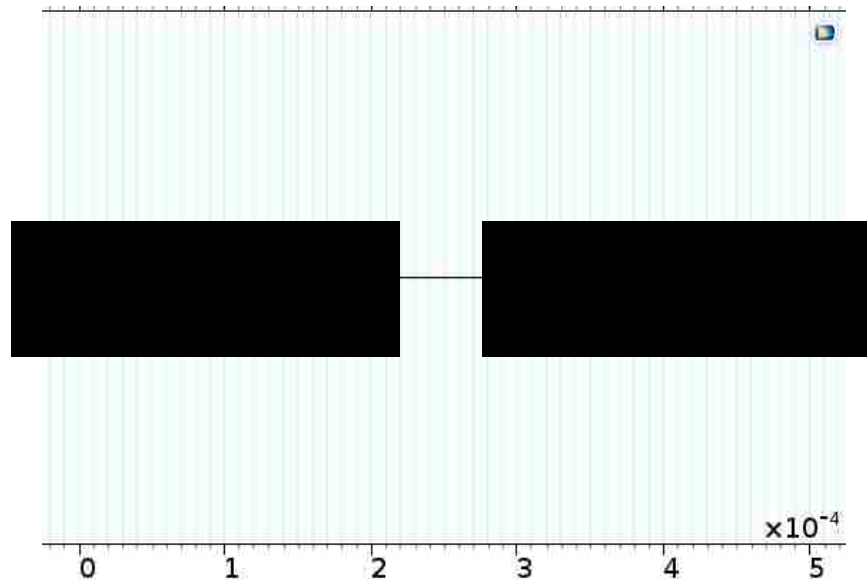


Figure 6.6: 1D simplified geometry for rapid-simulation comparison of actuator components

The 1D geometry shown in Fig. 6.6 is utilized for comparing cation-exchange and anion-exchange membrane type IPMC actuators. These results provide theoretical predictions of the ion concentration changes within these devices for similar operating conditions. Table 6.2 has the model parameter values used in this section. The cation-exchange IPMC simulations are performed assuming a Nafion 117 membrane with Li^+ mobile-cations at an initial concentration of 1200 mol/m^3 . The anion-exchange IPMC simulations are performed assuming a Nafion 112 membrane with CO^- mobile anions at an initial concentration of 24.50 mol/m^3 [85].

Table 6.2: Values used in simulations for cation/anion-exchange membrane comparisons.

Item	Cation-exchange IPMC	Anion-exchange IPMC
Diffusion coefficient (m^2/s)	$1\text{e-}10$	$1.153\text{e-}11$
Charge coefficient, z	+1 (for Li^+ ions)	-1 (for CO^- ions)
Initial ionic concentration	1200 mol/m^3	24.50 mol/m^3

For the case of the mobile-cation membrane based IPMC actuator, the results were as anticipated with a steep gradient of cation rise in a small, near-boundary region of less than $5\ \mu\text{m}$ in length near the negative electrode. The cation concentration change across the domain in time is shown in Fig. 6.7. The steep rise corresponds to a positive peak in the sine wave input signal at the opposite boundary during those times. A close-up of the $5\ \mu\text{m}$ near boundary region is included in Fig. 6.7 for higher detail.

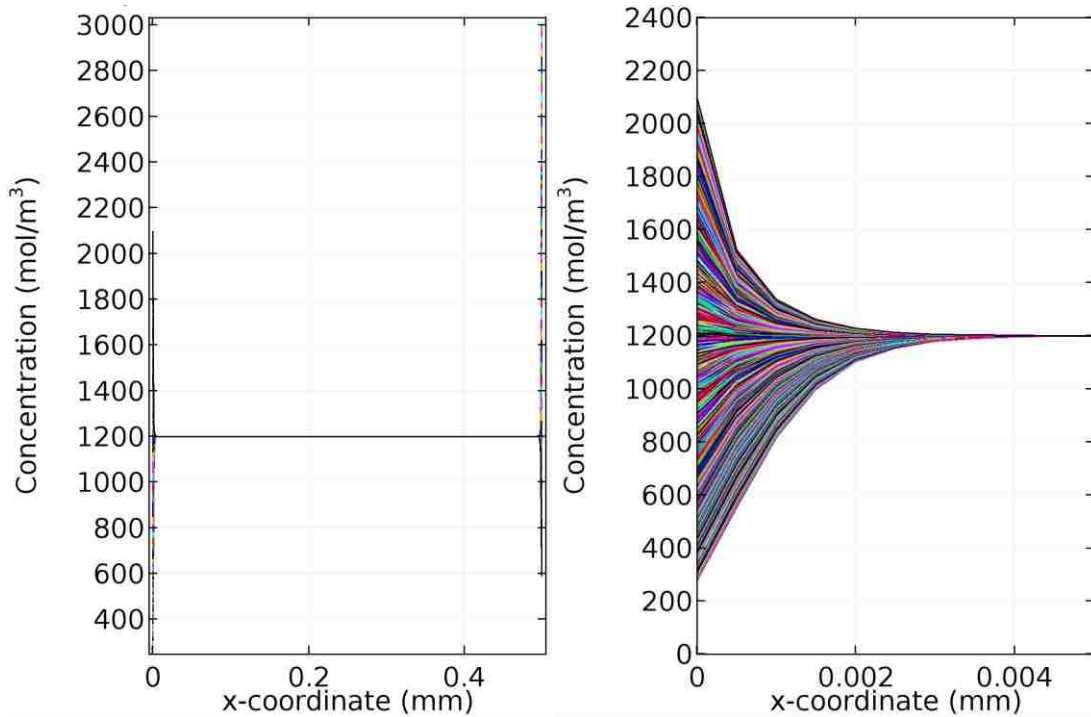


Figure 6.7: Simulated cation concentration for mobile-cation (traditional) type IPMC actuator across 1D domain (*left*) and in a small, near-boundary region (*right*) for mobile-cation type IPMC actuators

Temporal change in concentration at the right-most (V-) boundary for a traditional mobile cation based membrane IPMC actuator in response to a 0.5 V, 1 Hz sine wave is shown in Fig. 6.8. The direction of cation change is in the expected direction.

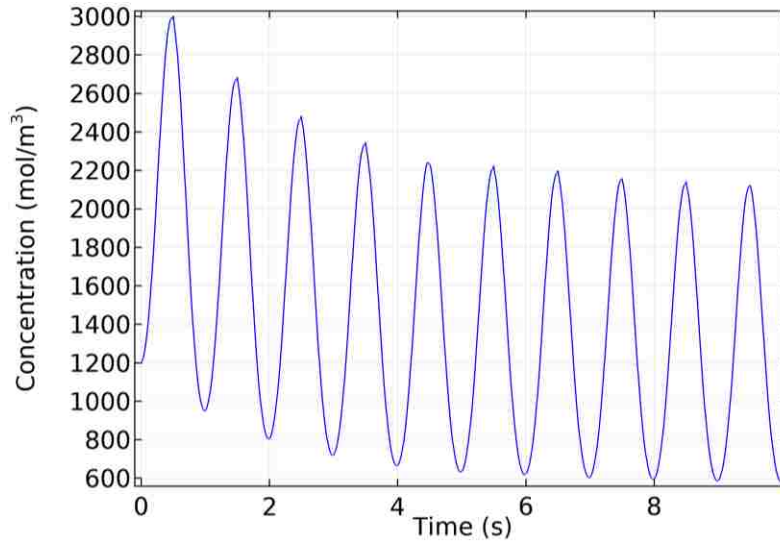


Figure 6.8: Simulated cation concentration change at right-most boundary of a mobile-cation IPMC in response to a 0.5 V, 1 Hz input signal across a 0.5 mm domain

For the case of the mobile-anion membrane based IPMC actuator, the results were as anticipated as the opposite of that seen with the mobile-cation membrane based IPMCs. Additionally, although the anion-rise was still mostly restricted to a near-electrode boundary, the change was more gradual, with the region of anion-change as about $50\mu\text{m}$ as opposed to $5\mu\text{m}$. The anion concentration change across the domain in time is shown in Fig. 6.9. A close-up of a $50\mu\text{m}$ near boundary region is also included in Fig. 6.9 for higher detail. Temporal change in concentration at the right-most (V-) boundary for the mobile-anion based membrane IPMC actuator in response to a 0.5 V, 1 Hz sine wave is shown in Fig. 6.10. The direction of anion change is in the expected direction, opposite that of cation-change for mobile-cation based membrane IPMC actuators. However, it is observed that the midpoint of the signal drifts away from the initial concentration, appearing to diverge. This is likely a numerical issue and is still being addressed.

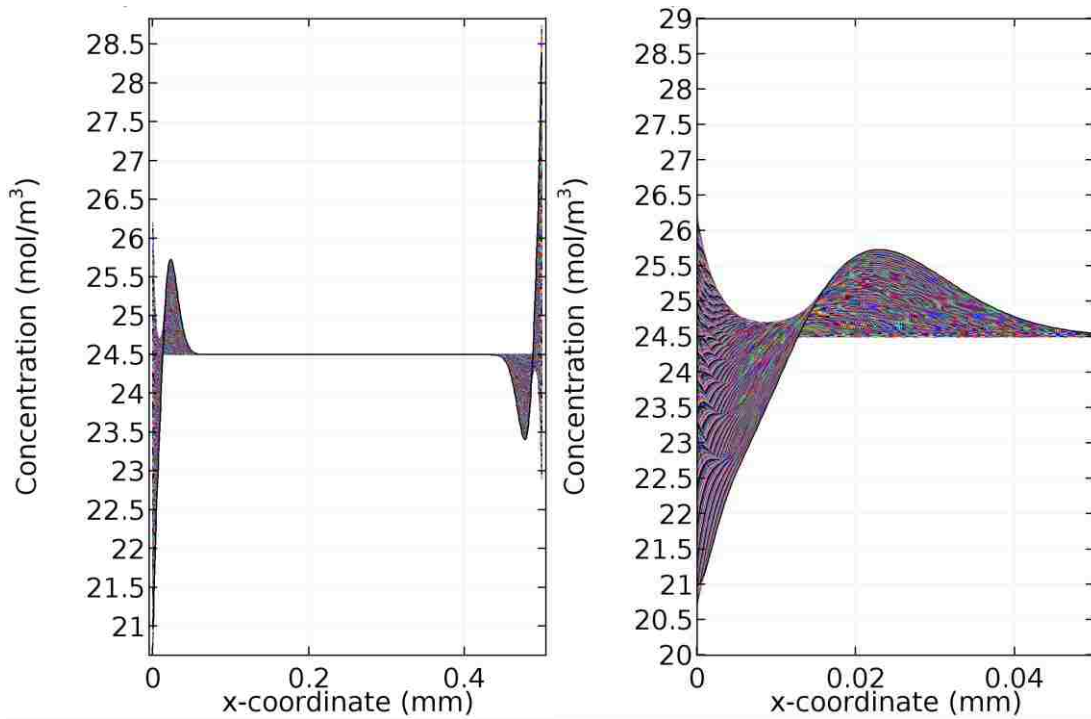


Figure 6.9: Simulated anion concentration for a mobile-anion type IPMC actuator across 1D domain (*left*) and in a small, near-boundary region (*right*) for mobile-cation type IPMC actuators

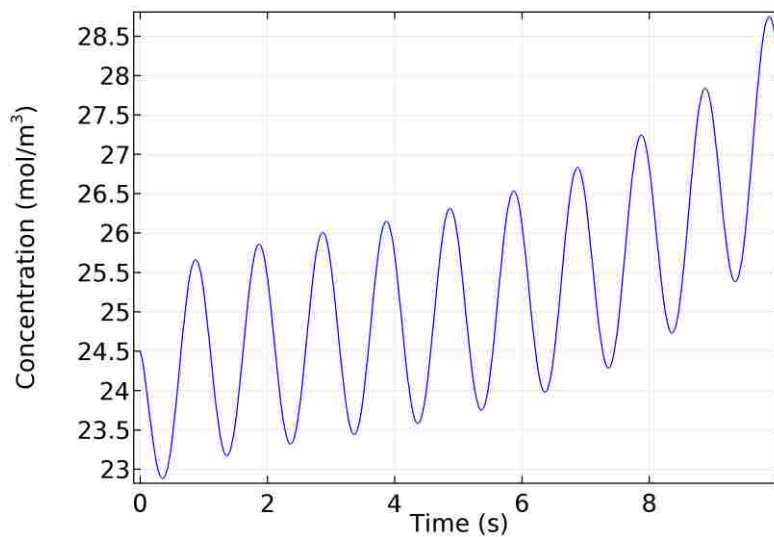


Figure 6.10: Simulated anion concentration change at right-most boundary of a mobile-anion IPMC in response to a 0.5 V, 1 Hz input signal across a 0.5 mm domain

CHAPTER 7. CONCLUSIONS

In this work, a framework model for ionic electroactive polymer devices, with specific focus on ionic polymer-metal composite materials, is presented with comparison to experimental results for exemplar cases, such as rectangular and tube-shaped IPMC devices. Additionally, a force-coupling equation is presented for DC actuation of IPMCs which can encompass back-relaxation effects. The simulation results are in good agreement with experimental cases, suggesting the physics-based model accurately depicts the underlying physics of the ion electroactive polymer devices that were investigated. The governing physics can be applied to several ion transport actuation and sensing problems, as is highlighted in Chapters 5 and 6. The presented modeling methods can assist research and development of higher-performance devices through. This will allow characterizing performance of ionic electroactive polymer devices through simulation before fabrication, which will be a significant cost reduction in further development of these devices. Cost of fabrication is currently one of the main issues hampering further industrial application of ionic electroactive polymer devices, thus utilization of the modeling methods presented within can also influence industrial application.

CHAPTER 8. RECOMMENDATIONS FOR FUTURE WORK

In this study, a modeling framework for ionic electroactive polymer devices is presented and investigated for several applications. The simulation results show good agreement with experimental tests for IPMCs of exemplar cases; however, there exist many other such ionic electroactive devices of interest that should be further investigated for development improvements. For example, anion exchange membrane based IPMCs were simulated and discussed, but still need to be experimentally validated. A full study of soft-robotic and ionic electroactive polymer devices can be carried out to compare performance and operational mechanisms. This would be beneficial to material selection for advanced applications in soft-robotics, microfluidics, biomedical engineering, and other similar fields of study.

Additionally, materials characterization and further experimental studies can be performed to improve simulation accuracy. Foremost, it is of great interest to observe the ion migration within an electroactive polymer experimentally with time during actuation and sensing. These results can be compared to simulations to experimentally validate the ion-migration results. This can be achieved with a fluorescent imaging system.

Finally, further calibration and investigation should be done for flow battery systems in order to achieve accurate simulation results. The preliminary model shows good agreement with experimental results in terms of form; however, the magnitude and time are not similar.

APPENDIX A: NOMENCLATURE

$J_{diffusion}$: Cation flux in polymer membrane of IPMC due to diffusion

$J_{migration\ in\ electric\ field}$: Cation flux in polymer membrane of IPMC due to migration in an electric field

$J_{convection}$: Cation flux in polymer membrane of IPMC due to convection

D : Diffusion coefficient

C : Cation concentration

C_a : Anion concentration

C_0 : Initial ion concentration

F : Faraday's constant

ϕ : Electric potential inside the polymer of an IPMC

ρ : Charge density inside the polymer of an IPMC

μ : Cation mobility

z : Charge number

u : Cation velocity

R : Gas constant

T : Absolute temperature

V_c : Molar volume change which quantifies cation hydrophilicity

P : Solvent pressure

p : Polymer pressure

ε : Absolute dielectric permittivity

μ_L, λ : Lamé's constants

σ_{ij} : Stresses

ε_{ij} : Strains

u_1 : Displacement in the x-direction

u_2 : Displacement in the y-direction

u_3 : Displacement in the z-direction

E : Young's modulus

ν : Poisson's ratio

\mathbf{F} : Body force

ρ_p : Polymer density

α : Experimental calibration coefficient

β : Experimental calibration coefficient

k_r : Experimental calibration coefficient

δ : Free-end displacement used in strain calculations

L : IPMC length

h : IPMC thickness

r : Radius of curvature for strain calculations

k : Nondimensional displacement used in shear strain calculations ($k = \delta_{shear}/h$)

\vec{e}_1 : Unit vector in 1-direction

\vec{e}_2 : Unit vector in 2-direction

\vec{e}_3 : Unit vector in 3-direction

J : Jacobian in strain calculations

E_{ij} : Lagrangian strain tensor

APPENDIX B: DERIVATION OF PRINCIPAL STRAIN FOR BENDING AND SHEAR CASES

Figure B.1 shows the two cases of interest for strain comparisons, where the width direction of the IPMC is into the page. For the case of bending, one can find the deformation from Fig. B.1 to be described as:

$$\vec{x} = (r - x_2^0) \sin\left(\frac{x_1^0}{r}\right) \vec{e}_1 + \left[r - (r - x_2^0) \cos\left(\frac{x_1^0}{r}\right)\right] \vec{e}_2 + (x_3^0) \vec{e}_3 \quad (\text{B.1})$$

The Lagrangian strain can be found from (B.1) as:

$$[E_{ij}] = \frac{1}{2} \left(\begin{bmatrix} \frac{\partial x_1}{\partial x_1^0} & \frac{\partial x_2}{\partial x_1^0} & \frac{\partial x_3}{\partial x_1^0} \\ \frac{\partial x_1}{\partial x_2^0} & \frac{\partial x_2}{\partial x_2^0} & \frac{\partial x_3}{\partial x_2^0} \\ \frac{\partial x_1}{\partial x_3^0} & \frac{\partial x_2}{\partial x_3^0} & \frac{\partial x_3}{\partial x_3^0} \end{bmatrix} \begin{bmatrix} \frac{\partial x_1}{\partial x_1^0} & \frac{\partial x_1}{\partial x_2^0} & \frac{\partial x_1}{\partial x_3^0} \\ \frac{\partial x_2}{\partial x_1^0} & \frac{\partial x_2}{\partial x_2^0} & \frac{\partial x_2}{\partial x_3^0} \\ \frac{\partial x_3}{\partial x_1^0} & \frac{\partial x_3}{\partial x_2^0} & \frac{\partial x_3}{\partial x_3^0} \end{bmatrix} - \begin{bmatrix} 1 & 0 & 0 \\ 0 & 1 & 0 \\ 0 & 0 & 1 \end{bmatrix} \right) = \begin{bmatrix} -\frac{x_2^0}{r} + \frac{1}{2} \left(\frac{x_2^0}{r}\right)^2 & 0 & 0 \\ 0 & 0 & 0 \\ 0 & 0 & 0 \end{bmatrix} \quad (\text{B.2})$$

where the maximum principal strain will simply be the E_{11} component, with $x_2^0 = -h/2$, that is:

$$\epsilon_{\text{principal,bending}} = \frac{h}{2r} + \frac{1}{2} \left(\frac{h}{2r}\right)^2 \quad (\text{3.15})$$

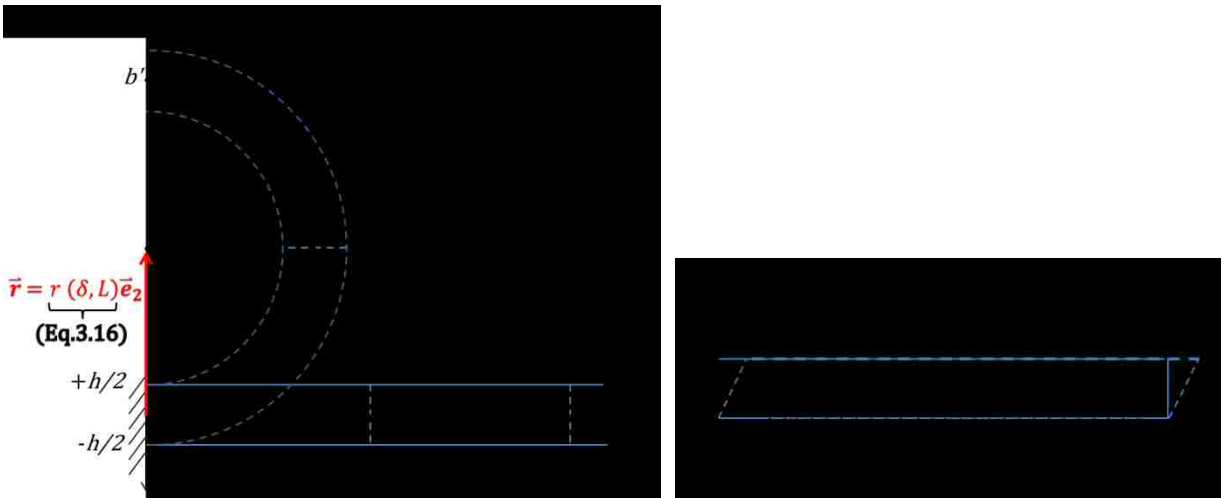


Figure B.1: Bending diagram (left) and the simple shear strain diagram (right) used for strain derivations

For a free-end displacement of δ at the center of the thickness ($x_1^0 = L$, $x_2^0 = 0$), the x_2 component of displacement can be utilized to solve for r , that is:

$$\delta = r \left[1 - \cos\left(\frac{L}{r}\right) \right] \quad (3.16)$$

From deformation equations described in (B.1), the Jacobian can be found as the determinant of the deformation gradient, that is:

$$J_{bending} = \det \begin{pmatrix} \frac{\partial x_1}{\partial x_1^0} & \frac{\partial x_1}{\partial x_2^0} & \frac{\partial x_1}{\partial x_3^0} \\ \frac{\partial x_2}{\partial x_1^0} & \frac{\partial x_2}{\partial x_2^0} & \frac{\partial x_2}{\partial x_3^0} \\ \frac{\partial x_3}{\partial x_1^0} & \frac{\partial x_3}{\partial x_2^0} & \frac{\partial x_3}{\partial x_3^0} \end{pmatrix} = 1 - \frac{x_2^0}{r} \quad (B.3)$$

with $x_2^0 = h/2$ for the top face:

$$J_{bending} = 1 - \frac{h}{2r} \quad (3.17)$$

For the case of simple shear, one can find the deformation from Fig. B.1 to be described as:

$$\vec{x} = (x_1^0 + kx_2^0)\vec{e}_1 + (x_2^0)\vec{e}_2 + (x_3^0)\vec{e}_3 \quad (B.4)$$

The Lagrangian strain can be found from (B.4) as:

$$[E_{ij}] = \frac{1}{2} \left(\begin{pmatrix} \frac{\partial x_1}{\partial x_1^0} & \frac{\partial x_2}{\partial x_1^0} & \frac{\partial x_3}{\partial x_1^0} \\ \frac{\partial x_1}{\partial x_2^0} & \frac{\partial x_2}{\partial x_2^0} & \frac{\partial x_3}{\partial x_2^0} \\ \frac{\partial x_1}{\partial x_3^0} & \frac{\partial x_2}{\partial x_3^0} & \frac{\partial x_3}{\partial x_3^0} \end{pmatrix} - \begin{pmatrix} 1 & 0 & 0 \\ 0 & 1 & 0 \\ 0 & 0 & 1 \end{pmatrix} \right) = \begin{bmatrix} 0 & \frac{k}{2} & 0 \\ \frac{k}{2} & \frac{k^2}{2} & 0 \\ 0 & 0 & 0 \end{bmatrix} \quad (B.5)$$

where the principal strains can be found by solving the Eigenvalue-Eigenvector problem for the Lagrangian strain tensor, in which one can find:

$$\epsilon_{principal, shear} = \frac{k^2}{4} \pm \frac{k}{2} \sqrt{\frac{k^2}{4} + 1} \quad (B.6)$$

APPENDIX C: COPYRIGHT PERMISSION APPROVALS

ELSEVIER LICENSE

Aug 22, 2016

This Agreement between Tyler P Stalbaum ("You") and Elsevier ("Elsevier") consists of your license details and the terms and conditions provided by Elsevier and Copyright Clearance Center.

License Number	3933880264466
License date	Aug 21, 2016
Licensed Content Publisher	Elsevier
Licensed Content Publication	Polymer
Licensed Content Title	A novel method of manufacturing three-dimensional ionic polymer–metal composites (IPMCs) biomimetic sensors, actuators and artificial muscles
Licensed Content Author	Kwang J. Kim, Mohsen Shahinpoor
Licensed Content Date	February 2002
Licensed Content Volume Number	43
Licensed Content Issue Number	3
Licensed Content Pages	6
Start Page	797
End Page	802
Type of Use	reuse in a thesis/dissertation
Portion	figures/tables/illustrations
Number of figures/tables/illustrations	1
Format	both print and electronic
Are you the author of this Elsevier article?	No

Will you be translating?	No
Order reference number	
Original figure numbers	Figure 2
Title of your thesis/dissertation	IONIC ELECTROACTIVE POLYMER DEVICES: PHYSICS-BASED MODELING WITH EXPERIMENTAL INVESTIGATION AND VERIFICATION
Expected completion date	Dec 2016
Estimated size (number of pages)	140
Elsevier VAT number	GB 494 6272 12

AIP PUBLISHING LLC LICENSE

Aug 22, 2016

This Agreement between Tyler P Stalbaum ("You") and AIP Publishing LLC ("AIP Publishing LLC") consists of your license details and the terms and conditions provided by AIP Publishing LLC and Copyright Clearance Center.

License Number	3933880787470
License date	Aug 21, 2016
Licensed Content Publisher	AIP Publishing LLC
Licensed Content Publication	Journal of Applied Physics
Licensed Content Title	Physics-based modeling of mechano-electric transduction of tube-shaped ionic polymer-metal composite
Licensed Content Author	Tyler Stalbaum, David Pugal, Shelby E. Nelson, et al.
Licensed Content Date	Mar 19, 2015
Licensed Content Volume Number	117
Licensed Content Issue Number	11

Type of Use	Thesis/Dissertation
Requestor type	Author (original article)
Format	Print and electronic
Portion	Excerpt (> 800 words)
Will you be translating?	No
Title of your thesis / dissertation	IONIC ELECTROACTIVE POLYMER DEVICES: PHYSICS-BASED MODELING WITH EXPERIMENTAL INVESTIGATION AND VERIFICATION
Expected completion date	Dec 2016
Estimated size (number of pages)	140

AIP PUBLISHING LLC LICENSE

Aug 22, 2016

This Agreement between Tyler P Stalbaum ("You") and AIP Publishing LLC ("AIP Publishing LLC") consists of your license details and the terms and conditions provided by AIP Publishing LLC and Copyright Clearance Center.

License Number	3933880872400
License date	Aug 21, 2016
Licensed Content Publisher	AIP Publishing LLC
Licensed Content Publication	Journal of Applied Physics
Licensed Content Title	Physics-based modeling of mechano-electric transduction of tube-shaped ionic polymer-metal composite
Licensed Content Author	Tyler Stalbaum, David Pugal, Shelby E. Nelson, et al.
Licensed Content Date	Mar 19, 2015

Licensed Content Volume Number	117
Licensed Content Issue Number	11
Type of Use	Thesis/Dissertation
Requestor type	Author (original article)
Format	Print and electronic
Portion	Figure/Table
Number of figures/tables	14
Title of your thesis / dissertation	IONIC ELECTROACTIVE POLYMER DEVICES: PHYSICS-BASED MODELING WITH EXPERIMENTAL INVESTIGATION AND VERIFICATION
Expected completion date	Dec 2016
Estimated size (number of pages)	140

AIP PUBLISHING LLC LICENSE

Aug 22, 2016

This Agreement between Tyler P Stalbaum ("You") and AIP Publishing LLC ("AIP Publishing LLC") consists of your license details and the terms and conditions provided by AIP Publishing LLC and Copyright Clearance Center.

License Number	3933881229827
License date	Aug 21, 2016
Licensed Content Publisher	AIP Publishing LLC
Licensed Content Publication	Journal of Applied Physics
Licensed Content Title	A comprehensive physics-based model encompassing variable surface resistance and underlying physics of ionic polymer-metal composite actuators
Licensed Content Author	Qi Shen, Viljar Palmre, Tyler Stalbaum, et al.

Licensed Content Date	Sep 29, 2015
Licensed Content Volume Number	118
Licensed Content Issue Number	12
Type of Use	Thesis/Dissertation
Requestor type	Author (original article)
Format	Print and electronic
Portion	Figure/Table
Number of figures/tables	15
Title of your thesis / dissertation	IONIC ELECTROACTIVE POLYMER DEVICES: PHYSICS-BASED MODELING WITH EXPERIMENTAL INVESTIGATION AND VERIFICATION
Expected completion date	Dec 2016
Estimated size (number of pages)	140

AIP PUBLISHING LLC LICENSE

Aug 22, 2016

This Agreement between Tyler P Stalbaum ("You") and AIP Publishing LLC ("AIP Publishing LLC") consists of your license details and the terms and conditions provided by AIP Publishing LLC and Copyright Clearance Center.

License Number	3933881139233
License date	Aug 21, 2016
Licensed Content Publisher	AIP Publishing LLC
Licensed Content Publication	Journal of Applied Physics
Licensed Content Title	A comprehensive physics-based model encompassing variable surface resistance and underlying physics of ionic polymer-metal composite actuators

Licensed Content Author	Qi Shen, Viljar Palmre, Tyler Stalbaum, et al.
Licensed Content Date	Sep 29, 2015
Licensed Content Volume Number	118
Licensed Content Issue Number	12
Type of Use	Thesis/Dissertation
Requestor type	Author (original article)
Format	Print and electronic
Portion	Excerpt (> 800 words)
Will you be translating?	No
Title of your thesis / dissertation	IONIC ELECTROACTIVE POLYMER DEVICES: PHYSICS-BASED MODELING WITH EXPERIMENTAL INVESTIGATION AND VERIFICATION
Expected completion date	Dec 2016
Estimated size (number of pages)	140

REFERENCES

1. Shahinpoor, M., Bar-Cohen, Y., Simpson, J. O., & Smith, J. (1998). Ionic polymer-metal composites (IPMCs) as biomimetic sensors, actuators and artificial muscles-a review. *Smart materials and structures*, 7(6), R15.
2. Oguro, K., Kawami, Y., & Takenaka, H. (1992). Bending of an ion-conducting polymer film-electrode composite by an electric stimulus at low voltage. *Journal of Micromachine Society*, 5(1), 27-30.
3. Shahinpoor, M. (1994). Continuum electromechanics of ionic polymeric gels as artificial muscles for robotic applications. *Smart Materials and Structures*, 3(3), 367.
4. Bar-Cohen, Y. (2006). Biomimetics using electroactive polymers (EAP) as artificial muscles-: A review. *Journal of advanced materials*, 38(4), 3-9.
5. Bonomo, C., Brunetto, P., Fortuna, L., Giannone, P., Graziani, S., & Strazzeri, S. (2008). A tactile sensor for biomedical applications based on IPMCs. *IEEE Sensors Journal*, 8(8), 1486-1493.
6. Yeom, S. W., & Oh, I. K. (2009). A biomimetic jellyfish robot based on ionic polymer metal composite actuators. *Smart materials and structures*, 18(8), 085002.
7. Palmre, V., Hubbard, J. J., Fleming, M., Pugal, D., Kim, S., Kim, K. J., & Leang, K. K. (2012). An IPMC-enabled bio-inspired bending/twisting fin for underwater applications. *Smart Materials and Structures*, 22(1), 014003.
8. Carpi, F., & Smela, E. (2009). *Biomedical Applications of Electroactive Polymer Actuators: A John Wiley and Sons. Ltd.: Chichester, UK.*
9. Tiwari, R., & Garcia, E. (2011). The state of understanding of ionic polymer metal composite architecture: a review. *Smart Materials and Structures*, 20(8), 083001.
10. Tiwari, R., Ryoo, K., Schlichting, A., & Garcia, E. (2013). Extremely low-loss rectification methodology for low-power vibration energy harvesters. *Smart Materials and Structures*, 22(6), 062001.
11. Giacomello, A., & Porfiri, M. (2011). Underwater energy harvesting from a heavy flag hosting ionic polymer metal composites. *Journal of Applied Physics*, 109(8), 084903.

12. Pugal, D., Jung, K., Aabloo, A., & Kim, K. J. (2010). Ionic polymer–metal composite mechano-electrical transduction: review and perspectives. *Polymer international*, 59(3), 279-289.
13. De Gennes, P. G., Okumura, K., Shahinpoor, M., & Kim, K. J. (2000). Mechano-electric effects in ionic gels. *EPL (Europhysics Letters)*, 50(4), 513.
14. Nemat-Nasser, S., & Li, J. Y. (2000). Electromechanical response of ionic polymer-metal composites. *Journal of Applied Physics*, 87(7), 3321-3331.
15. Porfiri, M. (2008). Charge dynamics in ionic polymer metal composites. *Journal of Applied Physics*, 104(10), 104915.
16. Porfiri, M. (2008). An electromechanical model for sensing and actuation of ionic polymer metal composites. *Smart Materials and Structures*, 18(1), 015016.
17. Park, I. S., Kim, S. M., Pugal, D., Huang, L., Tam-Chang, S. W., & Kim, K. J. (2010). Visualization of the cation migration in ionic polymer-metal composite under an electric field. *Applied Physics Letters*, 96(4), 043301.
18. Roentgen, W. C. (1880). About the changes in shape and volume of dielectrics caused by electricity. *Section III in G. Wiedemann (Ed.), Annual Physics and Chemistry Series*, 11, 771-786.
19. Desault, P. J. (1805). *A treatise on fractures, luxations, and other affections of the bones* (Vol. 1805). Fry and Kammerer.
20. Pugal, D., Kim, K. J., & Aabloo, A. (2011). An explicit physics-based model of ionic polymer-metal composite actuators. *Journal of Applied Physics*, 110(8), 084904.
21. Pugal, D., "Physics based model of ionic polymer-metal composite electromechanical and mechano-electrical transduction," PhD dissertation, UNR, (2012).
22. Bar-Cohen, Y. (2002). Electroactive polymers as artificial muscles: a review. *Journal of Spacecraft and Rockets*, 39(6), 822-827.
23. Madden, J. D., Vandesteeg, N. A., Anquetil, P. A., Madden, P. G., Takshi, A., Pytel, R. Z., ... & Hunter, I. W. (2004). Artificial muscle technology: physical principles and naval prospects. *IEEE Journal of oceanic engineering*, 29(3), 706-728.

24. Ruiz, S., Mead, B., Palmre, V., Kim, K. J., & Yim, W. (2014). A cylindrical ionic polymer-metal composite-based robotic catheter platform: modeling, design and control. *Smart Materials and Structures*, 24(1), 015007.
25. Shahinpoor, M., & Kim, K. J. (2004). Ionic polymer–metal composites: III. Modeling and simulation as biomimetic sensors, actuators, transducers, and artificial muscles. *Smart materials and structures*, 13(6), 1362.
26. Mallavarapu, K., & Leo, D. J. (2001). Feedback control of the bending response of ionic polymer actuators. *Journal of Intelligent Material Systems and Structures*, 12(3), 143-155.
27. Newbury, K. “Characterization, modeling, and control of ionic polymer transducers”, PhD dissertation, Virginia Tech, (2002).
28. Hunt, A., Chen, Z., Tan, X., & Kruusmaa, M. (2009, January). Feedback control of a coupled IPMC (ionic polymer-metal composite) sensor-actuator. In *ASME 2009 Dynamic Systems and Control Conference* (pp. 485-491). American Society of Mechanical Engineers.
29. Liu, D., McDaid, A. J., Aw, K. C., & Xie, S. Q. (2011). Position control of an ionic polymer metal composite actuated rotary joint using iterative feedback tuning. *Mechatronics*, 21(1), 315-328.
30. Tsugawa, M. A., Palmre, V., Carrico, J. D., Kim, K. J., & Leang, K. K. (2015). Slender tube-shaped and square rod-shaped IPMC actuators with integrated sensing for soft mechatronics. *Meccanica*, 50(11), 2781-2795.
31. Philpot, T.A. “Mechanics of materials: an integrated learning system”, Wiley, 3rd ed., (2012).
32. Stalbaum, T., Pugal, D., Nelson, S. E., Palmre, V., & Kim, K. J. (2015). Physics-based modeling of mechano-electric transduction of tube-shaped ionic polymer-metal composite. *Journal of Applied Physics*, 117(11), 114903.
33. Liu, J., Wang, Y., Zhao, D., Zhang, C., Chen, H., & Li, D. (2014, March). Design and fabrication of an IPMC-embedded tube for minimally invasive surgery applications. In *SPIE Smart Structures and Materials+ Nondestructive Evaluation and Health Monitoring* (pp. 90563K-90563K). International Society for Optics and Photonics.

34. Kim, K. J., & Shahinpoor, M. (2002). A novel method of manufacturing three-dimensional ionic polymer–metal composites (IPMCs) biomimetic sensors, actuators and artificial muscles. *Polymer*, *43*(3), 797-802.
35. Palmre, V., Pugal, D., Kim, K. J., Leang, K. K., Asaka, K., & Aabloo, A. (2014). Nanothorn electrodes for ionic polymer-metal composite artificial muscles. *Scientific reports*, *4*.
36. Shen, Q., Kim, K. J., & Wang, T. (2014). Electrode of ionic polymer-metal composite sensors: Modeling and experimental investigation. *Journal of Applied Physics*, *115*(19), 194902.
37. Shen, Q., Palmre, V., Stalbaum, T., & Kim, K. J. (2015). A comprehensive physics-based model encompassing variable surface resistance and underlying physics of ionic polymer-metal composite actuators. *Journal of Applied Physics*, *118*(12), 124904.
38. Fang, B. K., Ju, M. S., & Lin, C. C. K. (2007). A new approach to develop ionic polymer–metal composites (IPMC) actuator: Fabrication and control for active catheter systems. *Sensors and Actuators A: Physical*, *137*(2), 321-329.
39. Kim, S. J., Pugal, D., Wong, J., Kim, K. J., & Yim, W. (2014). A bio-inspired multi degree of freedom actuator based on a novel cylindrical ionic polymer–metal composite material. *Robotics and Autonomous Systems*, *62*(1), 53-60.
40. Tsugawa, M. A., Leang, K. K., Palmre, V., & Kim, K. J. (2013, September). Sectored tube-shaped ionic polymer-metal composite actuator with integrated sensor. In *ASME 2013 Conference on Smart Materials, Adaptive Structures and Intelligent Systems* (pp. V002T06A001-V002T06A001). American Society of Mechanical Engineers.
41. Palmre, V., Kim, S. J., & Kim, K. (2011, March). Millimeter thick ionic polymer membrane-based IPMCs with bimetallic Pd-Pt electrodes. In *SPIE Smart Structures and Materials+ Nondestructive Evaluation and Health Monitoring* (pp. 797615-797615). International Society for Optics and Photonics.
42. Chen, Z., & Tan, X. (2008). A Control-Oriented and Physics-Based Model for Ionic Polymer--Metal Composite Actuators. *IEEE/ASME Transactions on Mechatronics*, *13*(5), 519-529.
43. Ball, P. (1999). Engineering shark skin and other solutions. *Nature*, *400*(6744), 507-509.
44. Ball, P. (2001). Life's lessons in design. *Nature*, *409*(6818), 413-416.

45. Ball, P. (2002). Natural strategies for the molecular engineer. *Nanotechnology*, 13(5), R15.
46. Bar-Cohen, Y. (2006). Biomimetics? using nature to inspire human innovation. *Bioinspiration & biomimetics*, 1(1), P1.
47. Bhushan, B. (2009). Biomimetics: lessons from nature—an overview. *Philosophical Transactions of the Royal Society of London A: Mathematical, Physical and Engineering Sciences*, 367(1893), 1445-1486.
48. Bandyopadhyay, P. R., Beal, D. N., & Menozzi, A. (2008). Biorobotic insights into how animals swim. *Journal of Experimental Biology*, 211(2), 206-214.
49. Deng, X., & Avadhanula, S. (2005, April). Biomimetic micro underwater vehicle with oscillating fin propulsion: system design and force measurement. In *Proceedings of the 2005 IEEE International Conference on Robotics and Automation* (pp. 3312-3317). IEEE.
50. Zhou, Z. G., & Liu, Z. W. (2008). Biomimetic cilia based on MEMS technology. *Journal of Bionic Engineering*, 5(4), 358-365.
51. Yu, J., Tan, M., Wang, S., & Chen, E. (2004). Development of a biomimetic robotic fish and its control algorithm. *IEEE Transactions on Systems, Man, and Cybernetics, Part B (Cybernetics)*, 34(4), 1798-1810.
52. Fish, F. E., Howle, L. E., & Murray, M. M. (2008). Hydrodynamic flow control in marine mammals. *Integrative and Comparative Biology*, 48(6), 788-800.
53. Kamamichi, N., Yamakita, M., Asaka, K., & Luo, Z. W. (2006, May). A snake-like swimming robot using IPMC actuator/sensor. In *Proceedings 2006 IEEE International Conference on Robotics and Automation, 2006. ICRA 2006.* (pp. 1812-1817). IEEE.
54. Kim, B., Kim, D. H., Jung, J., & Park, J. O. (2005). A biomimetic undulatory tadpole robot using ionic polymer–metal composite actuators. *Smart materials and structures*, 14(6), 1579.
55. Kim, K. J., Yim, W., Paquette, J. W., & Kim, D. (2007). Ionic polymer-metal composites for underwater operation. *Journal of Intelligent Material Systems and Structures*, 18(2), 123-131.
56. Kim, K. J., Pugal, D., & Leang, K. K. (2011). A twistable ionic polymer-metal composite artificial muscle for marine applications. *Marine Technology Society Journal*, 45(4), 83-98.

57. Yim, W., Lee, J., & Kim, K. J. (2007). An artificial muscle actuator for biomimetic underwater propulsors. *Bioinspiration & biomimetics*, 2(2), S31.
58. Guo, S., Ge, Y., Li, L., & Liu, S. (2006, June). Underwater swimming micro robot using IPMC actuator. In *2006 International Conference on Mechatronics and Automation* (pp. 249-254). IEEE.
59. Guo, S., Shi, L., Ye, X., & Li, L. (2007, August). A new jellyfish type of underwater microrobot. In *2007 International Conference on Mechatronics and Automation* (pp. 509-514). IEEE.
60. Najem, J., Sarles, S. A., Akle, B., & Leo, D. J. (2012). Biomimetic jellyfish-inspired underwater vehicle actuated by ionic polymer metal composite actuators. *Smart Materials and Structures*, 21(9), 094026.
61. Lauder, G. V., & Madden, P. G. (2007). Fish locomotion: kinematics and hydrodynamics of flexible foil-like fins. *Experiments in Fluids*, 43(5), 641-653.
62. Wen, L., Weaver, J. C., & Lauder, G. V. (2014). Biomimetic shark skin: design, fabrication and hydrodynamic function. *Journal of Experimental Biology*, 217(10), 1656-1666.
63. Shen, Q., Trabia, S., Stalbaum, T., Palmre, V., Kim, K., & Oh, I. K. (2016). A multiple-shape memory polymer-metal composite actuator capable of programmable control, creating complex 3D motion of bending, twisting, and oscillation. *Scientific reports*, 6.
64. Shen, Q., Wang, T., & Kim, K. J. (2015). A biomimetic underwater vehicle actuated by waves with ionic polymer–metal composite soft sensors. *Bioinspiration & biomimetics*, 10(5), 055007.
65. Shen, Q., Wang, T., Liang, J., & Wen, L. (2013). Hydrodynamic performance of a biomimetic robotic swimmer actuated by ionic polymer–metal composite. *Smart Materials and Structures*, 22(7), 075035.
66. Oh, K., Chung, J. H., Devasia, S., & Riley, J. J. (2009). Bio-mimetic silicone cilia for microfluidic manipulation. *Lab on a Chip*, 9(11), 1561-1566.
67. den Toonder, J. M., & Onck, P. R. (2013). Microfluidic manipulation with artificial/bioinspired cilia. *Trends in biotechnology*, 31(2), 85-91.
68. Satir, P., & Christensen, S. T. (2007). Overview of structure and function of mammalian cilia. *Annu. Rev. Physiol.*, 69, 377-400.

69. Satir, P., & Christensen, S. T. (2008). Structure and function of mammalian cilia. *Histochemistry and cell biology*, 129(6), 687-693.
70. Enuka, Y., Hanukoglu, I., Edelheit, O., Vaknine, H., & Hanukoglu, A. (2012). Epithelial sodium channels (ENaC) are uniformly distributed on motile cilia in the oviduct and the respiratory airways. *Histochemistry and cell biology*, 137(3), 339-353.
71. Shahinpoor, M., & Kim, K. J. (2001). Ionic polymer-metal composites: I. Fundamentals. *Smart materials and structures*, 10(4), 819.
72. Shahinpoor, M., & Kim, K. J. (2004). Ionic polymer-metal composites: IV. Industrial and medical applications. *Smart materials and structures*, 14(1), 197.
73. Kim, K. J., & Shahinpoor, M. (2003). Ionic polymer-metal composites: II. Manufacturing techniques. *Smart materials and structures*, 12(1), 65.
74. Kim, K. J., Kim, S. J., & Wong, J. (2015). *U.S. Patent No. 9,147,825*. Washington, DC: U.S. Patent and Trademark Office.
75. Feng, G. H., & Tsai, J. W. (2011, June). 3D omnidirectional controllable elastic IPMC tweezer with self-sensing and adjustable clamping force abilities for biomedical applications. In *2011 16th International Solid-State Sensors, Actuators and Microsystems Conference* (pp. 1725-1728). IEEE.
76. Bar-Cohen, Y. 2004. *Electroactive Polymer (EAP) Actuators as Artificial Muscles: Reality, Potential and Challenges*, Second Edition. Bellingham, WA: SPIE Press. 816 pp
77. Alici, G., Spinks, G. M., Madden, J. D., Wu, Y., & Wallace, G. G. (2008). Response characterization of electroactive polymers as mechanical sensors. *IEEE/ASME Transactions on Mechatronics*, 13(2), 187-196.
78. Punning, A., Kruusmaa, M., & Aabloo, A. (2007). A self-sensing ion conducting polymer metal composite (IPMC) actuator. *Sensors and Actuators A: Physical*, 136(2), 656-664.
79. Kruusamäe, K., Brunetto, P., Graziani, S., Punning, A., Di Pasquale, G., & Aabloo, A. (2010). Self-sensing ionic polymer-metal composite actuating device with patterned surface electrodes. *Polymer International*, 59(3), 300-304.

80. Ko, B. G., Kwon, H. C., & Lee, S. J. (2008). A self-sensing method for IPMC actuator. In *Advances in Science and Technology* (Vol. 56, pp. 111-115). Trans Tech Publications.
81. Shahinpoor, M., & Kim, K. J. (2000). The effect of surface-electrode resistance on the performance of ionic polymer-metal composite (IPMC) artificial muscles. *Smart Materials and Structures*, 9(4), 543.
82. Zhang, W., Guo, S., & Asaka, K. (2006). Development of underwater microrobot with biomimetic locomotion. *Applied Bionics and Biomechanics*, 3(3), 245-252.
83. Edd, J., Payen, S., Rubinsky, B., Stoller, M. L., & Sitti, M. (2003, October). Biomimetic propulsion for a swimming surgical micro-robot. In *Intelligent Robots and Systems, 2003.(IROS 2003). Proceedings. 2003 IEEE/RSJ International Conference on* (Vol. 3, pp. 2583-2588). IEEE.
84. Knehr, K. W., Ertan Agar, C. R. Dennison, A. R. Kalidindi, and E. C. Kumbur. (2012). A transient vanadium flow battery model incorporating vanadium crossover and water transport through the membrane. *Journal of The Electrochemical Society* 159(9), A1446-A1459.
85. Sethuraman, V. A., Khan, S., Jur, J. S., Haug, A. T., & Weidner, J. W. (2009). Measuring oxygen, carbon monoxide and hydrogen sulfide diffusion coefficient and solubility in Nafion membranes. *Electrochimica Acta*, 54(27), 6850-6860.

CURRICULUM VITAE

Tyler P. Stalbaum

(702) 488-2201 • TPSTALBAUM@GMAIL.COM

EDUCATION

Ph.D. in Mechanical Engineering

Dec 2016

University of Nevada, Las Vegas

Dissertation title: "Ionic Electroactive Polymer Devices: Physics-Based Modeling with Experimental Investigation and Verification"

Committee: Kwang J. Kim (Chair), Pushkin Kachroo, Dong-Chan Lee, Woosoon Yim, Hui Zhao

GPA: 4.0/4.0

M.S. in Industrial Engineering

May 2013

Purdue University, West Lafayette, IN

Thesis title: "High Speed Turning of Compacted Graphite Iron Using Controlled Modulation"

Committee: Srinivasan Chandrasekar (Chair), W. Dale Compton, Jose M. Tanchoco

GPA: 3.48/4.0

B.S. in Mechanical Engineering, Magna Cum Laude

Dec 2010

University of Nevada, Las Vegas

GPA: 3.87/4.0

TEACHING

Instructor for Continuum Mechanics (ME 703), UNLV

Fall 2016

Guest lecturer for MEMS and Microsystems (ME 495/695), UNLV

Spring 2016

Guest lecturer for Advanced Thermodynamics (ME 711), UNLV

Fall 2015

Instructor for Mechanical Vibrations (ME 453/653), UNLV

Fall 2014

Teaching assistant for Manufacturing Process Engineering (IE 570), Purdue

Spring 2013

Teaching assistant for Industrial Control Systems (IE 474), Purdue

Fall 2012

Teaching assistant for Engineering Economics (IE 343), Purdue

**Spring 2011 -
Spring 2012**

RESEARCH

Research Assistant

**August 2013 –
present**

Department of Mechanical Engineering, University of Nevada, Las Vegas

- Doctoral research under supervision of Prof. Kwang J. Kim at the Active Materials and Smart Living (AMSL) Laboratory, UNLV
- Designed and analyzed experiments in electroactive materials
- Worked on design and computational simulations of an all-vanadium redox flow battery
- Worked on fabrication and development of new smart materials
- Performed finite element analysis of electroactive materials

ORNL Higher Education Research Experience Internship
Oak Ridge National Laboratory (ORNL), Oak Ridge, Tennessee

**June 2015 –
August 2015**

- Research internship under supervision of Dr. Brett Compton at the Manufacturing Demonstration Facility, ORNL
- Worked on additive manufacturing of electroactive polymer materials
- Developed geometry splicing code for flexible electronics printing
- Gained a strong insight into many other additive manufacturing methods

Research Assistant
Department of Industrial Engineering, Purdue University

**January 2011
– May 2013**

- Masters research under supervision of Profs. Srinivasan Chandrasekar and W. Dale Compton at the Center for Material Processing and Tribology, Purdue
- Worked on high-speed machining of compacted graphite iron using controlled modulation
- Worked closely with M4 Sciences, a West Lafayette start-up company, on calibration and machining tests of Modulation Assisted Machining (MAM) TriboMAM devices
- Studied unconventional deformation processing and corresponding microstructure analysis (modulated machining, large strain extrusion machining)
- Worked on collaborative research with the Paul Hansma Research Group, Department of Physics, UC Santa Barbara, in testing and analysis of the Osteoprobe reference point indentation instrument
- Studied cutting and deformation of hierarchical biologic materials

Purdue University Summer Undergraduate Research Fellowship 2010
Department of Industrial Engineering, Purdue University

**May 2010 –
August 2010**

- Research internship under supervision of Prof. Srinivasan Chandrasekar at the Center for Material Processing and Tribology, Purdue
- Gained an introduction to manufacturing and deformation processing
- Studied simulation of crystal defects and structures of materials using the Bragg-Nye bubble raft model

Undergraduate Research Assistant
Department of Mechanical Engineering, University of Nevada, Las Vegas

**April 2008 –
August 2009**

- Undergraduate research under supervision of Prof. Dan Cook and Dr. Sean Hsieh
- Worked on Basic Automation and Control (BAC) laboratory exercise development in the Entertainment Engineering and Design (EED) program at UNLV
- Worked on the Molten Salt Information System (MOSIS) for developing a knowledge-based resources management system for integrating results of molten salts technology

PUBLICATIONS

(Journal paper #1) Kim, K.J., Palmre, V., Stalbaum, T., Hwang, T., Shen, Q. and Trabia, S. "Promising developments in marine applications with artificial muscles: electrodeless artificial-cilia microfibers." *Marine Technology Society Journal*, accepted for publication (2016).

(Journal paper #2) Shen, Q., Trabia, S., Stalbaum, T., Palmre, V., Kim, K. J., and Oh, I. K. "A multiple-shape memory polymer-metal composite actuator capable of programmable control, creating complex 3D motion of bending, twisting, and oscillation." *Scientific Reports*, 6 (2016): 24462.

(Book chapter #1) Kim, K.J., Palmre, V., Pugal, D., Stalbaum, T., Chen, Z., Tan, X., and Yamakita, M. "IPMCs as EAPs: Models," *Polymers and Polymeric Composites: A Reference Series. Electromechanically Active Polymers*, Carpi, F., editor, Springer, 2015.

(Book chapter #2) Pugal, D., Stalbaum, T., Palmre, V., and Kim, K.J. "Chapter 5. Modeling Ionic Polymer Metal Composites with COMSOL: Step-by-Step Guide," *Ionic Polymer Metal Composites (IPMCs): Smart Multi-Functional Materials and Artificial Muscles Volume 1*, Shahinpoor M., editor, Royal Society of Chemistry, 2015.

(Journal paper #3) Shen, Q., Palmre, V., Stalbaum, T., and Kim, K. J. "A comprehensive physics-based model encompassing variable surface resistance and underlying physics of ionic polymer-metal composite actuators." *Journal of Applied Physics*, 118 (2015): 124904.

(Journal paper #4) Stalbaum, T., Pugal, D., Nelson, S. E., Palmre, V., and Kim, K. J. "Physics-based modeling of mechano-electric transduction of tube-shaped ionic polymer-metal composite." *Journal of Applied Physics*, 117 (2015): 114903.

(Journal paper #5) Randall, C., Bridges, D., Guerri, R., Nogues, X., Puig, L., Torres, E., Mellibovsky, L., Hoffseth, K., Stalbaum, T., Srikanth, A., Weaver, C., Rosen, S., Barnard, H., Brimer, D., Proctor, A., Candy, J., Saldana, C., Chandrasekar, S., Lescun, T., Nielson, C. M., Orwoll, E., Herthel, D., Kopeikin, H., Yang, H. T. Y., Farr, J. N., McCready, L., Khosla, S., Diez-Perez, A., and Hansma, P. K., "Applications of a New Handheld Reference Point Indentation Instrument Measuring Bone Material Strength", *Journal of Medical Devices* 7.4 (2013): 041005.

(Journal paper #6) Guo, Y., Stalbaum, T., Mann, J. B., Yeung, H., and Chandrasekar, S., "Modulation-assisted High Speed Machining of Compacted Graphite Iron (CGI)", *Journal of Manufacturing Processes* 15.4 (2013): 426-431.

CONFERENCE PRESENTATIONS & PROCEEDINGS

Kim, K.J., Stalbaum, T., and Shen, Q. "Ion concentration and electromechanical actuation simulations of ionic polymer-metal composites." *COMSOL Conference 2016 Boston*. Presentation and poster.

Trabia, S., Shen, Q., Stalbaum, T., Hunt, R., Hwang, T., and Kim, K.J. "Numerical and experimental investigation of a biomimetic robotic jellyfish actuated by ionic polymer-metal composite." *13th International Conference on Ubiquitous Robots and Ambient Intelligence URAI, IEEE*, (2015). Poster only.

Hwang, T., Palmre, V., Stalbaum, T., Shen, Q., Trabia, S., and Kim, K.J. "IPMC cilia system for artificial muscle applications." *Proc. SPIE 979818*, (2016). Presentation only.

Stalbaum, T., Trabia, S., Shen, Q., and Kim, K.J. "Fluid flow sensing and control using ionic polymer-metal composites." *Proc. SPIE 9782E*, (2016). Presentation and paper.

Shen, Q., Palmre, V., Stalbaum, T., and Kim, K.J. "Comprehensive modeling of ionic polymer-metal composite actuators based upon variable surface resistance and underlying physics of the polymer membrane." *Proc. SPIE 94302J*. Poster and paper.

Stalbaum, T., Nelson, S.E., Palmre, V., and Kim, K.J. "Theoretical investigation of ionic effects in actuation and sensing of IPMCs of various geometries." *Proc. SPIE 9432-32*, (2015). Presentation and paper.

Stalbaum, T., Nelson, S. E., Palmre, V., and Kim, K. J. "Multi degree of freedom IPMC sensor." *Proc. SPIE 9056-92*, (2014). Presentation and paper.

HONORS & AWARDS

NASA EPSCOR Space Grant Fellowship, Spring 2015, UNLV

Purdue University Summer Undergraduate Research Fellowship 2010 (PURDUE SURF 2010)

Mechanical Engineering Outstanding Graduating Senior, Class of 2010, UNLV

Ray Kozak Scholarship, Fall 2010, UNLV

Nevada Millennium Scholarship, Fall 2006 - Fall 2010, UNLV

National Science and Mathematics Access to Retain Talent (SMART) Grant, Fall 2008 - Spring 2010, UNLV

CSUN Scholarship, Fall 2008, UNLV

Josef Princ Memorial Scholarship, Fall 2006 - Spring 2008, UNLV

Williams Memorial Scholarship, Fall 2006 - Spring 2007, UNLV

CERTIFICATIONS

FE certified Engineer in Training (EIT) in the US as of June 4, 2010